DISSERTATIONES
CHIMICAE
UNIVERSITATIS
TARTUENSIS
229

HUY QUÍ VINH NGUYEN

Development of Carbon Supported Pt–CeO_2 Catalysts for Proton Exchange Membrane Fuel Cells

DISSERTATIONES CHIMICAE UNIVERSITATIS TARTUENSIS
229

DISSERTATIONES CHIMICAE UNIVERSITATIS TARTUENSIS
229

HUY QUÍ VINH NGUYEN

Development of Carbon Supported Pt–CeO_2 Catalysts for Proton Exchange Membrane Fuel Cells

UNIVERSITY OF TARTU
Press
1632

Institute of Chemistry, Faculty of Science and Technology, University of Tartu, Estonia.

The dissertation is accepted for the commencement of the degree of Doctor of Philosophy in Chemistry on June 11th, 2024 by the Council of the Institute of Chemistry, University of Tartu.

Supervisors:	Prof. Jaak Nerut, Ph.D. University of Tartu, Estonia
	Prof. Enn Lust, Ph.D. University of Tartu, Estonia
	Heili Kasuk, Ph.D. University of Tartu, Estonia
Opponents:	Asst. Prof. Jonathan Quinson, Ph.D. Aarhus University, Denmark
Commencement:	August 16th, 2024, at 11:15. Auditorium 1020, Ravila 14a, Tartu.

This work has been partially supported by ASTRA project PER ASPERA Graduate School of Functional Materials and Technologies receiving funding from the European Regional Development Fund under project in University of Tartu, Estonia

ISSN 1406-0299 (print)
ISBN 978-9916-27-588-7 (print)
ISSN 2806-2159 (pdf)
ISBN 978-9916-27-589-4 (pdf)

University of Tartu Press
http://www.tyk.ee/

TABLE OF CONTENTS

1. LIST OF ORIGINAL PUBLICATIONS **7**

2. ABBREVIATIONS AND SYMBOLS **8**

3. INTRODUCTION **13**

4. LITERATURE OVERVIEW **15**
4.1. Proton Exchange Membrane Fuel Cells 15
4.1.1. Chromium Carbide-Derive Carbon Supports 17
4.1.2. Effects of CeO_2 Coupled with Pt on Catalytic Activity . . . 18
4.1.3. Oxygen Reduction Reaction 19
4.1.4. Methanol Oxidation Reaction 23
4.2. Optimisation of Synthesis Methods 27
4.2.1. Ethylene Glycol Reduction Method 27
4.2.2. Nucleation and Growth of Metal Particles 29
4.2.3. Sedimentation of Metal Particles onto The Supports 30
4.2.4. Effect of Energy Providing Methods on Catalyst Parameters 33
4.2.5. Synthesis Methods of CeO_2 Modified Catalysts 36
4.3. Characterisation Methods 37
4.3.1. Low-Temperature Nitrogen Sorption (LTNS) 37
4.3.2. Characterisation of Structure and Morphology 38
4.3.3. Cyclic Voltammetry (CV) 39
4.3.4. Rotating Disk Electrode Method 43
4.3.5. Kinetics Assessment 44
4.3.6. Stability Assessment 45

5. EXPERIMENTAL **46**
5.1. Synthesis of Materials 46
5.1.1. Synthesis of Chromium Carbide-Derived Carbons 46
5.1.2. Synthesis of CeO_2 46
5.1.3. Pt-CeO_2/C Catalysts Preparation 47
5.2. Physical and Electrochemical Characterisation of Catalysts 52
5.2.1. Physical Characterisation Methods 52
5.2.2. Electrochemical Measurements 53

6. RESULTS AND DISCUSSIONS **56**
6.1. Structure of Catalysts 56
6.1.1. Chemical Composition, Structure, and Morphology of C(Cr_3C_2) Materials 56
6.1.2. Chemical Composition, Structure, and Morphology of CeO_2/C Materials 59

6.1.3. Chemical Composition, Structure, and Morphology of PtC and Pt−CeO_2/C Materials 63
6.2. Oxygen Reduction Reaction 71
6.2.1. The Oxygen Reduction Reaction on Chromium Carbide-Derived Carbon Materials 71
6.2.2. Influence of Heating Method and Formation of Glycolate-Based System on Pt-based Catalysts ORR Characteristics . 76
6.2.3. Influences of CeO_2 on ORR Characteristics of Pt-based Catatlysts 77
6.2.4. Influence of Chromium Carbide-Derived Carbon Support on ORR Characteristics of Pt-based Catatlysts 79
6.3. Methanol Oxidation Reaction 79
6.3.1. Manipulation of EG Reduction Methods by Glycolate Anions 79
6.3.2. Influence of Ageing Catalyst Suspension on MOR Activity 80
6.3.3. Influence of Hydrogen Post-Treatment on MOR Activity of Catalysts 82
6.3.4. Influences of Heating Method During The Synthesis on MOR Activity of Catalysts 83
6.3.5. Influence of the Sedimentation Method on MOR Activity of Catalysts 85
6.3.6. Influence of CeO_2 on MOR Activity of Catalysts 87
6.3.7. Influence of Sodium Hydroxide Concentration in Synthesis Mixture on MOR Activity of Catalysts 90
6.3.8. Influence of Chromium Carbide-Derived Carbon Support on MOR Activity of Catalysts 92
6.4. The Best Catalyst Materials 94

7. SUMMARY **96**

8. REFERENCES **98**

9. SISUKOKKUVÕTE (SUMMARY IN ESTONIAN) **108**

10. ACKNOWLEDGEMENTS **110**

11. PUBLICATIONS **113**
Paper I 115
Paper II 135
Paper III 151
Paper IV 167

CURRICULUM VITAE **183**

ELULOOKIRJELDUS (CURRICULUM VITAE IN ESTONIAN) **185**

1. LIST OF ORIGINAL PUBLICATIONS

I. **H. Q. V. Nguyen**, J. Nerut, H. Kasuk, V. Grozovski, T. Thomberg, I. Tallo, R. Palm, M. Koppel, T. Romann, J. Aruväli, M. Külaviir, and E. Lust, Oxygen Reduction Reaction on Chromium Carbide-Derived Carbons, *Russ. J. Electrochem.* 58 (2022) 781-797.

II. **H. Q. V. Nguyen**, J. Nerut, H. Kasuk, M. Härmas, P. Valk, T. Romann, M. Koppel, P. Teppor, J. Aruväli, O. Korjus, O. Volobujeva, and E. Lust, Optimisation of The Ethylene Glycol Reduction Method for The Synthesis of Platinum-Ceria-Carbon Materials as Catalysts for The Methanol Oxidation Reaction, *J. Solid State Electrochem.* 27 (2023) 313-326.

III. **H. Q. V. Nguyen**, J. Nerut, H. Kasuk, T. Thomas, T. Romann, J. Aruväli, and E. Lust, Ultra-Small Ceria Nanocrystals at Carbon Surface synthesised by Ultrasound Sonication: A Study of Highly Active Platinum-Cerium Bifunctional Catalysts for Methanol Oxidation and Oxygen Reduction, *ECS Trans.* 111 (2023) 17.

IV. **H. Q. V. Nguyen**, J. Nerut, H. Kasuk, T. Thomas, T. Romann, J. Aruväli, M. Külaviir, P. Paaver, Z. Kochovski, E. Härk and E. Lust, Influence of Chromium Carbide-Derived Carbon Support and Ceria Nanocrystals on Pt-CeO_2/C Catalysts for Fuel Cell Applications, *ECS Adv.*, 3 (2024) 024505.

Author's contribution:

Paper I: Performed the electrochemical measurements and some physical characterisations such as low-temperature nitrogen sorption (LTNS) and thermogravimetric analysis (TGA), analysed the data and wrote the manuscript

Paper II: Developed the idea of paper, synthesised the catalysts, performed the electrochemical measurements and some physical characterisations (LTNS and TGA), analysed the data and wrote the manuscript

Paper III: Developed the idea of paper, synthesised the catalysts, performed the electrochemical measurements and some physical characterisations (LTNS and TGA), analysed the data and wrote the manuscript

Paper IV: Developed the idea of paper, synthesised the catalysts, performed the electrochemical measurements and some physical characterisations (LTNS and TGA), analysed the data and wrote the manuscript

2. ABBREVIATIONS AND SYMBOLS

Abbreviations

Notation	Description
AST	accelerated stability test
BET	Brunauer-Emmett-Teller
C(KB)	Ketjenblack carbon powder
CA	chronoamperometry
CB	carbon black powder
$C(Cr_3C_2)$	chromium carbide-derived carbon powder (electrode)
CDC	carbide-derived carbon powder
Ce_{MW}	CeO_2 in colloidal solution synthesised with the heating step conducted using microwave radiation (the synthesis parameters are in subsection 5.1.2)
CeO_2/C_{solvo}	CeO_2 activated carbon material synthesised by solvothermal synthesis method (the synthesis parameters for this ceria activated carbon are in subsection 5.1.2)
CeO_2/C_{ultr}	CeO_2 activated carbon material synthesised by the ultrasound sonication method (the synthesis parameters for this ceria activated carbon are in subsection 5.1.2)
Ce_{ultr}	the CeO_2 in colloidal solution synthesised with the heating step conducted using ultrasound sonication (the synthesis parameters are in subsection 5.1.2)
CNT	classical nucleation theory
CV	cyclic voltammetry
DFT	density functional theory
DMFC	direct methanol fuel cell
ECSA	electrochemcial active surface area
EDL	electrical double layer
EDX	energy dispersive X-Ray spectroscopy
EG	ethylene glycol
EIS	electrochemical impedance spectroscopy
EV	electric vehicle
FWHM	full width at half maximum
GCDE	glassy carbon disk electrode
GDL	gas diffusion layer
hcd	high current density
HOR	hydrogen oxidation reaction
lcd	low current density

Notation	Description
LTNS	low-temperature nitrogen sorption
MA	mass activity
MEA	membrane electrode assembly
MOR	methanol oxidation reaction
MW	microwave
NLDFT	non-local density functional theory
NP	nanoparticle
ORR	oxygen reduction reaction
PEMFC	proton exchange membrane fuel cell
PSD	particle size distribution
PSF	peak shape functions
$PtC(Cr_3C_2)$	the PtC catalysts deposited onto the chromium carbide-derived carbon support (the synthesis parameters for this material are in subsection 5.1.3)
$PtCe_{chl}$	the $Pt-CeO_2/C$ complex catalyst prepared at the synthesis parameters given in subsection 5.1.3 and the HCl solution was used for the deposition of metals onto the support material
$PtCe_{H_2O_2}$	the $Pt-CeO_2/C$ complex catalyst prepared at the synthesis parameters given in subsection 5.1.3 and the hydroperoxide solution was used for the deposition of metals onto the support material
$PtCe_{H_3PO_4}$	the $Pt-CeO_2/C$ complex catalyst prepared at the synthesis parameters given in subsection 5.1.3 and the H_3PO_4 solution was used for the deposition of metals onto the support material
$PtCe_{Na}$	the $Pt-CeO_2/C$ complex catalyst on the Ketjenblack carbon support synthesised by using the reaction of Na and ethylene glycol to generate glycolate ions for the synthesis solution (the synthesis parameters for this material are in subsection 5.1.3)
$PtCe_{NaOH}$	the $Pt-CeO_2/C$ catalyst deposited onto the Ketjenblack carbon support synthesized by ethylene glycol reduction method in the NaOH solution reaction system and the combination of heating methods (microwave, ultrasound radiation, and refluxing) is used
$PtCe_{sul}$	the $Pt-CeO_2/C$ complex catalyst prepared at the synthesis parameters given in subsection 5.1.3 and the H_2SO_4 solution was used for the deposition of metals onto the support material

Notation	Description
PtC(KB)	the PtC catalysts deposited onto the Ketjenblack carbon support, by using the reflux method for the heating step (the synthesis parameters for this material are in subsection 5.1.3)
$PtC(KB)_{com}$	the PtC catalysts deposited onto the Ketjenblack carbon support, by using the combination of different heating methods. The synthesis parameters for this material are in subsection 5.1.3
PWD	pore-width distribution
RDE	rotating disk electrode
RDS	rate determining step
RHE	reversible hydrogen electrode
SA	specific activity
SEM	scanning electron microscopy
TEM	transmission electron microscopy
TGA	thermogravimetric analysis
WE	working electrode
XRD	X-ray diffraction

Latin Symbols

Notation	Description
c_{Na^+}	the concentration of Na^+ in the reaction mixture
C	capacitance
C_p	the capacitance value of a parallel circuit
c_{Pt}	Pt concentration on the electrode surface
$c_{Pt(IV)}$	the $[PtCl_6]^{2-}$ concentration in solution
C_s	the capacitance value of a series circuit
$d_{CeO_2,\ microscopy}$	CeO_2 crystallite size observed from either scanning electron microscopy or transmission electron microscopy images
$d_{CeO_2,\ XRD}$	CeO_2 crystallite size estimated from X-ray diffraction data
D_p	penetration depth
$d_{Pt,\ ECSA}$	diameter of Pt nanoparticles estimated from the electrochemical active area value
$d_{Pt,\ microscopy}$	Pt crystallite size estimated from either scanning electron microscopy or transmission electron microscopy images
$d_{Pt,\ XRD}$	Pt crystallite size estimated from X-ray diffraction data

Notation	Description
D_{Scherrer}	effective crystallite size
E_{onset}	the onset potential value
E_{p}	peak potential
E_{peak}	the potential value of the first oxygen reduction reaction peak in cyclic voltammetry measurement
f	frequency
H_{UDP}	hydrogen species under deposition potential
I	current
$i_{\text{CA at 0.50 V}}$	the stable mass activity at the end of the chronoamperometry duration measured at 0.50 V
$i_{\text{CA at 0.85 V}}$	the stable mass activity at the end of the chronoamperometry duration measured at 0.85 V
$i_{\text{ap, CV}}$	the mass activity calculated using the anode peak current measured in cyclic voltammetry
i_{CA}	the stable mass activity was measured at the potential value of the anodic peak of the methanol oxidation reaction measurement in cyclic voltammetry
$i_{\text{CA at 0.85 V}}/i_{\text{ap, CV}}$	the ratio of $i_{\text{CA at 0.85 V}}$ and $i_{\text{ap, CV}}$
I_{p}	peak current
j	current density
j_{k}	oxygen reduction reaction kinetic current density
P/P_0	relative pressure
$Q_{\text{H}_{\text{UDP}}}$	the sum of H_{UDP} charges
S_{BET}	specific surface area
S_{DFT}	total surface area
S_{external}	surface area of meso- and macro-porous area
$S_{\text{micropores}}$	microporous pore area
$t_{\text{ultrasound}}$	duration of ultrasound treatment during the synthesis of $\text{Pt}-\text{CeO}_2/\text{C}$ materials
V_{ads}	total adsorbed nitrogen volume
V_{m}	adsorbed volume of nitrogen of the complete unimolecular adsorbed layer
$V_{\text{mesopores}}/V_{\text{total}}$	ratio of mesoporous volume to total pore volume
$V_{\text{micropores}}$	microporous pore volume
V_{total}	total pore volume

Greek Symbols

Notation	Description
ΔE_{pp}	peak potential seperation

Notation	Description
δ	diffusion layer thickness
ε'	relative permittivity
ε''	dielectric loss
ν	the potential scan rate
$\tan\delta$	dielectric loss tangent

3. INTRODUCTION

Electric cars have already gained considerable interest from governments and industries, and this interest continues to rise. Although electric cars using batteries as an energy source currently dominate the market, it is hard to establish the electric vehicle (EV) infrastructure in the city. The challenge arises from the need for numerous fast-charging points (i.e. fully charge of a 200-mile range EV under 30 min) for mass EV adoption [1]. Refueling stations for EVs using such alternative fuels as hydrogen or alcohol seems to be a more accessible and more practical solution than megawatt charging stations [2, 3]. This has motivated the researchers to study the proton exchange membrane fuel cell (PEMFC), as this device is more suitable for electricity production for long-range and heavy-duty EVs.

PEMFCs devices generate electricity using various fuels, including hydrogen, alcohol, hydrazine, and ammonia. The anode and cathode of PEMFCs are separated by a proton exchange membrane (PEM). Depending on the fuel used, PEMFCs can have specific names, such as direct methanol fuel cell (DMFC) [4], direct ethanol fuel cell [4], direct dimethyl ether fuel cell [5], and direct hydrazine fuel cell [6, 7]. PEMFCs are usually preferred to hydrogen-fueled PEMFCs [8]. These fuel cells work due to the oxidation reaction of the fuel at the anode catalyst and oxygen reduction reaction (ORR) at the cathode catalyst [4, 8–10]. Electrons released from the oxidation reaction at the anode and travel through the load to the cathode to participate in the ORR. Both anode and cathode reactions need to be catalysed to increase the efficiency of the PEMFC. The ORR is rather sluggish, prompting extensive research to develop better ORR catalysts as ORR is important regardless of the PEMFC type. The hydrogen oxidation at the low-loading Pt catalysts is usually very fast. The oxidation of alcohols is much slower due to complex reaction mechanism [4]. In the later case, the anode catalyst suffers from Pt deactivation due to the adsorption of intermediates from alcohol oxidation reaction, and due to corrosion. The poisoning issue becomes more serious over time. In the DMFC, methanol oxidation reaction (MOR) is also sluggish and the better catalysts are needed. In this thesis, the focus is on development of MOR catalysts, which also catalyse ORR.

The most common catalysts for PEMFCs are Pt-based catalysts deposited onto various catalyst supports [4, 8–10]. The structure of Pt is sensitive to the adsorption of oxygen-containing species at the surface [11–13]. This sensitivity facilitates the ORR [11]. However, Pt is very easily deactivated by the adsorption of certain chemical species, known as catalyst poisons (e.g. H_2S, bisulfate, halides, and CO adsorptions) [14–16], which can occur at both anode and cathode. In the case of DMFC, the performance and durability of the anodic catalyst severely affected by the adsorption of CO-like intermediates of MOR. In case of the DMFC cathode catalyst, the durability of the catalyst can be reduced

by the impurities from the feed gas and crossover of methanol from the anode side to cathode side [4, 17]. An excellent DMFC anode catalyst can also work well at the cathode, such as PtRu and Pt−CeO_2 catalysts, because the poisoning condition at the DMFC anode is more extreme than at the cathode, and most of the catalytic activity of MOR and ORR comes from Pt [4, 18–21]. To overcome the poisoning issue, another metal or metal oxide can be coupled with Pt to weaken the bond between Pt and catalyst poisons and facilitate the oxidation reaction of poisons at the Pt surface [21–25]. In the selection of metals and/or metal oxides coupled with Pt, rare-earth metals, especially CeO_2-based catalysts, are attractive to the researchers due to their high abundance in Earth's crust and synergistic effects to promote both ORR and MOR [19, 20, 26]. Additionally, the electrochemical activity of Pt is dependent on the dispersion of Pt nanoparticles (NPs) and their characteristics of Pt NPs on the support surface. Common catalyst supports are carbon and/or carbides and/or metal oxides [27, 28]. However, carbon black is dominantly used as they have high surface area ($\geq$250 $m^2\,g^{-1}_{material}$), low cost and high availability [27, 28]. The unique structure and morphology of different carbons can influence both the durability and performance of PEMFCs [29, 30]. Thus, the selection of a metal element and carbon is essential for an excellent Pt-based catalyst.

The main aim of this study was to address the catalysis issues in DMFCs mentioned above. To achieve this, the following aims were set.

- Develop and analyse the unique structure of chromium carbide-derived carbon supports, synthesised under different conditions, as possible catalyst supports.
- Optimise the synthesis methods for the preparation of Pt−CeO_2/C complex catalysts, targeting the MOR at the DMFC anode catalyst.
- Improve the MOR and ORR activity of Pt−CeO_2/C complex catalysts by improving the dispersion of Pt and CeO_2 NPs and analysing the (structural) factors influencing the catalytic activity and durability.

4. LITERATURE OVERVIEW

4.1 Proton Exchange Membrane Fuel Cells

The general structure of a single-cell PEMFC is demonstrated in Figure 1. The heart of a PEMFC is the membrane electrode assembly (MEA), which includes catalyst layers and PEM. The core components of a PEMFC consist of porous carbon layers as a gas diffusion layer (GDL) on two sides of the MEA. The gaskets and GDL control the flow of gases (including fuel) to the MEA and the removal of products such as water from the MEA to the outside. Bipolar plates are the current collectors and are used to connect the electrodes with the application loads. In this study, the main component of the catalyst is $Pt{-}CeO_2$ on a carbon support, and with the PEM being a Nafion membrane.

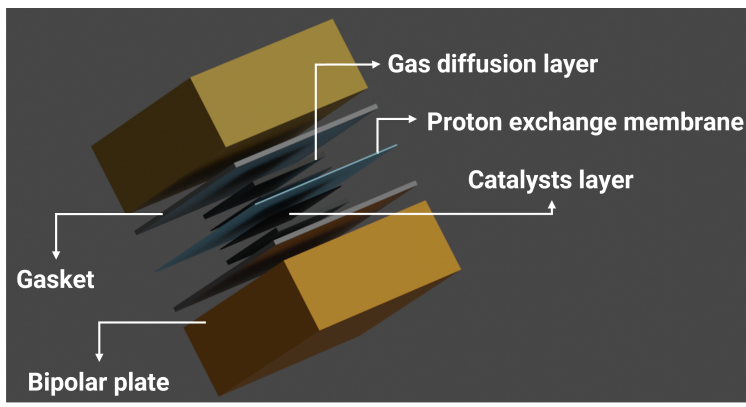

Figure 1. Structure of a proton exchange membrane fuel cell with components, noted in the figure.

Although the general structure of hydrogen fueled PEMFC and DMFCs is similar as demonstrated in Figure 1, the working principles are slightly different (Figures 2 and 3). For PEMFCs, the hydrogen oxidation reaction (HOR) takes place at the anode (Equation 4.1), where electrons and protons are generated.

$$H_2 \longrightarrow 2\,H^+ + 2\,e^- \quad \text{(at anode)}. \tag{4.1}$$

The protons are transported through the PEM to the cathode, while the electrons are transferred through the application device to the cathode. Electrons and protons participate in the ORR at the cathode (Equation 4.2), and water is produced.

$$O_2 + 4\,H^+ + 4\,e^- \longrightarrow 2\,H_2O \quad \text{(at cathode)}. \tag{4.2}$$

The main difference between the hydrogen-fueled PEMFC and DMFC is the MOR at the anode. In the MOR, CO_2 and protons are produced (Equation 4.3).

$$CH_3OH + H_2O \longrightarrow CO_2 + 6\,H^+ + 6\,e^- \quad \text{(at anode)}. \tag{4.3}$$

The ORR also takes place at the cathode of the DMFC (Equation 4.2), a small amount of methanol can crossover the PEM to form CO_2 at the cathode side. Thus, the ORR, HOR, and MOR have to be studied to develop good catalysts for hydrogen-fueled PEMFC and DMFC. However, the working conditions of MOR are more extreme than that of HOR. Therefore, the MOR catalysts are investigated in this study.

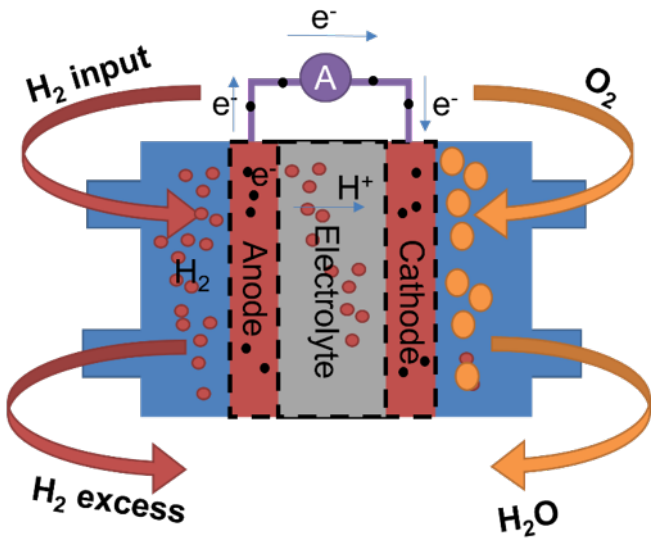

Figure 2. Working principle of proton exchange membrane fuel cell powered by hydrogen fuel. The black dash lines indicate the boundaries of components in the membrane electrode assembly compartment.

4.1.1 Chromium Carbide-Derive Carbon Supports

Carbon as catalyst support is a dominant element in catalyst layers for PEMFC electrodes. Many different types of carbon have been studied for PEMFC applications, such as ordered mesoporous carbon powder, carbon black powder (CB), single-walled carbon nanotubes, multi-walled carbon nanotubes, and carbide-derived carbon powder (CDC). Each type of carbon has a unique structure and morphology, and it influences the metal dispersion on the carbon support and the formation of metal NPs. Therefore, the carbon support contributes to the electrochemical activity and durability of catalyst material [31–33].

Amongst carbon supports mentioned above, CDC support materials for PEMFC are widely studied at the University of Tartu [34–38]. The formation of a unique micro-mesoporous structure occurs during the chlorination step following the diffusion of metal elements (in the form of chloride) from binary carbides out of the carbon structure. Additionally, the large specific surface area of this type of carbon facilitates better metal dispersion on the support surface. One of the interesting CDC materials synthesised by Thomberg *et al.* [39] is chromium CDC. Different metal carbide precursors and synthesis temperature influence the porosity, morphology, and graphitisation level of the carbon [39, 40]. Thomberg *et al.* [39] have identified that chromium(II) carbide, especially Cr_3C_2, is a good metal carbide precursor for preparing a micro-mesoporous carbon. This chromium CDC is synthesised following the reaction (Equation 4.4):

$$2\,Cr_3C_2 + 9\,Cl_2 \longrightarrow 6\,CrCl_3 + 4\,C \tag{4.4}$$

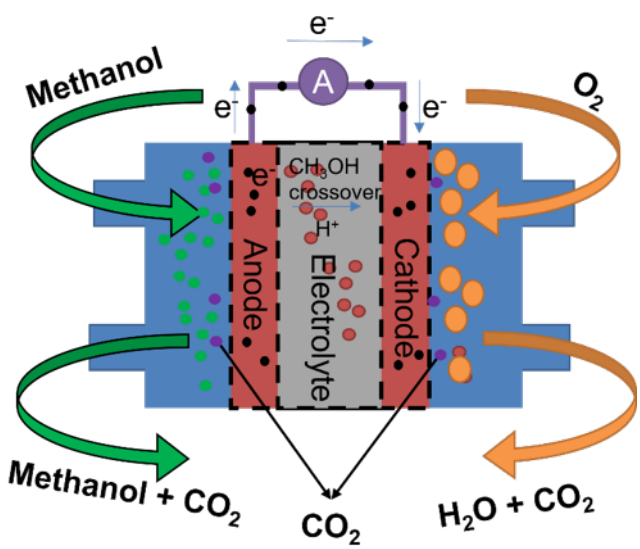

Figure 3. Working principle of direct methanol fuel cells. The black dash lines indicate the boundaries of components in the membrane electrode.

Additionally, the study by Hoffman *et al.* [41] reveals that the chlorination of this type of binary carbide produces carbon with uniform position of carbon atoms in the lattices, high specific surface area, large pore volume, and a good ratio between micropores and mesopores.

4.1.2 Effects of CeO_2 Coupled with Pt on Catalytic Activity

Cerium has gained interest among researchers due to its abundant presence in the Earth's crust [26]. The presence of CeO_2 during the Pt deposition onto carbon support generates more Pt^0 species and improves the dispersion of Pt on the support surface [42]. This effect is caused by the redox reaction of Ce^{3+} with Pt cations (Equations 4.5 and 4.6) [43]:

$$Pt^{4+} + 4\,Ce^{3+} \longrightarrow Pt + 4\,Ce^{4+}, \tag{4.5}$$

and/or

$$Pt^{2+} + 2\,Ce^{3+} \longrightarrow Pt + 2\,Ce^{4+}. \tag{4.6}$$

Additionally, the main component of the catalyst (CeO_2 coupled with Pt) enhances the electrochemical activity and stability of the catalysts towards both MOR and ORR.

In the case of MOR, the enhancement occurs due to the fluorite structure of CeO_2. The structure of CeO_2 can act as an oxygen reservoir (Equations 4.7 – 4.10) and switch between the cation oxidation states of Ce^{4+} and Ce^{3+} [44, 45].

$$\frac{1}{2}\,O_2 + V_{O}^{\bullet\bullet 2-} \longrightarrow O_O^{x} + 2\,h^{\bullet}, \tag{4.7}$$

$$Ce^{4+}{-}O{-}Pt^{2+} + CO + O_O^{x} \longrightarrow Ce^{4+}{-}O{-}Pt^{0} + V_{O}^{\bullet\bullet 2-} + CO_2, \tag{4.8}$$

$$Ce^{4+}{-}O{-}Pt^{0} + h^{\bullet} \longrightarrow Ce^{3+}{-}O{-}Pt^{2+}, \tag{4.9}$$

$$Ce^{3+}{-}O{-}Pt^{2+} + h^{\bullet} \longrightarrow Ce^{4+}{-}O{-}Pt^{2+}, \tag{4.10}$$

where $V_{O}^{\bullet\bullet 2-}$, O_O^{x}, and $h^{\bullet}$ are the doubly ionised oxide ion vacancy, neutral oxygen occupying the vacancy, and the electron-hole, respectively. This explains why the CO-like compounds on the surface of catalysts containing CeO_2 are easily oxidised. Moreover, the electron configuration of CeO_2 in the ground state with 4f electrons can weaken the interaction between Pt and CO_{ads} by transferring electrons from CeO_2 to the 3d orbital of Pt [21]. Therefore, the CO_{ads} on the Pt surface can be easily oxidised off.

In case of ORR, the activity of Pt-CeO_2 catalysts is improved because the fluorite structure of CeO_2 facilitates the formation of water from H_2O_2. The process can be described by the equations below [46]:

$$O_2 + 2\,H^{+} + 2\,e^{-} \longrightarrow H_2O_2, \tag{4.11}$$

$$2\,CeO_2 + 2\,H^+ + 2\,e^- \longrightarrow Ce_2O_3 + H_2O, \tag{4.12}$$

$$Ce_2O_3 + H_2O_2 \longrightarrow 2\,CeO_2 + H_2O. \tag{4.13}$$

The presence of Ce^{3+} as the intermediate (Ce_2O_3) lowers the risk of carbon oxidation by hydrogen peroxide. Therefore, the lifetime of the cathode material can be improved.

Although the main electrochemical activity of the catalyst material comes from Pt, it is obvious that the presence of CeO_2 influences the electrochemical activity of MOR and ORR reactions. Additionally, the CeO_2 crystals with different morphologies have varying impacts on electrochemical activity [20, 47, 48]. Flower-shaped, rod-shaped and sphere-shaped crystals of CeO_2 exhibit higher electrochemical activity than other shapes due to the strong interaction between Pt and CeO_2, as well as the abundance of oxygen vacancies on (100)/(110) planes.

4.1.3 Oxygen Reduction Reaction

The ORR takes place at the PEMFC cathode. To predict the ORR activity of the Pt−CeO_2/C catalyst, the electrochemical measurements are conducted in acid solution. The overall chemical reaction pathway of ORR (Figure 4) in acid solution can follow a 4-electron process [49]:

$$O_2 + 4\,H^+ + 4\,e^- \longrightarrow 2\,H_2O \quad E^\circ = 1.229\,V. \tag{4.14}$$

Alternatively, the ORR can follow the hydrogen peroxide pathway, also known as the 2+2 electron process. In the 2-electron process, the hydrogen peroxide is formed:

$$O_2 + 2\,H^+ + 2\,e^- \longrightarrow H_2O_2 \quad E^\circ = 0.67\,V. \tag{4.15}$$

Subsequently, the hydrogen peroxide can be reduced in another 2-electron process:

$$H_2O_2 + 2\,H^+ + 2\,e^- \longrightarrow 2\,H_2O \quad E^\circ = 1.77\,V, \tag{4.16}$$

or it can decompose:

$$2\,H_2O_2 \longrightarrow 2\,H_2O + O_2. \tag{4.17}$$

The detailed mechanism of ORR differs for various surfaces. On Pt catalysts, it is generally accepted that the ORR begins with the adsorption of an oxygen molecule at the surface of the Pt catalyst (Equation 4.18).

$$O_2 \rightleftharpoons O_{2(ads)} \tag{4.18}$$

The subscript part "(ads)" indicates the adsorbed species at the active site.

However, there are two different mechanisms for the 4-electron process of ORR [50]. The first mechanism is the dissociative route (Equations 4.19 – 4.21), which has the rate constant k_1 in Figure 4 [51]. The O−O bond is broken to form

the adsorbed atomic oxygen when O_2 is adsorbed onto Pt clusters (Equation 4.19). After that, two electrons are transferred from the Pt surface, and water is produced (Equations 4.20 and 4.21). In total, four electrons are consumed to reduce one O_2 molecule to water.

$$O_{2(ads)} + 2\,Pt \longrightarrow 2\,Pt{-}O, \tag{4.19}$$

$$Pt{-}O + H^+ + e^- \longrightarrow Pt{-}OH \quad \text{is the rate determining step (RDS)}, \tag{4.20}$$

$$Pt{-}OH + H^+ + e^- \longrightarrow Pt + H_2O. \tag{4.21}$$

The second mechanism is the associative route (Equations 4.22 – 4.25). In

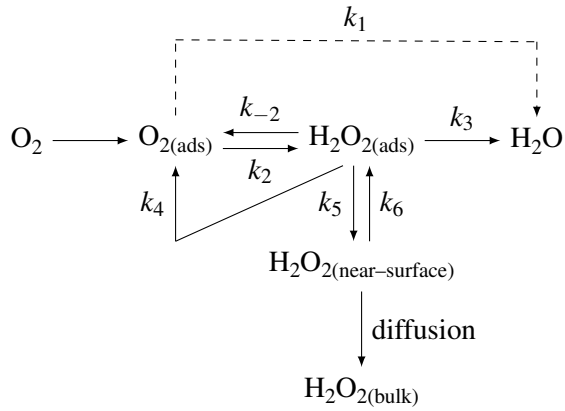

Figure 4. Scheme for oxygen reduction reaction mechanism at the electrode surface in acid media [51].

this route, the O−O bond is broken in the second step (Equation 4.23). In the case of both mechanisms, the peroxide cannot be formed if the O−O bond is broken either in the first (Equation 4.19) or in the second step (Equation 4.23).

$$Pt{-}O_{2(ads)} + H^+ + e^- \longrightarrow Pt{-}OOH \quad \text{is the RDS}, \tag{4.22}$$

$$Pt{-}OOH + H^+ + e^- \longrightarrow Pt{-}OH + HO, \tag{4.23}$$

$$Pt{-}OH + OH + H^+ + e^- \longrightarrow Pt{-}OH + H_2O, \tag{4.24}$$

$$Pt{-}OH + H^+ + e^- \longrightarrow Pt + H_2O. \tag{4.25}$$

However, if the O−O bond of Pt−OOH is not broken after the first step (Equation 4.22), the ORR follows the hydrogen peroxide pathway and could be described by following equations below:

$$Pt{-}OOH + H^+ + e^- \longrightarrow Pt{-}(OHOH)_{ads}. \tag{4.26}$$

The hydrogen peroxide is formed in a 2-electron process (Equations 4.22 and 4.26) described by the rate constant k_2 and the reverse process is the oxidation of peroxide to form $O_{2(ads)}$ with the rate constant k_{-2}. After that, the adsorbed

peroxide at the Pt surface is reduced to water (Equations 4.27 and 4.28) described by the rate constant k_3.

$$\mathrm{Pt{-}(OHOH)_{ads} + H^+ + e^- \longrightarrow Pt{-}OH + H_2O}, \tag{4.27}$$

$$\mathrm{Pt{-}OH + H^+ + e^- \longrightarrow Pt{-}OH_2}. \tag{4.28}$$

The $H_2O_{2(ads)}$ can either decompose back at the electrode surface to form $O_{2(ads)}$ described by the rate constant k_4, or desorbed (and evolved) from the surface described by the rate constant k_5. Near the electrode surface, the hydrogen peroxide can adsorb back to the electrode surface with the rate constant k_6. The dissociative and associative mechanisms could occur in parallel at the electrode surface. However, at the electrode potential around 0.8 V vs SHE and below, the associative mechanism is dominant [50].

Besides, Pt is the best catalyst for the ORR. The reason that other metals cannot be as good as Pt is explained by the bonding energy of Pt and both O and OH species. In the study of Nørskov *et al.* [50], the oxygen binding energy between metal and O or OH was calculated using the equations below:

$$\mathrm{H_2O_{gas} + M \longrightarrow M{-}O + H_{2(gas)}}, \tag{4.29}$$

$$\mathrm{H_2O_{gas} + M \longrightarrow M{-}OH + \frac{1}{2}\,H_{2(gas)}} \tag{4.30}$$

where M is the metal.

According to Nørskov *et al.* [50], the metal elements, which have either higher or lower bonding energy with O, exhibit lower ORR activity. In the case of the stronger M−O bond, such as the Ni−O bond compared to that of Pt, the process of proton and electron transfer to the oxygen is slower. For Au, the bonding energy between Au and O is exothermic. Consequently, the state of oxygen on the Au surface is somewhat more unstable than that of moleqular oxygen. This instablity causes the ORR activity at Au to be lower as the transfer of protons and electrons to the oxygen is hindered. Defects and steps on the Pt surface strengthen this bond but do not enhance the ORR rate. According to computational theory, the kinetics of ORR can be faster if the oxygen binding energy on the metal compared to Pt is lower (Figure 5). This implies that metals such as Mo, Fe, Cu, Ni, and Ru may exhibit a higher ORR rate. The density functional theory (DFT) calculations indicate that the Pt skin coupled with another metal in an alloy (in the bulk phase) has lower oxygen binding energy than that of pure Pt [52, 53]. This phenomenon is confirmed by many practical studies [54–56]. Therefore, reducing the oxygen binding energy at the Pt surface is a method to improve the ORR activity of catalyst materials.

Another problem with the ORR is the blocking effect of products. If the kinetics of the reduction of OH to water (Equations 4.21, 4.24 and 4.25) are extremely fast, the equilibrium potential for the formation/desorption of OH

species is around 0.70 V vs RHE [12]. The OH species can cause a large overpotential due to the formation of blocking intermediates at the reaction sites. This phenomenon has motivated efforts to improve the reaction site accessibility of new catalyst materials by conducting studies with novel support materials and various surface studies [14, 33, 54, 57].

The ORR pathway on a glassy carbon disk electrode (GCDE) in acidic media is a 2-electron process involving peroxide formation [49, 58]. After the adsorption of an O_2 molecule on the active site, which is similar to Equation 4.18, the process is described as follows [49, 58]:

$$O_{2(ads)} + e^- \longrightarrow O^-_{2(ads,at-inert-site)} \quad \text{is the RDS,} \tag{4.31}$$

$$O^-_{2(ads,at-inert-site)} \longrightarrow O^-_{2(ads,at-active-site)} \quad \text{is the movement of oxygen.} \tag{4.32}$$

According to Taylor *et al.* [58], the $O^-_{2(ads)}$ is protonated in an acidic environment to form HO_2 species ($pH < pK_a \approx 4.8$) as described in the equation below:

$$O^-_{2(ads,at-active-site)} + H^+ \rightleftharpoons HO_2. \tag{4.33}$$

Then, the peroxide pathway proceeds similarly to the case of Pt and is described by the equation:

$$HO_{2(ads)} + H^+ + e^- \longrightarrow H_2O_{2(ads)}. \tag{4.34}$$

Finally, the peroxide can diffuse or decompose as shown in Figure 4.

$$H_2O_{2(ads)} \longrightarrow H_2O_{2(bulk)}. \tag{4.35}$$

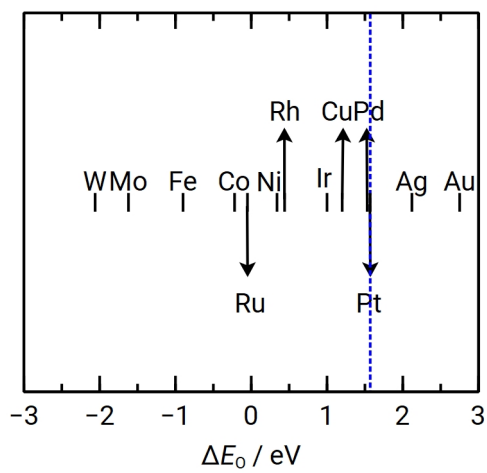

Figure 5. The oxygen binding energy values calculated from the heat of the reaction ($H_2O_{gas} + M \longrightarrow M{-}O + H_{2(gas)}$) with a quarter oxygen of coverage. The data are taken from Nørskov *et al.* [50].

The investigation of the ORR activity of the carbon material of the Pt catalyst can be used to elucidate the ORR activity of the carbon support and the (possible synergistic) effect of the carbon support on the ORR of the Pt catalyst.

4.1.4 Methanol Oxidation Reaction

The MOR is a 6-electron process that forms CO_2 as the final product. In acidic media, the overall process can be described by Equation 4.36 (at pH= 0).

$$CH_3OH + H_2O \longrightarrow CO_2 + 6\,H^+ + 6\,e^- \quad E^\circ = 0.016\,V. \tag{4.36}$$

At the Pt surface, the MOR mechanism can be described by the scheme in Figure 6 by Cohen *et al.* [59]. The MOR begins with the dehydrogenation steps (Equations 4.37 – 4.39):

$$CH_3OH_{(sol)} + Pt \longrightarrow Pt{-}(CH_3OH)_{(ads)}, \tag{4.37}$$

$$Pt{-}(CH_3OH)_{(ads)} + Pt_{(active\text{–}site)} \longrightarrow Pt{-}(CH_2OH)_{(ads)} + Pt + H^+ + e^-, \tag{4.38}$$

$$Pt{-}(CH_2OH)_{(ads)} + 2\,Pt_{(active\text{–}site)} \longrightarrow Pt_2{-}(CHOH)_{(ads)} + Pt + H^+ + e^-. \tag{4.39}$$

The formation of formaldehyde (Equation 4.40) can occur right after Equation 4.38.

$$Pt{-}(CH_2OH)_{(ads)} + Pt_{(active\text{–}site)} \longrightarrow H_2CO_{(sol)} + 2\,Pt + H^+ + e^-. \tag{4.40}$$

If Equation 4.40 does not take place, the MOR can follow two different pathways. The first pathway is the formaldehyde process (Equations 4.41 – 4.45).

$$Pt_2{-}(CHOH)_{(ads)} + Pt_{(active\text{–}site)} \longrightarrow Pt{-}(CHO)_{(ads)} + 2\,Pt + H^+ + e^-, \tag{4.41}$$

$$Pt{-}(CHO)_{(ads)} + 2\,Pt_{(active\text{–}site)} \longrightarrow Pt_2{-}(CO)_{(ads)}. \tag{4.42}$$

The states $Pt_2{-}(CO)_{(ads)}$ and $Pt{-}(CO)_{(ads)}$ are interchangeable (Equation 4.43).

$$Pt_2{-}(CO)_{(ads)} \rightleftharpoons Pt{-}(CO)_{(ads)} + Pt. \tag{4.43}$$

Additionally, the adsorption of a water molecule on $Pt_{(active\text{–}site)}$ (Equation 4.44) is crucial for the completion of MOR. The electrons released during this process are responsible for the MOR.

$$Pt + H_2O \longrightarrow Pt{-}OH_{(ads)} + H^+ + e^-. \tag{4.44}$$

The final step of this reaction pathway is the reaction between $Pt{-}CO_{(ads)}$ and $Pt{-}OH_{(ads)}$ to complete the oxidation of methanol (Equation 4.45).

$$Pt_2{-}(CO)_{(ads)} + Pt{-}OH_{(ads)} + Pt \longrightarrow CO_2 + 4\,Pt + H^+ + e^-. \tag{4.45}$$

The second reaction pathway is the formic acid reaction pathway, which starts after the dehydrogenation (Equation 4.39). The adsorption of water on Pt

(Equation 4.44) is also essential for this pathway. The later steps of the formic acid reaction pathway are described by Equations 4.46 – 4.48.

$$Pt_2{-}(CHOH)_{(ads)} + Pt{-}OH_{(ads)} \longrightarrow HCOOH_{(soln)} + 3\,Pt + H^+ + e^-, \quad (4.46)$$

$$Pt + HCOOH_{(soln)} \longrightarrow Pt{-}(COOH)_{(ads)} + H^+ + e^-, \quad (4.47)$$

$$Pt{-}(COOH)_{(ads)} + Pt_{(active\text{–}site)} \longrightarrow CO_2 + 2\,Pt + H^+ + e^-. \quad (4.48)$$

However, during the formaldehyde reaction pathway, $Pt{-}(COOH)_{(ads)}$ can also be formed, causing the reaction pathway to switche to the formic acid reaction pathway, also known as the indirect pathway. This occurss when either $Pt{-}(CHO)_{(ads)}$ (Equation 4.1.4) or $Pt_2{-}(CO)_{(ads)}$ reacts with $Pt{-}OH_{(ads)}$ (Equation 4.50).

$$Pt{-}(CHO)_{(ads)} + Pt{-}OH_{(ads)} + Pt_{(active\text{–}site)} \longrightarrow Pt{-}(COOH)_{(ads)} + 2\,Pt + H^+ + e^-, \quad (4.49)$$

$$Pt_2{-}(CO)_{(ads)} + Pt{-}OH_{(ads)} \longrightarrow Pt{-}(COOH)_{(ads)} + 2\,Pt. \quad (4.50)$$

Unlike the ORR, electron transfer is not the RDS for the MOR mechanism at positive potentials. However, scientists are particularly interested in identifying the processes that limit the MOR current at specific potentials (Figure 7) [23, 60, 61]. According to Chung *et al.* [23], the electrochemical impedance spectroscopy (EIS) studies have indicared that different processes limit the MOR

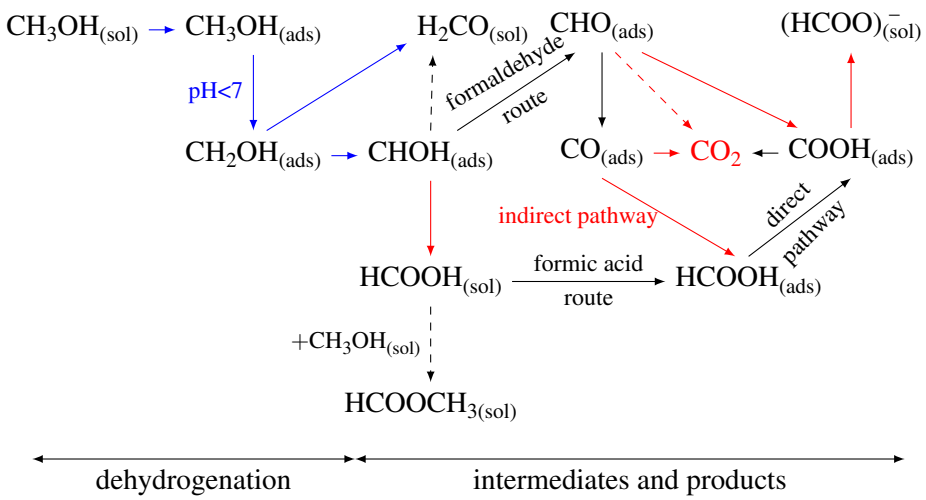

Figure 6. The pathways of methanol oxidation reaction at the Pt surface in acidic media [59]. The dashed lines indicate the routes that are unlikely to occur under typical measurement conditions. The red lines indicate the steps that require the $OH_{(ads)}$ adsorption (originating from water). The blue lines indicate the initial dehydrogenation pathway.

in specific potential ranges. The MOR initiates around 0.4 V vs RHE, and methanol adsorption on the Pt surface (Equation 4.37) is the RDS in the potential range of 0.4 – 0.6 V vs RHE. The formation of formate (Equation 4.47) can occur at the potential more positive than 0.5 V vs RHE [60]. According to the MOR mechanism (Figure 6), the presence of formate requires $Pt{-}OH_{(ads)}$ from the preceding step (Equation 4.46). Therefore, the water adsorption has already taken place, However at these potentials, water adsorption is weak, and $Pt{-}OH_{(ads)}$ is less exposed to the reaction, thereby insufficient for oxidising the intermediates to CO_2. The adsorption of water on the Pt surface (Equation 4.44) becomes faster at the potentials more above 0.6 V vs RHE, initiating the completion of methanol oxidation by oxidasing $CO_{(ads)}$-like intermediates into CO_2. The adsorption of methanol and water occurs simultaneously. Therefore, the oxidation of $CO_{(ads)}$ (Equation 4.45) and $COOH_{(ads)}$ (Equation 4.48) intermediates in the potential range of 0.60 – 0.75 V becomes the RDS. The rate of water dissociation (Equation 4.44) continues to increase as the potential is swept towards more positive potentials than 0.6 V, enhancing the MOR rate by increasing the coverage of $OH_{(ads)}$ on the Pt surface. In the potential range of 0.75 – 0.85 V, the oxidation steps of the final intermediates to CO_2 (Equation 4.45 and 4.48) in the formaldehyde and formic acid reaction pathways occur at simultaneously. However, oxidation mediated by $OH_{(ads)}$ (Equation 4.45) in the formaldehyde reaction pathway is faster than that mediated by the $Pt_{(active\text{–}site)}$ (Equation 4.48) in formic acid reaction pathway at this potential region. The overlapped peak at 0.75 V observed in cyclic voltammetry (CV) curves for the MOR, indicates the a shift in kinetics between the two oxidation pathways, with$CO_{(ads)}$ oxidation in the formaldehyde pathway (Equation 4.45) becoming faster than the oxidation in the formic acid pathway (Equation 4.48). The RDS in this potential region is considered the step converting $Pt{-}(CH_3OH)_{(ads)}$ to final intermediates. In the potential range of 0.850 – 0.975 V, the rate of water adsorption (Equation 4.44) on Pt increases, continally enhancing the coverage of $OH_{(ads)}$. This leads to a deficiency of Pt active sites for methanol adsorption, causing the current to decrease after reaching the MOR current peak. It is evident that the RDS encompasses steps from methanol adsorption (Equation 4.37) to the formation of $Pt{-}CO_{(ads)}$. After this potential range, the Pt surface is predominantly covered by $OH_{(ads)}$. However, if the Pt surface is continuously oxidised, the formation of $Pt{-}O_x$ in the potential range of 1.1 – 1.2 V is suggested to occur. The surface coverage with $Pt{-}OH_{(ads)}$ changes to $Pt{-}O_{(ads)}$ around 1 V. The $Pt{-}O_x$ surface has been found to be active toward the MOR, even at the open circuit potential. As the coverage of $Pt{-}O_x$ is electrochemically reduced during the reverse potential scan (cathodic direction), methanol can adsorb on the Pt surface. In this case, subsequent dehydrogenation of methanol at free Pt active sites facilitates the formation of $Pt{-}OH_{(ads)}$ on the$Pt{-}O_x$ surface, likely occuring at the adjacent surface between Pt and $Pt{-}O_x$. Thus, the completion of the MOR is facilitated

during the potential scan of cathodic direction.

According to the MOR mechanism, the poisoning of the Pt surface is

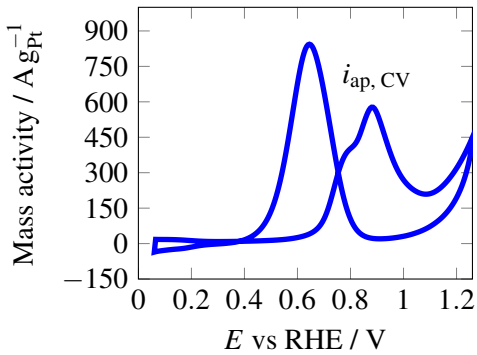

Figure 7. Mass activity measured in a solution of 1 mol dm^{-3} CH_3OH and 0.5 mol dm^{-3} H_2SO_4 saturated with argon.

atributed to the irreversible formation of Pt−$CO_{(ads)}$ at low potentials. While methanol dissociation can occur, there is not sufficient driving force and Pt−$OH_{(ads)}$ to oxidise $CO_{(ads)}$ to CO_2, particularly evident at potentials around 0.5 V. Consequently, $CO_{(ads)}$ can be oxidised at higher potentials where Pt−$OH_{(ads)}$ sites are available. If there are not enough Pt−$OH_{(ads)}$ sites, which would facilitate the reaction with Pt−$CO_{(ads)}$ (Equation 4.45), the number of Pt−$CO_{(ads)}$ sites increases subsequently and hinders the adsorption of methanol and water. This phenomenon causes the reduction of the current at specific potentials and the shift of the onset potential of MOR to more positive values, necessitating a greater driving force to oxidise the Pt−$CO_{(ads)}$ and free the Pt surface for the methanol adsorption. Furthermore, the decrease in methanol concentration in the electrolyte solution slightly increases the proportion of formaldehyde, which is the intermediate in the main route to form $CO_{(ads)}$ at the electrode surface. Both formaldehyde and formic acid can undergo oxidation to produce $CO_{(ads)}$. Cohen *et al.* [59] hdemonstrated that the increase of temperature causes the strengthening of the Pt−$CO_{(ads)}$ bond. However, the slightly lower coverage of CO on the electrode surface is due to the thermal activation enhancement of Pt−$OH_{(ads)}$ formation. The sensitive surface of Pt can adsorb sulfate anions from the H_2SO_4 electrolyte. Adsorption of bisulfate reduces the overall MOR current. However, the impact of anion coverage may be minimal and negligible under appropriate measurement conditions, such as starting CV with a cathodic potential scan at 1.26 V in 0.1 mol dm^{-3} H_2SO_4 [59]. This CV measurement condition helps mitigate the bisulfate anion adsorption by promoting coverage of the oxide layer .

In the previous discussion, the importance of Pt−$OH_{(ads)}$, Pt−O_x and CO_{ads} coverage in the MOR was addressed. It is evident that increasing the oxide coverage on the Pt surface improves both the MOR activity and stability of the catalyst [23, 59]. Additionally, the resistance of the Pt catalyst to CO_{ads}

poisoning can be enhanced by promoting the formic acid reaction pathway (Figure 6) and weakening the adsorption bond between Pt and $CO_{(ads)}$. The binding energy of Pt and $CO_{(ads)}$ can be reduced by alloying Pt with other metals, akin to the strategy discussed in the previous ORR section. Mailard *et al.* [62] demonstrated that Pt coupled with Ru mostly bypasses $CO_{(ads)}$ formation by favouring the formic acid reaction pathway. In the case of CeO_2, CeO_2 facilitates theoxidation of $Pt{-}CO_{ads}$ to CO_2 (Equation 4.51 and 4.52) via the adsorbed OH_{ads} on the CeO_2 surface.

$$CeO_2 + H_2O \longrightarrow CeO_2{-}OH_{(ads)} + H^+ + e^-, \tag{4.51}$$

$$Pt{-}CO_{ads} + CeO_2{-}OH_{(ads)} \longrightarrow Pt + CeO_2 + CO_2 + H^+ + e^-. \tag{4.52}$$

Moreover, CO oxidation by catalysts with a fluorite structure (Equation 4.7 – 4.10) can occur concurrently, described generally by Equation 4.53.

$$Pt{-}CeO_2 + CO \longrightarrow Pt{-}CeO_{2-x} + x\,CO_2. \tag{4.53}$$

4.2 Optimisation of Synthesis Methods

4.2.1 Ethylene Glycol Reduction Method

If the synthesis methods for Pt NPs are classified by the reducing chemicals used such as ethylene glycol (EG), H_2, $NaBH_4$, H_2O_2 and etc, the EG reduction method is one of the most popular choices. The reaction pathway of this method has not been conclusively reported because many different Pt precursors and reducing chemicals can be used. The reaction pathway proposed by Yao *et al.* (Figure 8) [63] demonstrates the subsequent reduction of Pt (from the $[PtCl_4]^{2-}$ ions of K_2PtCl_4) to form Pt_nCl_x cluster. However, if H_2PtCl_6 is used, both $[PtCl_6]^{2-}$ and $[PtCl_4]^{2-}$ ions are present during the EG reduction synthesis.

The reaction pathway of the EG reduction is easier to be explained using the oxidation route of EG (Figure 9) [64, 65]. The EG is an alcohol and weak reducing agent. At the same time as the oxidation of an alcohol at Pt surface is observed, the formation of $CO_{(ads)}$ takes place. Studies by Schrader *et al.* [65] reveal that the presence of both $CO_{(ads)}$ and $OH^-_{(ads)}$ at the surface of Pt colloid NPs using nuclear magnetic resonance spectroscopy, infrared spectroscopy and electrospray-ionization mass spectrometry. No C−H vibrations are recorded from the Pt colloid NPs. The presence of $OH^-_{(ads)}$ results from the presence of water in the EG system. Water adsorption can probably occur as demonstrated in Equation 4.44. The surface of Pt colloid NPs is not fully covered with the $CO_{(ads)}$. Instead, $CO_{(ads)}$ tends to be displaced by the adsorbed OH^- species. A study on the synthesis of carbon-supported PtRu catalyst [64] confirms the presence of both oxalic and glycolic acids in the reaction solution at the end of the experiment. These aldehydes are unstable in synthesis conditions and are oxidised to oxalic and glycolic acids, with glycolic acid being the dominant

product of EG oxidation. Glycolic acid also acts as a stabilising reagent in this synthesis process, existing as glycolate anions at high pH.

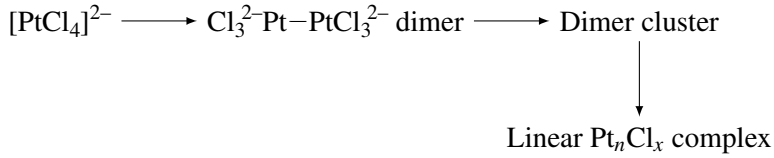

Figure 8. The proposed reaction pathway of ethylene glycol reduction method to synthesise Pt nanoparticles by Yao *et al.* from the K_2PtCl_4 precursor [63].

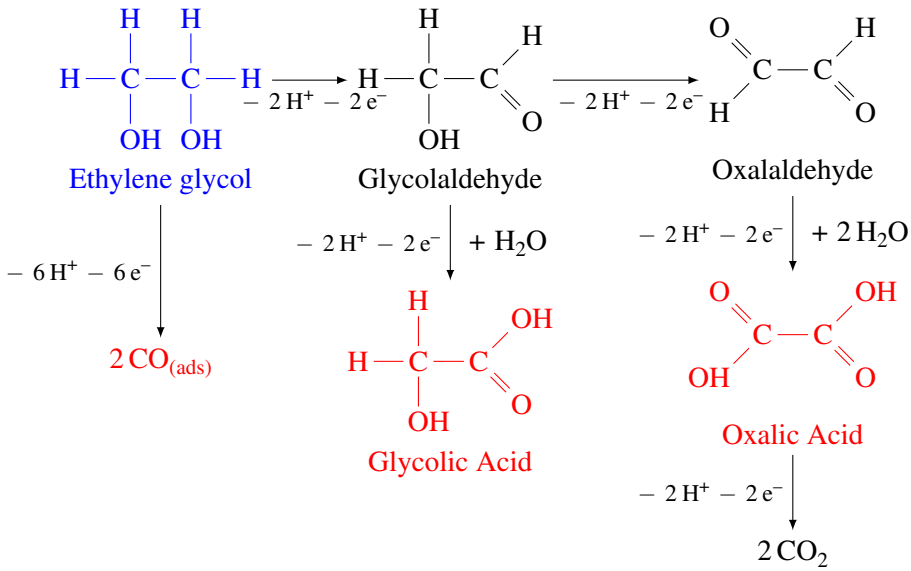

Figure 9. The ethylene glycol oxidation route that provides the electrons for the Pt reduction during the ethylene glycol synthesis [64]. The blue compound indicates the starting compound and the red compounds indicate intermediate products. Carbon dioxide is the final product.

4.2.2 Nucleation and Growth of Metal Particles

During the synthesis of metal NPs, the formation of metal NPs occurs subsequently from the initial formation of metal nuclei to the growth of bigger metal complexes. Therefore, the nucleation, which describes the formation of nuclei, is a crucial step to control the crystal structure and the size distribution of Pt NPs. A high level of control of the crystallisation is hard to achieve without an understanding of the details of the nucleation process. Although many nucleation models [66, 67] have been proposed, the classical nucleation theory (CNT) is still serving as a guideline by many reasons. The CNT is based on the Gibbs energy changes during the condensation of the droplets from the vapor phase, and this fundamental knowledge is also applicable to the crystallisation of solids from the solution phase [67–69]. According to the CNT (Figure 10), the Gibbs free energy change for the formation of a cluster (ΔG) is the sum of free energy change for the phase formation (ΔG_{v}) and the free energy change for the formation of a surface (ΔG_{s}):

$$\Delta G = \Delta G_{\mathrm{v}} + \Delta G_{\mathrm{s}}. \tag{4.54}$$

In the perspective of CNT crystallisation from the solution, the term ΔG_{v} demonstrates that the crystallisation of supersaturated solution is spontaneous. This term is negative as the crystals from the solid state are thermodynamically more stable than the solvated precursors in the liquid phase. The growth of the solid/liquid interface increases the free energy proportionally to the surface area of the cluster (ΔG_{s}). Therefore, the growth of the cluster is determined by the competition of ΔG_{v} and ΔG_{s} terms. The term ΔG_{v} promotes the growth while ΔG_{s} relates to the dissolution of the cluster. At the initial stage, the radii (r) of the cluster are small, and the term ΔG_{s} dominates, causing the solid to form. The small clusters are typically dissolved. However, the radii of the cluster increase along with the increase of ΔG until the critical size ($\mathrm{r_c}$). At this point ($\mathrm{r} = \mathrm{r_c}$), the cluster becomes stable, and the rapid change of ΔG_{v} decreases ΔG continuously from this point further ($\mathrm{r} > \mathrm{r_c}$). As a result, the cluster growth is energetically favourable, leading to the formation of nuclei. In addition, the steady-state rate of nucleation (J) can also be described as [67]:

$$J = Ae^{-\frac{\Delta G_{\mathrm{crit}}}{kT}}, \tag{4.55}$$

where A is the pre-exponential factor (10^{30} $\mathrm{cm^{-3}\,s^{-1}}$) and k is the Boltzmann's constant and T is absolute temperature.

As the crystallisation from solution is controlled by the Gibbs free energy, the crystallisation process can be manipulated by controlling the factors that influence the system Gibbs free energy. The surfactants can control/influence the surface free energy (ΔG_{s}). Each metal precusor has unique ΔG_{v} and ΔG_{s} values for nuclei formations. The changes in the reaction environment can influence the

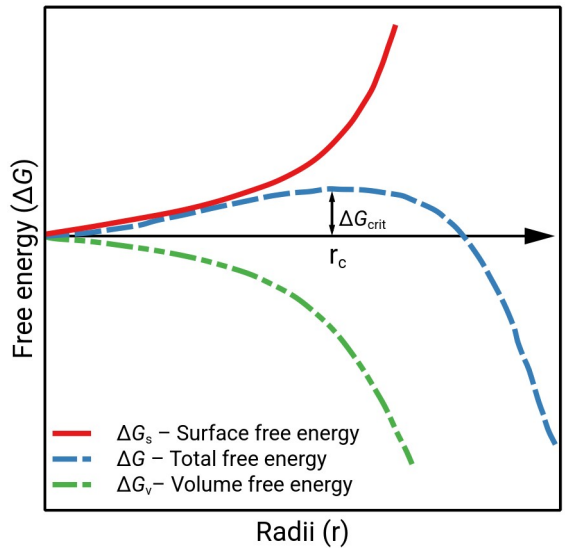

Figure 10. The Gibbs free energy changes during the nucleation of particles.

stability of nuclei. Therefore, in the EG reduction method applied for Pt deposition, besides capping reagents, the nucleation kinetics can be controlled by changing the reducing reagents (hydrogen gas [70], formaldehyde [71, 72], formic acid [71, 72], citric acid [70] and sodium borohydride [71, 73]) and stabilizers (OH^- [70], acetate [74], sodium chloride, glycolate [64, 75]). In addition, the temperature control [76] is important because the steady-state rate of the nucleation is influenced by this factor.

The CNT can also be interpreted by the concentrations of reactants in the reaction system as demonstrated in Figure 11 [68]. When applied for the Pt deposition using the EG reduction method, the process of nucleation can be interpreted (as given in Figure 8) by the accumulation of $Cl_3^{2-}Pt-PtCl_3^{2-}$ dimer, the self-assembling process to form the dimer clusters at the critical concentration and growth of Pt_nCl_x complex in the diffusion regime. Therefore, this crystallisation process can be controlled by increasing of expected participating species to obtain the supersaturated concentration level of products in the reaction solution and the change of solubility of the products at the critical concentration.

4.2.3 Sedimentation of Metal Particles onto The Supports

When the initial Pt complexes are formed, the growth of the complexes to form Pt NPs may follow different pathways [77, 78]. This section is more concentrated on the later step where the Pt NPs are deposited onto the carbon support. If the EG is used as the reducing reagent, the Pt NPs tend to stay in the colloid solution if the reaction solution is alkaline or the NPs are stabilised. The precipitation of the Pt NPs onto the carbon support surface requires the driving force from other

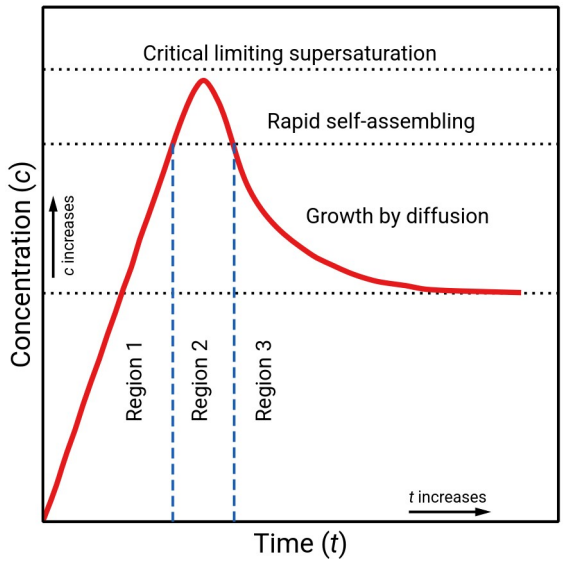

Figure 11. Kinetics of the nucleation process proposed by LaMer and Dinger [68].

factors than the EG.

The first strategy is using the stronger reducing reagents (formaldehyde, formic acid, or sodium borohydride) to fully reduce Pt species to Pt^0. The proposed reaction mechanism [79] in the case of formaldehyde and formic acid is described as below.

$$[PtCl_6]^{2-} + H{-}CHO + 2\,OH^- \longrightarrow [PtCl_4]^{2-} + CO + 2\,Cl^- + 2\,H_2O, \quad (4.56)$$

$$[PtCl_4]^{2-} + H{-}CHO + 2\,OH^- \longrightarrow Pt^0 + CO + 4\,Cl^- + 2\,H_2O. \quad (4.57)$$

$$[PtCl_6]^{2-} + H{-}COOH \longrightarrow [PtCl_4]^{2-} + CO_2 + 2\,Cl^- + 2\,H^+, \quad (4.58)$$

$$[PtCl_4]^{2-} + H{-}COOH + H_2O \longrightarrow Pt^0 + CO_2 + 4\,Cl^- + 2\,H^+ + H_2O. \quad (4.59)$$

In the case of sodium borohydride, in alkaline media, the $[BH_4]^-$ releases electrons in the two reactions given in Equations 4.60 and 4.61 [80, 81].

$$BH_4^- + 2\,H_2O \longrightarrow HBO_2 + 3\,H^+ + 2\,H_2 + 4\,e^- \quad E^0 = -0.98\,V, \quad (4.60)$$

and/or

$$BH_4^- + 4\,OH^- \longrightarrow BO_2^- + 2\,H_2O + 2\,H_2 + 4\,e^- \quad E^0 = -1.67\,V. \quad (4.61)$$

These released electrons participate in the reduction of Pt species to Pt^0, according to equations described below [80].

$$[PtCl_6]^{2-} + 2\,e^- \longrightarrow [PtCl_4]^{2-} + 2\,Cl^- \quad E^0 = 0.68\,V, \quad (4.62)$$

$$[PtCl_4]^{2-} + 2\,e^- \longrightarrow Pt^0 + 4\,Cl^- \quad E^0 = 0.755\,V. \quad (4.63)$$

The second strategy to achieve precipitation onto carbon support is to regulate the reaction environment. In this case, pH is controlled to reach the expected value by using either acids or water to reduce the solutions pH after the reaction. The precipitation of Pt onto carbon support surface can happen due to the different charge sign of Pt colloid NPs and the carbon support (Figure 12). This phenomenon can be explained by using zeta potential, which is the potential difference between the bulk fluid and the stationary layer of fluid at dispersed particle. When the $pH \leq 9$, the zeta potential of carbon support becomes positive, while the zeta potential of Pt NPs tends to be negative and the deposition is taking place [82]. The CeO_2 NPs can also be deposited onto the carbon support by the regulation of pH. This strategy has been applied in many studies [71, 83–85]. Nevertheless, the functionality groups on carbon surface can cause the differences amongst carbon support materials in the dependence of zeta potentials and pH values.

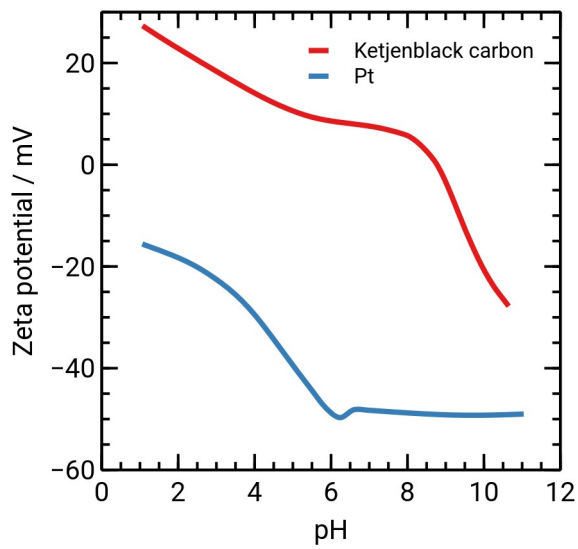

Figure 12. The dependence of zeta potentials of Pt nanoparticles and Ketjenblack carbon on solution pH values. Adapted from Oh *et al.* [82].

The precipitation of the Pt NPs can also be done by the rapid change of Gibbs free energy using an exothermic shock. Solla-Gullón *et al.* [86] synthesised the colloid Pt using H_2 gas as the reducing reagent. After that, Solla-Gullón *et al.* used two pellets of NaOH to precipitate the Pt out of the solution. The dissolution of two NaOH pellets in water initiated an exothermic process providing a sudden heat in the reaction solution and the change of pH of the solution.

The last strategy is the kinetic control of the nucleation. The stabilizer composition and temperature of reaction are the keys for this strategy. As

glycolate is a good stabilizer in the EG reduction method, the control of glycolate concentration is crucial. The dissociation of glycolic acid to glycolate is controlled by the pH of the reaction solution (Figure 13) [64]. The concentration of glycolate is maximum as pH $\geq$ 6. Therefore, higher pH values are suitable for the growth of Pt NPs. The increase of synthesis temperature enhances the steady-state rate of nucleation (Equation 4.55). By manipulating these two parameters, the Pt species can be accumulated, reaching the supersaturated concentration point (as explained in Chapter 4.2.2). This, in turn, triggers the self-assembly and growth of Pt clusters on carbon supports.

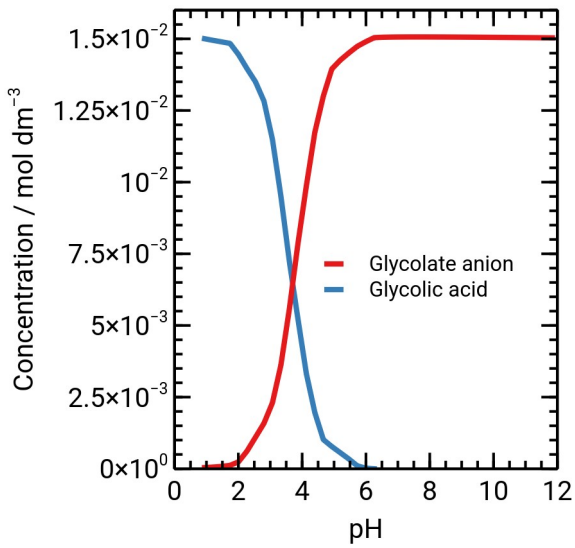

Figure 13. The dependence of glycolate anion and glycolic acid molecule concentrations on the pH of solution. The total concentration of glycolic acid is 1.5 $\times 10^{-2}$ mol dm^{-3}.

4.2.4 Effect of Energy Providing Methods on Catalyst Parameters

Boiling is the most popular method to provide energy as heat to the reaction system. The temperature of the reaction mixture increases slowly until reaching the reaction temperature. Most heating devices provide a sine temperature profile around the reaction temperature in the reaction mixture. If the refluxing system coupled with oil bath is used, the solvent should have boiling point higher than the reaction temperature [64]. Heating with the stainless steel autoclave can endure high pressure and solvent can have the boiling point lower than the reaction temperature [87]. The refluxing system with oil bath is suitable for a one-pot synthesis, in which both solid (carbon) and liquid compounds are presented. Otherwise, heating with the stainless steel autoclave is more suitable for the condensation of crystals from vapor, however, this method is still applicable for one-pot synthesis.

The microwave (MW) heating, so-called dielectric heating, method has gained the interest from researchers because of the robust and fast heating by MW radiation. MW are the electromagnetic waves that have both electric and magnetic components. During the MW heating, the charge particles receive a force from the electric field. This force results in the charge movements, rotation and even polarization. The spontaneous switch in moving directions of particles caused by both MW components heats up these particles due to the friction forces. The MW frequency range is 918 MHz – 2.45 GHz corresponding to wavelengths of 33.3–12.2 cm. Nevertheless, the most popular frequency is 2.45 GHz because the dielectric property at this frequency is suitable to heat up water molecule and can be used in many different fields such as industrial, scientific, and medical fields. The two effects of MW heating are described by the ε', and ε''. The ε' indicates the ability of a molecule to be polarized by an electric field while ε'' reveals the ability of a medium to be heat up by dielectric energy. Thereafter, the dielectric loss tangent, $\tan\delta$, is used to assess the ability of the system to be heat up by the MW radiation at a certain frequency and temperature [88].

$$\tan\delta = \frac{\varepsilon''}{\varepsilon'}. \tag{4.64}$$

Therefore, the selection of solvent to provide a suitable reaction conditions is important. The $\tan\delta$ values (>0.1) for some solvents at 20 °C are shown in Figure 14 [89]. The popular solvents for the polyol synthesis method such as EG, ethanol and methanol have high $\tan\delta$ values (>0.6). In contrast, water have quite low $\tan\delta$ value (ca. 0.1). Since EG and water are two popular compounds in a reaction mixture, the huge different $\tan\delta$ values (Figure 14) of these two solvents have gained interest for the use of microwave in Pt catalysts synthesis. Sharma *et al.* [90] have studied the influence of water content in mixture of EG and water to the synthesis of Pt NPs using microwave power at 200 W at 140 °C with the reaction time 150 s. The influence of water volume fraction during the Pt deposition, in which the initial Pt concentration was 5 mmol dm^{-3}, on the electrochemically active surface area (ECSA) is shown in Figure 15.

Unlikely to boiling, the MW heating method is influenced by the volume of the reaction mixture, which may result in the loss of absorbance. This effect is described by the penetration depth, D_p, which is connected to $\tan\delta$ [91].

$$D_p = \frac{\lambda_0}{2\sqrt{2\pi}\sqrt{\varepsilon'[\sqrt{1+(\varepsilon''/\varepsilon')^2}-1]}}, \tag{4.65}$$

where λ_0 (cm) is the microwave wavelength.

In addition to heating, MW radiation has other effects on the reaction mixture. With a suitable choice of solvents, the reactant can be heated up rapidly by microwave energy while the solvent itself does not absorb the wavelength. This effect in the preparation of intercalation compounds results in a higher

crystallinity degree [92, 93]. In fact, the Pt NPs particles prepared by the microwave heating method have sharp peaks for Pt individual planes in X-ray diffraction (XRD) measurement, i.e. large Pt crystallites are formed [90, 94]. When the synthesis mixture contains both solid and organic solvent, the microwave energy heats up the solid phase and the solvent absorbs the heat from the solid phase rather than from the microwave radiation. This advantage enables the use of microwave heating method in atmospheric pressure for the synthesis

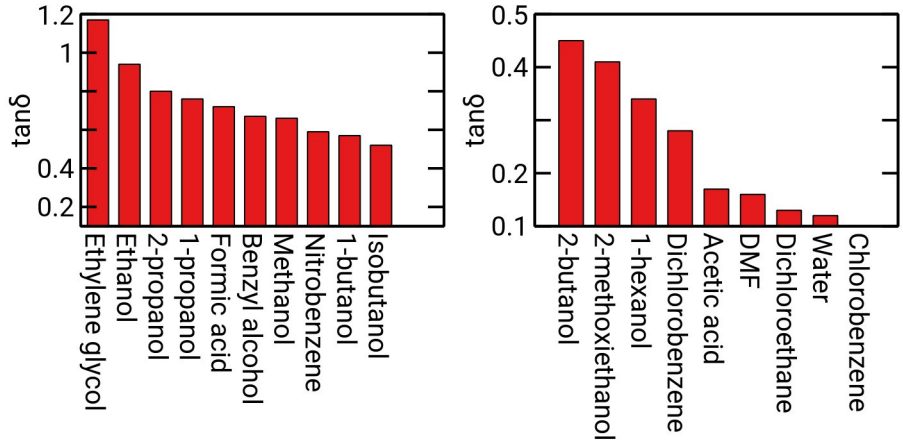

Figure 14. The dielectric loss tangent values for different solvents. Data are adapted from Nunes *et al.* [89].

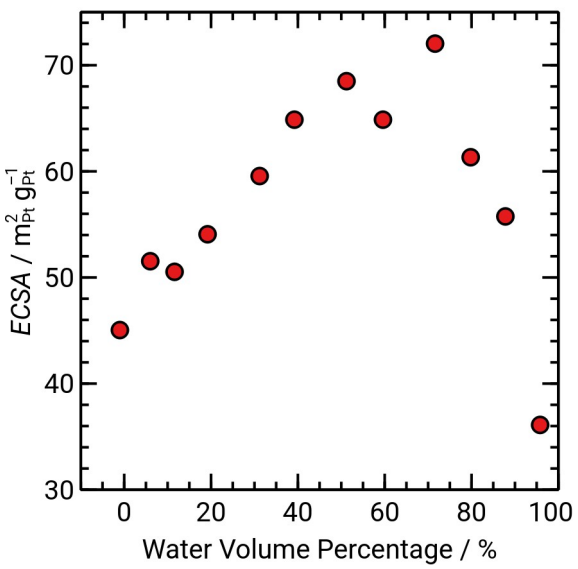

Figure 15. The influence of water volume fraction on the electrochemically active surface area (ECSA) of Pt catalyst prepared with the ethylene glycol reduction synthesis method. Data is taken from [90].

that is usually carried out in the autoclave at high pressure and temperature [95]. Many studies have reported that microwave radiation enhances the rate of hydrolysis and esterification reaction [95, 96]. Additionally, the enthalpy of MW energy affects on the vibration of a molecule and the entropy affects the alignment of molecules, collectively lowering the Gibbs free activation energy of a reaction [97].

The last heating method is the use of ultrasound for the synthesis of metal NPs. An usual ultrasonic bath in a chemistry laboratory uses the frequency from 20 to 40 kHz and the wavelength ca. < 1.9 cm [98]. The heating effect of ultrasound radiation is quite unique compared to other heating methods. The formation and collapse of bubbles cause extremely high rates of cooling and heating ($> 10^{10}$ $\mathrm{K\,s^{-1}}$) [98]. This effect enables the ultrasound radiation to deposit and synthesise various nanostructured materials. In addition, the high intensity of ultrasound radiation deliver some chemical effects such as hydrolysis and sonochemical reduction due to the possible formation of H_2 and H_2O_2 from water. The syntheses using ultrasound radiation, so-called sonochemical syntheses, are favorable because the reaction mixture can emulsify and disperse well various chemical species, and the high intensity of ultrasound can induce some surface damages and defects. These effects can be applied to synthesise a well disperse nanoparticle (NP) catalysts. In fact, the sonochemical synthesis method is applied to deposit various metals onto a support material [98], and synthesise colloid metals and metal oxides like CeO_2 [99, 100].

4.2.5 Synthesis Methods of CeO_2 Modified Catalysts

The most popular method to synthesise CeO_2 crystals is solvothermal synthesis method using a stainless steel autoclave [87, 101]. In the conventional solvothermal synthesis method, an aqueous solution of NaOH and a cerium salt are used. By controling the NaOH concentration (Table 4), it is possible to change the morphology of CeO_2 crystals [87]. In the comparison amongst these CeO_2 crystal morphology, the a Pt catalyst coupled with rod-shaped CeO_2 crystals were the most active material towards the MOR [20, 47]. The rod-shape of CeO_2 crystals can be synthesised using ultrasound radiation [99].

The morphology of the CeO_2 NPs can also be controlled by replacing NaOH with different amino acids in the urea reaction mixture [101, 102]. The use of amino acids to control the CeO_2 characteristics was studied by Atla *et al.* [101], in which they used L-histidine in an urea buffer solution to create the flower-shaped CeO_2 crystals. The flower-shaped CeO_2 was found to be more active towards the CO oxidation compared to other CeO_2 morphologies [48].

As the number of junctions between Pt and CeO_2 is crucial for electrochemical activity of the catalyst, Chen *et al.* [47] attempted to deposit Pt NPs onto CeO_2 crystals as a support material. After that, the $Pt{-}CeO_2$ complexes were deposited onto a carbon support. Unfortunately, the

Table 4. The dependence of the CeO_2 crystal morphology on the NaOH concentrations in the 24-hour solvothermal synthesis using the initial Ce^{3+} concentratrion ca. 0.05 mol dm^{-3}. Data are taken from Mai *et al.* [87].

c_{NaOH} / mol dm^{-3}	Synthesis temperature / °C	Crystal shape
0.01	100	polyhedra
0.01	180	polyhedra
1	100	polyhedra, rods
3	100	polyhedra, rods
6	100	rods
6	140	rods, cubes
6	180	cubes
9	100	rods

electrochemical activity of these Pt−CeO_2/C complex catalysts was very low although the Pt NPs were well-dispersed on the CeO_2 crystals.

4.3 Characterisation Methods

4.3.1 Low-Temperature Nitrogen Sorption (LTNS)

The low-temperature nitrogen sorption (LTNS) is the popular method to characterize the porosity of the studied materials. Valuable information such as specific surface area (S_{BET}), and total pore volume (V_{total}) can be obtained from the dependence of total adsorbed nitrogen volume (V_{ads}) at −196 °C (77 K) on relative pressure value (P/P_0) [103, 104]. The data can be interpreted following the conventional method by using Brunauer-Emmett-Teller (BET) method [103, 104].

$$\frac{P}{V_{ads}(P_0 - P)} = \frac{1}{V_m c} + \frac{c-1}{V_m c} \cdot \frac{P}{P_0}, \tag{4.66}$$

where c is the BET constant and V_m is the volume of nitrogen for the completion of unimolecular adsorbed layer, P is the absolute pressure, and P_0 is the saturation pressure of the gas. As the Equation 4.66 presents a form of straight line relationship, both c and V_m can be determined from the slope and intercept of this line.

$$\text{slope} + \text{intercept} = \frac{1}{V_m}, \tag{4.67}$$

$$c = \frac{1}{V_m}. \tag{4.68}$$

The experimental relationship of the Equation 4.66 is nearly linear in the region of P/P_0 from 0.05 to 0.35. The S_{BET} is determined using the V_m value [103, 104].

$$S_{BET} = \frac{V_m \cdot N_A \cdot A_{\text{cross-section}}}{M \cdot m_{\text{sample}}} \tag{4.69}$$

where $N_A = 6.02 \cdot 10^{23}$ molecules per mole is the Avogadro constant, $A_{\text{cross-section}} = 0.162$ nm^2 is the molecular cross-section area of N_2 adsorbate at 77 K [103, 104], M is the molar mass of N_2 adsorbate and m_{sample} is the mass of sample used for the experiment.

The V_{total} is usually estimated at the nearly specifc P/P_0 value ($\frac{P}{P_0} = 0.95$), where the N_2 adsorption is nearly saturated.

$$V_{\text{total}} = \frac{PV_{\text{ads}}V_{\text{molar}}}{RT}. \tag{4.70}$$

The t-plot method can be used to estimate the microporous area ($S_{\text{micropores}}$) value from the S_{BET} value. According to Boer *et al.* [105], the t_{stat} represents the statistical thickness of the adsorbed layer and S_{external} stands for the surface area of meso- and macro-porous area.

$$t_{\text{stat}} = \sqrt{\frac{13.99}{\log\frac{P}{P_0} + 0.034}}. \tag{4.71}$$

The S_{external} can be found from the slope at high relative pressure, and volume of micropore ($V_{\text{micropores}}$) can be estimated from the intercept value (see Equations 4.66 and 4.67).

$$S_{\text{micropores}} = S_{\text{BET}} - S_{\text{external}}. \tag{4.72}$$

As the BET method may over-estimate the adsorption parameters, the second method is used to analyze the LTNS results using the non-local density functional theory (NLDFT) for carbon materials within the SAIEUS software [106], so-called "Carbon-N2-77, 2D-NLDFT Heterogeneous Surface" [107]. The surface areas and pore volumes can be estimated via the cummulative area and cummulative volume from the output of the SAIEUS software.

$$N(\frac{P}{P_0}) = \int_{w_{\text{min}}}^{w_{\text{max}}} N(\frac{P}{P_0}, w) f(w) dw, \tag{4.73}$$

where $N(\frac{P}{P_0})$ is the adsorption isotherm data point, w is the pore width and $f(w)$ is the pore width distribution function. The result from SAIEUS software is more reliable since a specific NLDFT model was used for carbon surface. Besides, the combination of second derivative from the L-curve method [108], in which the roughness is taken into account, and a regularization method by employing non negativity contrainsts [109] delivers stable and meaningful results.

4.3.2 Characterisation of Structure and Morphology

X-ray diffraction is the most popular method to characterize the structural phases and crystal structure that are present in the catalyst. The effective crystallite size,

D_{Scherrer}, can be estimated from the diffraction pattern of powder using the Scherrer equation [110].

$$D_{\text{Scherrer}} = \frac{K\lambda}{\beta \cos\theta}, \tag{4.74}$$

where the integral breadth of the profile is β, a cubic crystallite shape has a factor $K = 0.9$, θ is the Bragg's angle and the X-ray wavelength is λ [110].

The TOPAS software is the popular software for modeling of the experimental diffraction results. The first approach is to implement the simple mathematical form to characterize the profile fitting by peak shape functions (PSF). The popular PSF are Gaussian, Lorentizian, Voigt, pseudo-Voigt and Pearson VII functions. However, these functions are limited to fit the profile well in the whole range of 2θ angles without using a large number of parameters. Therefore, this approach can result in correlation problems, loss of uniqueness, and instability of the refinement procedure [110]. The second approach is using the well-known profiles to generate a learned PSF [110]. Unfortunately, this approach requires non-overlapping peaks in the whole 2θ angle range, and the learned PSF should be pre-defined. The last approach is known as the direct convolution approach [110]. The observed profile shape, $Y(2\theta)$, is described by a process, where the convolutions of various function are implemented [110].

$$Y(2\theta) = W \otimes F_1(2\theta) \otimes F_2(2\theta) \otimes ... \otimes F_n(2\theta), \tag{4.75}$$

where $\otimes$ describes the convolution process, and W is the source emission profile, F is a function.

Another powerful method to investigate the microstructure of catalysts is Raman spectrometry. This technique is widely used to study the graphization and microstructure of carbon [111–113]. The Raman spectrum (with the wavenumber below 1000 cm^{-1}) can be used to characterize the catalysts containing the CeO_2 [114–117].

Metal particles in the catalysts can be visualized in a nanometer scale by using high-resolution transmission electron microscopy (TEM) and scanning electron microscopy (SEM) methods. Although the working principles of these two methods are different, the TEM and SEM are powerful methods to observe the structure and morphology of catalysts [87, 118–121].

4.3.3 Cyclic Voltammetry (CV)

The CV is a popular method to investigate capacitive behaviour of catalyst supports and the electrochemical activity of a catalyst material in an quiescence solution. In the CV measurement, the electrode potential is swept at constant potential scan rate ($\text{V}\,\text{s}^{-1}$). The change of potential during the experiment is demonstrated in the Figure 16. The CV measurement is conducted with a potentiostat in a three-electrode system, which is demonstrated in the Figure 17. The working scheme of the potentiostat is described in the Figure 18 [122].

According to the scheme, there is the slight difference between the applied potential (E_{applied}) by the potentiostat and the working electrode potential (E_{working}) at the working electrode (WE), which is caused by the ohmic drop in the solution. Therefore, the E_{working} can be determined following the Equation 4.76.

$$E_{\text{working}} = E_{\text{applied}} - IR. \tag{4.76}$$

The current in CV measurements can be processed and presented in a

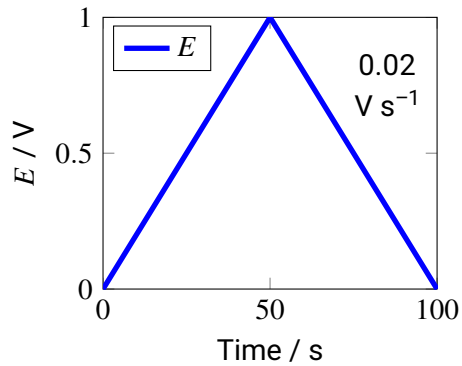

Figure 16. The function of applied potential in CV measurement.

suitable plot for the analysis, e.g. as a dependence of mass activity (Figure 7) or capacitance (Figure 19) on electrode potentials. The mass activity (MA), j and C values are usually used for the analysis instead of the measured I value because these values outline the difference of the catalysts or catalyst support. The equations to calculate the mentioned parameters are described below.

$$MA(\mathrm{A\,g_{Pt}^{-1}}) = \frac{I}{m_{\text{Pt}}}, \tag{4.77}$$

$$j(\mathrm{A\,m^{-2}}) = \frac{I}{A}, \tag{4.78}$$

$$C(\mathrm{F\,g^{-1}}) = \frac{I}{m\nu}. \tag{4.79}$$

Where m_{Pt} (g) and m (g) are mass of Pt and the mass of catalyst material on the electrode surface, respectively. The A ($\mathrm{m^2}$) and ν ($\mathrm{V\,s^{-1}}$) are the area of the electrode surface and the potential scan rate, respectively.

In one-electron transfer process, the peak current (I_{p}) of the reaction in the case of irreversible processes is proportional to the square root of potential scan rate [123]. By assuming that the one-electron is the reduction reaction of A to B, the dependence of I_{p} of a reversible process on the potential scan rate is described as below [123].

$$\mathrm{A} + \mathrm{e^-} \rightleftharpoons \mathrm{B}. \tag{4.80}$$

$$I_p = 2.69 \cdot 10^5 A D^{1/2} [A]_{bulk} \nu^{1/2} \quad \text{at 298K (mass transfer limited).} \tag{4.81}$$

Reversible and irreversible process can be distinguished using the peak potential seperation (ΔE_{pp}).

$$\Delta E_{pp} = |E_p(\text{anode}) - E_p(\text{cathode})|, \tag{4.82}$$

where E_p is the peak potential of anodic peak or cathodic peak [123].

In the case of reversible one-electron process, the ΔE_{pp} in the low ν values is around 57 mV at 298 K and is independent of electrode potential sweep rate [123].

The process of ORR and MOR is irreversible, irrespective of measurement technique. As it mentioned in the subsection 4.1.4, the reverse peak at the cathodic potential scan direction (Figure 7) is caused by the $Pt{-}O_{(ads)}$ reduction and CH_3OH dehydrogenation at the refresh Pt surface [23]. Later, the current decreases in more negative potential because due to the lack of free Pt surface

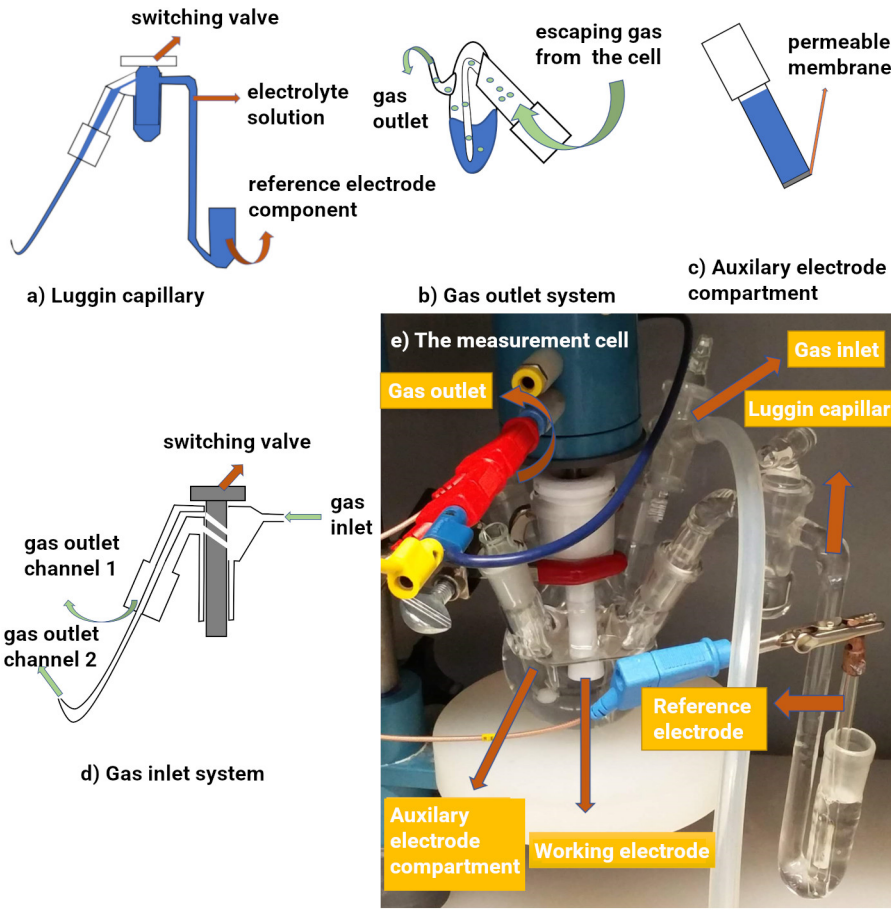

Figure 17. Three electrode system for electrochemical measurements (details are given in the figure).

and the lower potential driving force. This is different from the formation of the anodic peak, which is mentioned in the previous section.

Another application of CV is to describe the capacitive behaviour of catalyst supports or catalysts (Figure 19). The adsorption of C=O groups can be observed in the potential region from 0.55 to 0.60 V, which is caused by a redox

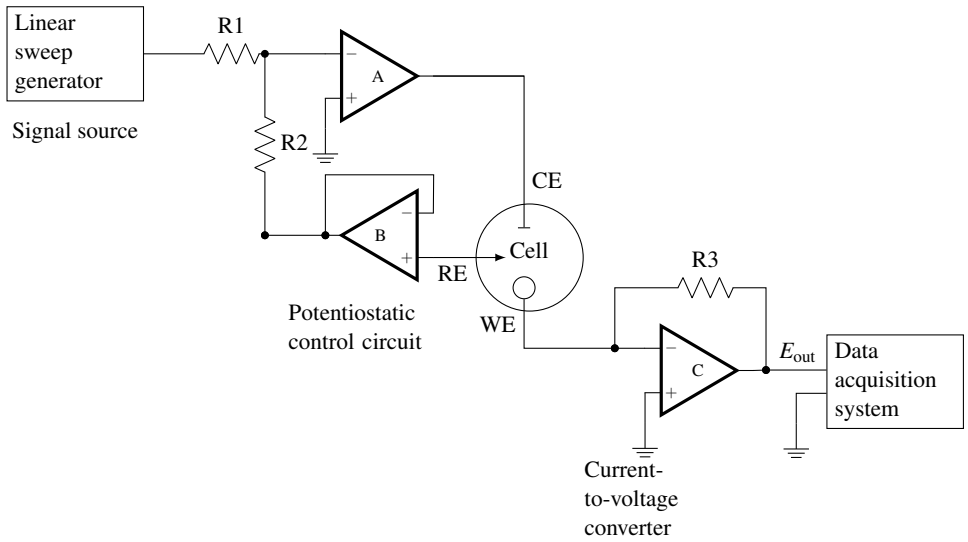

Figure 18. The electric scheme for the measurement with a potentiostat in the 3-electrode system. Figure is adapted from Skoog *et al.* [122].

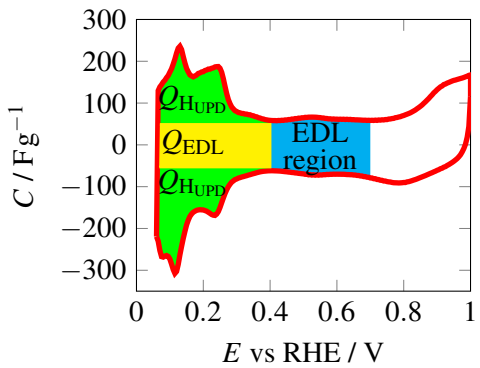

Figure 19. Capacitance vs potential curves calculated from CV data for a Pt−CeO_2/C material measured in 0.5 mol dm^{-3} H_2SO_4 solution saturated with argon.

process of quinone [124].

$$\begin{array}{c} \diagdown \\ \diagup \end{array}\!\!\text{C}=\text{O} \;+\; \text{H}_3\text{O}^+ \;+\; \text{e}^- \;\underset{\text{discharge}}{\overset{\text{charge}}{\rightleftharpoons}}\; \begin{array}{c} \diagdown \\ \diagup \end{array}\!\!\text{C}-\text{OH} \;+\; \text{H}_2\text{O}.$$

quinone type (4.83)

The adsorption and desorption of hydrogen species under deposition potential (H_{UDP}) can be observed in the potential region more negative than 0.40 V (Figure 19). The average of the H_{UDP} charges (from both anodic and cathodic scan) of a monolayer on Pt surface ($Q_{H_{UDP}}$, C) [125] can be used to estimate the electrochemcial active surface area (ECSA) value.

$$Q_{\text{H}_{\text{UDP}}} = 0.5 \times (Q_{\text{total}} - Q_{\text{EDL}}), \tag{4.84}$$

where Q_{total} (C) is the total charge in the region 0.05 to 0.40 V and Q_{EDL} (C) is the sum of the charge accumulated at the electrical double layer (EDL) in the same potential region. At mentioned conditions, the ECSA value can be determined following the equation [126, 127] below.

$$\text{ECSA}(\text{m}^2_{\text{Pt}}\,\text{g}^{-1}_{\text{Pt}}) = \frac{Q_{\text{H}_{\text{UDP}}}}{m_{\text{Pt}} \cdot Q_{\text{H}_{\text{UDP, ref}}}}, \tag{4.85}$$

where the $Q_{\text{H}_{\text{UDP, ref}}}$ is a reference value (2.10 $\text{C}\,\text{m}^{-2}$) for the $Q_{\text{H}_{\text{UDP}}}$ process on a smooth polycrystalline Pt surface [128]. The diameter, $d_{\text{Pt, ECSA}}$, of the spherical Pt NPs can be estimated using the ECSA value [129].

$$d_{\text{Pt, ECSA}}(\text{nm}) = \frac{6}{\rho_{\text{Pt}} \cdot \text{ECSA} \cdot 10^9}, \tag{4.86}$$

where $\rho_{\text{Pt}} = 21.45 \times 10^6\ \text{g}\,\text{m}^{-3}$ is bulk density of Pt [80]. The $d_{\text{Pt, ECSA}}$ reflects the dispersion of Pt NPs on the support surface.

4.3.4 Rotating Disk Electrode Method

The rotating disk electrode (RDE) method is the most popular approach to conduct a hydrodynamic voltammetry experiments. The same setup from the CV with a rotator attached to the WE can be used for the RDE measurement (Figure 17). In this study, the RDE method is used to study the ORR. As the products are simutaneously swept from the electrode surface, the RDE can achieve the stationary measurement conditions, and control mass transport conditions. The mass transport in this method is governed by the convection caused by the rotating electrode and the diffusion of regents from the bulk solution to the electrode surface [122]. When the electrode rotates, the solution under the electrode forms two different profiles; i.e. the stagnant Nernst diffusion

layer near the electrode surface and the convection region in the bulk solution. The diffusion layer thickness, δ, is inversely proportional to the rotation speed of the WE [130].

$$\delta = 1.61 \cdot {D_{O_2}}^{1/3} \upsilon^{1/6} \omega^{-1/2}, \tag{4.87}$$

where D_{O_2} is the diffusion coefficient of oxygen in the bulk solution, υ is the kinematic viscosity of the bulk solution, and ω is the angular rotation speed of the WE. If the electrode reaction kinetics is limited by the mass tranfer process, the diffusion step limits the charge transfer and the current is described by Levich equation [130].

$$I_d = -0.62 \cdot nF {D_{O_2}}^{2/3} \upsilon^{-1/6} c_{O_2} \omega^{1/2}, \tag{4.88}$$

where F is Faraday constant, n is the number of electrons transferred per one O_2 molecule, and c_{O_2} is the concentration of oxygen in the bulk solution. According to the Equation 4.88, the limiting current is proportional to c_{O_2}. The n value can be calculated from the RDE data using the Equation 4.88 in the diffusion limited conditions.

The ORR process is usually limited by the charge transfer and mass transfer process rates. Therefore, the classical Koutechký-Levich (K-L) equation can be applied to separate the components.

$$\frac{1}{I_c} = \frac{1}{I_k} + \frac{1}{I_d}, \tag{4.89}$$

where I_c is the measured ORR current corrected with the background current, I_k is the kinetic current of the heterogeneous process. The $I_k = -nFk_{het}c_{O_2}$ can be substituted into the Equation 4.89, and we can have the Equation 4.90.

$$\frac{1}{I_c} = \frac{1}{-nFk_{het}c_{O_2}} + \frac{1}{-0.62 \cdot nF {D_{O_2}}^{2/3} \upsilon^{-1/6} c_{O2} \omega^{1/2}}. \tag{4.90}$$

Since the 0.1 mol dm^{-3} $HClO_4$ solution saturated with oxygen is used for the ORR at 25°C in this study, the $c_{O_2} = 1.26$ mol m^3 [131], $D_{O_2} = 1.90 \times 10^{-5}$ cm^2 s^{-1} [131], and $\upsilon = 0.0089$ (cm^2 s^{-1}) [132] were used for the calculations.

4.3.5 Kinetics Assessment

In the RDE method, the mass transfer is not the limiting process at very low current region ($I < I_d$) if the solution is stirred well [123, 130]. Therefore, the current in that low current region directly reflects the charge transfer the process. For the Pt-based catalysts, the ORR is usually limited by the charge transfer at potentials more positive than 0.90 V. The MA and specific activity (SA) at 0.90 V are used widely to compare the ORR kinetics of studied materials [130].

$$MA_{0.9\ V} = \frac{I_{k,\ 0.9\ V}}{m_{Pt}}, \tag{4.91}$$

$$\mathrm{SA} = \frac{\mathrm{MA}_{0.9\ \mathrm{V}}}{\mathrm{ECSA}}, \tag{4.92}$$

where $I_{\mathrm{k},\ 0.9\ \mathrm{V}}$ is the kinetic current for the ORR at 0.9 V.

The most popular method to assess the kinetics of a charge transfer limited reaction is to construct the Tafel plot (Equation 4.93).

$$\eta = a + b \cdot log(I_{\mathrm{k}}), \tag{4.93}$$

where $\eta = E - E_{\mathrm{eq}}$ is the overpotential and E_{eq} is equilibrium potential of the reaction under study (at $I = 0$). The Tafel relationship can be established only when the kinetics of the reaction is sluggish, and the reaction requires a large activation energy [130]. According to Marcus-Hush model for the reaction kinetics, the curvation of the Tafel plot can be caused by the variation of transfer cofficient with electrode potential [123]. However, nearly linear Tafel plots can be established.

In the case of ORR, the Tafel slope for polycrystalline Pt catalyst is around 60 mV in low current region (from 0.9 to 1.0 V) [133, 134]. However, the Tafel slope for polycrystalline Pt catalyst is shifted to 120 mV in high current region (from 0.75 to 0.85 V) due to the change of the ORR mechanism and the decrease of adsorbed oxides at the catalyst surface [133, 134].

4.3.6 Stability Assessment

The accelerated stability test (AST) is a common method for investigate the stability of material in the interested potential range under study using CV. The change of electrochemical activity after high number of voltammetry cycles can reflect the stability of catalyst material under the certain conditions such as oxidation and reduction of the reactants at/on the catalyst surface. This approach is usually used for the analyses of the stability of MOR [135–138] and ORR catalysts [32].

The chronoamperometry (CA) is usually conducted to investigate the stability at a constant potential value during short time period. This method reveals the changes of electrochemical activity when a constant potential is applied over the measurement duration. The short time stability of the catalyst for MOR is investigated at various potentials using the CA method [136–138].

5. EXPERIMENTAL

5.1 Synthesis of Materials

5.1.1 Synthesis of Chromium Carbide-Derived Carbons

Four different chromium CDCs were synthesised using the precursor Cr_3C_2 (99.5% purity, –325 mesh powder, the product of Sigma-Aldrich) for this study. The synthesis temperatures used were fixed at 800, 900, 1000, and 1100 °C and the corresponding materials are C(Cr_3C_2, 800), C(Cr_3C_2, 900), C(Cr_3C_2, 1000), and C(Cr_3C_2, 1100). The synthesis step used in this work was slightly different from the same C(Cr_3C_2) materials used in our previous study [39]. The cleaning step, in which the stream of H_2 and Ar (1:4) gas at 800 °C was used, was conducted 30 min longer than that in the previous study. Therefore, there are some differences in the characteristics of materials synthesised between the two studies. The general reaction for this synthesis is given as an Equation 4.4 and the details of the synthesis procedure can be found in the study by Thomberg *et al.* [39].

5.1.2 Synthesis of CeO_2

The CeO_2 NPs were synthesised using the $Ce(NO_3)_3 \times 6\,H_2O$ salt (Stream Chemicals, 99.9% - Ce). Two strategies were applied to synthesize CeO_2/C complex materials. The first method is a modified solvothermal synthesis method using L-histidine (Sigma-Aldrich, ReagentPlus®, $\geq$ 99%) and urea (Sigma-Aldrich, puriss., meets analytical specification of Ph. Eur., 99–101.0%) to control the crystal shape of CeO_2 NPs. The second method was the sonochemical deposition method using the EG (Lach-Ner, 99.98%) as a capping reagent. The details of this synthesis method are described in our previous work [139, 140], and the parameters are given in the Table 5, in which the subscript text such as "solvo", "ultr", and "MW" was used to denote for solvothermal, ultrasound, and microwave methods. The alkaline solution was prepared from NaOH (Sigma-Aldrich, 99.99% metals basis, Semiconductor grade) and Milli-Q water (18 MΩ cm). Details of the synthesis procedure for the CeO_2/C_{ultr} and Ce_{ultr} materials were followed from the work of Zhang *et al.* [141]. According to Zhang et al., the process can be described as:

$$4\,Ce^{3+} + 12\,OH^- + O_{2(air)} + 6\,H_2O \xrightarrow{\text{ultrasound}} 4\,CeO_2 \cdot 12\,H_2O, \qquad (5.1)$$

$$CeO_2 \cdot n\,H_2O \xrightarrow{T} CeO_2 + n\,H_2O. \qquad (5.2)$$

The difference between the CeO_2/C_{ultr} and Ce_{ultr} materials is that the carbon material was mixed together with the reaction mixture at the beginning of the synthesis in the case of CeO_2/C_{ultr} material. After the synthesis, this material had to be washed with Milli-Q water, filtered and dried before the CeO_2/C_{ultr} material

was finally obtained. The Ce_{ultr} was the colloidal solution, which is illustrated in the Figure 20.

The colloidal CeO_2 solution was synthesized using either ultrasound sonication (Ce_{ultr}) [140] or microwave method (Ce_{MW}) [140] with appropriate NaOH concentration in EG solution. Cerium(III) nitrate was mixed with EG and added to the reaction mixture. A calculated volume of $10\,mol\,dm^{-3}$ NaOH solution in Milli-Q water was diluted in EG to reach $10\,cm^3$. This NaOH solution was then added slowly into the reaction mixture to obtain the final concentration shown in the Table 5. Due to the use of a concentrated NaOH solution, the volume percentage of water remained small and constant. The total volume for the synthesis mixture was $46.5\,cm^3$. The reaction mixture was then treated with either microwave or ultrasound. The parameters used are given in Table 5. For the microwave treatment, the mixture was radiated for 78 s three times, with 30-minute intervals between each radiation to allow the solution to cool down to room temperature. The obtained solution was thoroughly mixed by hand and used to prepare $Pt-CeO_2/C$ catalysts.

Table 5. Synthesis parameters of CeO_2 particles onto the Ketjenblack carbon and CeO_2 from colloidal solution.

Material	$c_{Ce^{3+}}$ / $mmol\,dm^{-3}$	c_{NaOH} / $mol\,dm^{-3}$	$t_{ultrasound}$ / h	t_{MW} / s	$t_{solvothermal}$ / h	$T_{reaction}$ / °C
CeO_2/C_{solvo}-1[a]	30	–[c]	–	–	12	≈130
CeO_2/C_{solvo}-2[b]	30	–[c]	–	–	12	≈130
CeO_2/C_{ultr}-1	5	0.125	2	–	–	≤60
CeO_2/C_{ultr}-2	2.5	0.032	2	–	–	≤60
CeO_2/C_{ultr}-3	2.5	1	2	–	–	≤60
Ce_{ultr}[d]	2	0.1	2	–	–	≤60
Ce_{MW}-1[d]	2.5	0.1	–	234	–	≤198
Ce_{MW}-2[d]	5	0.1	–	234	–	≤198

[a] CeO_2/C particles were calcinated at 550 °C for 5 h under a N_2 gas stream after the synthesis. The mass ratio of $Ce(NO_3)_3 \cdot 6\,H_2O$ and carbon was 0.40
[b] CeO_2/C particles were calcinated at 550 °C for 5 h under a N_2 gas stream after the synthesis. The mass ratio of $Ce(NO_3)_3 \cdot 6\,H_2O$ and carbon was 0.58
[c] Urea and L-histidine were used.
[d] CeO_2 particles in the colloidal solution.

5.1.3 Pt-CeO_2/C Catalysts Preparation

There were two strategies to synthesize the $Pt-CeO_2/C$ catalyst materials. In the first method, called the two-step method, the Pt NPs were deposited onto the CeO_2/C support. In this case, if the combination of heating methods (ultrasound,

microwave and refluxing methods) was used for the precipitation, the synthesis was performed as an one-pot synthesis, where all the precursors (H_2PtCl_6 and CeO_2/C) and chemicals were mixed in the EG solution at the beginning of the synthesis. However, if Pt was deposited onto the CeO_2/C support material by adjusting the pH of the solution, the Pt colloid was synthesised firstly using the refluxing method (Figure 21). After that, the colloidal solution of Pt was mixed with a solution of CeO_2/C dispersed in a mixture (0.83:0.17, volume ratio) of EG and Milli-Q water. The pH of this mixture was adjusted to 5 for the precipitation of Pt onto CeO_2/C material. The synthesis parameters were described in the Tables 6 and 7.

The second method is co-precipitation of Pt and CeO_2 NPs onto a carbon support. In this case, a solution of carbon support material in EG solution was mixed with the colloidal solutions of Pt (Figure 21) and CeO_2 (Figure 20). Pt and CeO_2 were then precipitated onto the support material either by adjusting the pH of the solution with the acid solution or by adding 1 cm^3 of H_2O_2 (Fisher Chemical, 30%). The synthesis parameters are described in Tables 6 and 7. The procedures for the synthesis methods of these complex catalysts are described in our previous studies [139, 142].

The following procedure was used for the synthesis of Pt colloid. Firstly, a stock Pt solution was prepared by dissolving 126 mg of $H_2PtCl_6 \cdot 6\,H_2O$ in 1 cm^3 of Milli-Q water. 200 cm^3 of EG was transferred into a 500 cm^3 synthesis flask. A 10 $mol\,dm^{-3}$ NaOH was prepared by dissolving the required amount of NaOH in Milli-Q water. Then, 0.743 cm^3 of 10 $mol\,dm^{-3}$ NaOH was transferred into the synthesised flask. 0.846 cm^3 of the stock Pt solution and 10 cm^3 Milli-Q water were transferred into a small beaker . The synthesised flask was set up with refluxing system and oil bath. The reaction solution was mixed well using the hot plate with a magnetic stirrer. Argon gas (Linde Gas, 99.9999%) was bubbled through the reaction solution. After bubbling with argon gas for 15 min, the

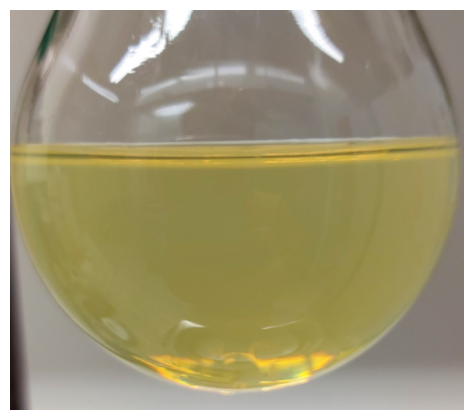

Figure 20. The colloidal solution of the CeO_2 nanoparticles after the CeO_2 synthesis was finished.

diluted Pt solution was pumped slowly into the reaction mixture by using a syringe pump. The syringe was rinsed three times using 22.4 cm^3 of Milli-Q water. The reaction mixture contained 200 cm^3 of EG and 34 cm^3 of water in total. The final concentration of the chemicals is given in the Table 7. The reaction mixture was heated up to 100 °C and was kept at this temperature for 2 hours. The dark brown solution formed was the Pt colloidal solution containing 40 mg of Pt.

A procedure to synthesize a complete Pt−CeO_2/C catalysts is described as the following. Depending on the calculated amount of CeO_2 colloid in the previous step, carbon amount around 120–160 mg was weighed to synthesise corresponding 20 wt% Pt−CeO_2/C and Pt/C catalysts, e.g. 160 mg of carbon was used to synthesise 20 wt% Pt/C catalysts. From now and on, the Pt−CeO_2/C is

Table 6. Substrates and chemicals for the synthesis of Pt−CeO_2/C and Pt catalysts.

Material	Substrate & colloidal solution	Chemicals used to deposit Pt NPs	Chemicals used to synthesise glycolate anions	Deposition method
$PtCe_{NaOH}$	CeO_2/C_{solvo}-1	–	NaOH	two-step
$PtCe_{Na}$-1	CeO_2/C_{solvo}-1	–	Na	two-step
$PtCe_{Na}$-2	CeO_2/C_{solvo}-1	–	Na	two-step
$PtCe_{chl}$-1	CeO_2/C_{solvo}-2[a]	HCl	NaOH	two-step
$PtCe_{chl}$-2	CeO_2/C_{ultr}-1	HCl	NaOH	two-step
$PtCe_{chl}$-3	CeO_2/C_{ultr}-1	HCl	NaOH	two-step
$PtCe_{chl}$-4	CeO_2/C_{ultr}-2	HCl	NaOH	two-step
$PtCe_{H_2O_2}$	Ce_{ultr} + C(KB)	H_2O_2	NaOH	co-precipitation
$PtCe_{H_3PO_4}$	CeO_2/C_{ultr}-3	H_3PO_4	NaOH	two-step
$PtCe_{sul}$-1	CeO_2/C_{ultr}-2	H_2SO_4	NaOH	two-step
$PtCe_{sul}$-2	Ce_{ultr} + C(KB)	H_2SO_4	NaOH	co-precipitation
$PtCe_{sul}$-3	Ce_{MW}-1 + C(KB)	H_2SO_4	NaOH	co-precipitation
$PtCe_{sul}$-4	Ce_{MW}-2 + C(KB)	H_2SO_4	NaOH	co-precipitation
$PtCe_{sul}$-5	Ce_{MW}-2 + $C(Cr_3C_2, 900)$[a]	H_2SO_4	NaOH	co-precipitation
$PtC(KB)_{com}$	C(KB)	H_2SO_4	NaOH	precipitation
PtC(KB)	C(KB)	H_2SO_4	NaOH	precipitation
$PtC(Cr_3C_2)$	$C(Cr_3C_2, 900)$[a]	H_2SO_4	NaOH	precipitation

[a]The ball-milling of the substrate was performed using ytrium stabilised zirconia balls for 45 min at 300 rpm, and after that, the substrate was dried at 100 °C and 50 mbar vacuum oven

noted as $PtCe_{(chemical/method)}$-number, to specify a specific material (given in the Table 7). Carbon was mixed well in a 50-cm^3 mixture of EG and Milli-Q water before the ultrasound sonication for 10 minutes. After that, the carbon suspension and CeO_2 colloid mixture were transferred into the Pt colloid solution. In the case of $PtCe_{sul}$-1, the 160 mg of CeO_2/C mixture was transferred into the Pt colloid solution. The reaction mixture was stirred well using a magnetic stirrer during the NPs deposition. A solution of 0.5 $mol\,dm^{-3}$ H_2SO_4 was added drop-wise until pH 5. The precipitation of Pt NPs onto the carbon support by the pH control of the solution has been used by various research groups [71, 143]. Thereafter, the reaction mixture was left to sediment for 30 min. The final step was to filter and dry the solid product received overnight in a vacuum oven at 100 °C and 50 mbar reduced pressure.

The synthesis of PtC catalysts were conducted by the precipitation of Pt NPs onto a corresponding carbon support. The Pt precipitation was conducted either using a combination of heating methods or by adjusting the pH of the solution. The synthesis parameters can be found in Tables 6 and 7.

For selected materials (Table 8), the heat treatment under a stream of hydrogen gas was performed. The post-treatment parameters are described in the Table 8. The treatment temperature and duration of the $PtCe_{chl}$-2_H_2 and $PtCe_{H_3PO_4}$_H_2 catalysts were reduced to avoid the changes of Pt diameter after the treatment.

a) Original reaction solution

b) Temperature reached the synthesis temperature (90°C)

c) The synthesis was conducted for 8 min

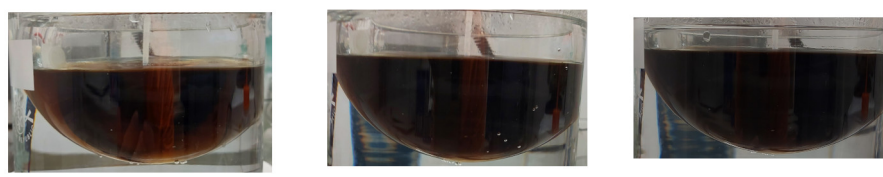

d) The synthesis was conducted for 30 min

e) The synthesis was conducted for 50 min

f) The synthesis was conducted for 90 min

Figure 21. The changes of reaction mixture colour during the synthesis of Pt nanoparticles.

Table 7. The synthesis parameters for Pt and Pt−CeO_2/C materials using the ethylene glycol reduction method.

Material	$c_{Pt(IV)}$ / mmol dm^{-3}	c_{Na^+} / mmol dm^{-3}	Na^+/Pt	$t_{ultrasound}$ / min	t_{MW} / s	$t_{refluxing}$ / h	$T_{refluxing}$ / °C
$PtCe_{NaOH}$	5.0	50	10	60	78[a]	2	110
$PtCe_{Na}$-1	6.0	30	5	60	66[a]	2	110
$PtCe_{Na}$-2	6.0	30	5	90	68[a]	–	–
$PtCe_{chl}$-1	5.7	58	10	–	–	2	110
$PtCe_{chl}$-2	2.0	20	10	–	–	2	110
$PtCe_{chl}$-3	0.9	18	20	–	–	6	110
$PtCe_{chl}$-4	0.9	62	70	–	–	2	110
$PtCe_{H_2O_2}$	13.3	133	10	–	180[b]	–	–
$PtCe_{H_3PO_4}$	2.0	64	32	–	–	2	100
$PtCe_{sul}$-1	0.9	30	34	–	–	2	100
$PtCe_{sul}$-2	1.5	80	53	–	–	2	100
$PtCe_{sul}$-3	0.9	30	34	–	–	2	100
$PtCe_{sul}$-4	0.9	30	34	–	–	2	100
$PtCe_{sul}$-5[c]	0.9	30	34	–	–	2	100
$PtC(KB)_{com}$	6.1	31	5	90	78[a]	–	–
PtC(KB)	0.9	30	34	–	–	2	100
$PtC(Cr_3C_2)$	0.9	30	34	–	–	2	100

[a]A 700W microwave oven (Galanz WD700L17-8, frequency ≈ 2.4 GHz) was set at the medium-low level.
[b]A specialized microwave device (Anton Paar Multiwave PRO microwave with an 8N rotor, frequency ≈ 2.4 GHz) pre-heated the sample to 160 °C and the sample has been hold at this temperature for 180 s by using a 100W microwave radiation.
[c]A $C(Cr_3C_2)$ support was used instead of C(KB) support.

Table 8. The post-treatment parameters for the Pt−CeO_2/C catalysts. The post-treatment was in the stream of 400 cm^3 min^{-1} H_2 gas.

Material	Starting material	$t_{reaction}$ / h	$T_{reaction}$ / °C
$PtCe_{chl}$-1_H_2	$PtCe_{chl}$-1	4	300
$PtCe_{chl}$-2_H_2	$PtCe_{chl}$-2	2	200
$PtCe_{H_3PO_4}$_H_2	$PtCe_{H_3PO_4}$	2	200

5.2 Physical and Electrochemical Characterisation of Catalysts

5.2.1 Physical Characterisation Methods

The thermogravimetric analysis (TGA) was conducted using an Al_2O_3 pan and the NETZSCH STA449F3 instrument. The temperature program increased the temperature at the rate $10°C\,min^{-1}$ from 25 °C to 1000 °C under the flow of 40 $cm^3\,min^{-1}$ N_2 gas (Linde Gas, 99.999%) and 10 $cm^3\,min^{-1}$ O_2 gas (Linde Gas, 99.999%).

A Bruker D8 Advance diffractometer coupled with Ni-filtered CuK_α radiation emitted a 0.6 mm wide parallel beam through a 2.5° Soller slit. The scattered light passed through another 2.5° Soller slit and was collected at the LynxEye line detector system. All signals for 2θ angle in the range from 20 ° to 90 ° with the scanning step of 0.013° were collected for the X-ray diffractogram. The total duration per scanning step was 348 seconds. The double Voigt model [144] was employed for fitting of the XRD profile and the Topas software (version 6) was used for the crystallite size estimation.

Raman spectroscopy measurements were conducted using an argon lazer ($\lambda = 514$ nm) coupled with a Renishaw InVia micro-Raman spectrometer. Twenty spots were measured to collect the excitation spectra for each material. The laser power was 2 mW and the collection time was 15 min for each spot. The average spectra are shown in the results.

The samples for low-temperature (at near 77 K) nitrogen sorption [145] were degassed at 100 °C and 13 µbar for 24 h. The measurements were conducted using a 3Flex system (Micromeritics, USA). The pore-size distribution (PSD) and micro-mesoporosity data were estimated using the SAIEUS software [106] (version 2.02, Micromeritics, USA) and built-in function "Carbon-N2-77, 2D-NLDFT Heterogeneous Surface" based on the nonlocal density functional theory model for nitrogen sorption at porous carbon [107]. The other parameters such as the specific surface area (S_{DFT}), the surface area of mesopores ($S_{\mathrm{mesopores}}$) and the total pore volume (V_{total}) and volume of mesopores ($V_{\mathrm{mesopores}}$) were estimated from the "Carbon-N2-77, 2D-NLDFT Heterogeneous Surface" modeling results with the relative pressure $\frac{P}{P_0}$ from 1×10^{-5} to 0.95 [106, 107].

The Zeiss Merlin microscope and a copper sample holder were used for conducting the high-resolution scanning electron microscopy (SEM). The energy dispersive X-ray (EDX) system on the Zeiss Merlin instrument and a Burker EDX-XFlash® 6/30 detector were employed at the accelerating voltage of 15 kV for the quantitative analysis. The quantitative data were processed using the P/B-ZAF standardless analysis.

A JEOL JEM-2100 device (JEOL GmbH, Eching, Germany), which worked at an acceleration voltage of 200 kV, has been used to record the transmission electron microscopy (TEM) images.

The microwave plasma atomic emission spectrometry (MP-AES) was conducted to analyse the Pt and CeO_2 content in the studied materials. From 10

to 20 mg of samples were dissolved by sequentially adding 6 cm^3 of 35% HCl (Carl Roth ROTIPURAN Supra) and 2 cm^3 69% HNO_3 (Carl Roth ROTIPURAN Supra) into NXF100 digestion vessels (PTFE-TFM liner). After that, the digestion vessels were capped and heated for digestion using an Anton Paar Multiwave PRO microwave digestion system coupled with an 8N rotor. The digested samples were diluted using 1%HNO_3/1%HCl solution to a final dilution factor of 80000 for the determination of CeO_2 and Pt contents. An Agilent 4210 MP-AES was calibrated using single-element Ce and Pt solutions before measuring Ce at 417.659 nm wavelength and Pt at 265.945 nm wavelength. The CeO_2 and Pt content were calculated back from the measured data of Ce and Pt in diluted samples.

5.2.2 Electrochemical Measurements

Electrochemical characterization to study MOR and ORR was conducted using a three-electrode system in a proper electrolyte solution (Figure 17). The reference electrode was a reversible hydrogen electrode (RHE), which was prepared in the corresponding electrolyte solution [146]. The RHE was connected to the cell via a Luggin capillary. All the potentials in this work are referenced against RHE. The auxiliary electrode was a Pt net. The working electrode was the glassy carbon disk electrode (GCDE) covered with the catalyst layer.

For all experiments, the working electrode was prepared by pipetting a 7-µL drop of catalyst suspension onto the GCDE (PINE Instrument Company, electrode diameter 5 mm) surface. The nominal loading of Pt on the GCDE surface was 18 $\mu g_{Pt}\,cm^{-2}$. The suspension was prepared by sonication of 4.9 mg of catalyst in a mixture of 1.33 cm^3 Milli-Q water, 0.57 cm^3 isopropanol (Sigma-Aldrich, $>$ 99%) and 41 µL of Nafion solution (5% solution, Sigma-Aldrich). The ionomer-to-carbon ratio was 0.5.

All electrochemical measurements were conducted using the Autolab PGSTAT302N potentiostat and NOVA 1.11.2 software. Before electrochemical measurements, the conditioning step was performed by scanning the working electrode potential from 0.025 V to 1.4 V at 0.5 $V\,s^{-1}$ and at 1600 rpm for 100 cycles in the corresponding electrolyte solution in an Ar atmosphere.

The ECSA values and Pt NP diameter, $d_{Pt,\,ECSA}$, were estimated in 0.5 $mol\,dm^{-3}$ H_2SO_4 (conc. 95–97%, Sigma-Aldrich, puriss. p.a, ACS reagent) or 0.1 $mol\,dm^{-3}$ $HClO_4$ solution saturated with Ar. The potential was scanned from 0.06 V to 1.00 V at various potential scanning rates from 0.01 to 0.40 $V\,s^{-1}$. The ECSA and $d_{Pt,\,ECSA}$ were determined using the model discussed in detail by Trasatti *et al.* [127].

The MOR activity was measured in the solution of 0.5 $mol\,dm^{-3}$ H_2SO_4 + 1 $mol\,dm^{-3}$ CH_3OH saturated with Ar. During the cyclic voltammetry measurements (CV), the potential was scanned from 0.06 V to 1.26 V at 0.05 $V\,s^{-1}$. The CA experiments were performed at fixed potentials of 0.85 V for

60 min and 0.50 V for 30 min, respectively.

The ORR activity was measured in 0.1 $\mathrm{mol\,dm^{-3}}$ $HClO_4$, which was prepared from 70% $HClO_4$ (99.999% trace metals basis, redistilled, Sigma-Aldrich) and Milli-Q water. The RDE measurements were conducted from 0.01 to 1.00 V at 0.02 $\mathrm{V\,s^{-1}}$ and 1600 rpm. The background current, which was established for the electrolyte was saturated with Ar gas. After that, the currents were collected in the electrolyte saturated with O_2. To get the ORR currents, the currents were corrected with the background currents. During the measurements, the potential was corrected with the ohmic drop potential. The electrolyte resistance was estimated from EIS measurements.

The CO stripping measurements were conducted in 0.1 $\mathrm{mol\,dm^{-3}}$ $HClO_4$ solution after the conditioning step. The solution was bubbled with argon gas for 10 min while the working electrode potential was kept at 0.05 volt (400 rpm). After that, the gas flow was switched to CO gas for 10 min. Finally, the argon gas was introduced again for another 10 min before the CO oxidation. Five CV cycles were measured within the range from 0.05 to 1.00 V at the scan rate of 20 $\mathrm{mV\,s^{-1}}$ (0 rpm) and the argon gas was flowing above the solution [147]. The last CV cycle was used as the baseline to correct the background charges during the calculation of ECSA from CO oxidation peaks, $ECSA_{CO}$. The $ECSA_{CO}$ was estimated in the potential range from 0.4 to 1.0 V using the reference charge of 420 $\mu\mathrm{C\,cm^{-2}_{Pt}}$ for Pt-based catalyst [148].

In the case of CDC materials, the CV measurements for the ORR were conducted in the potential range from -0.4 to 1.1 V, and the potential scan rates used were from 5 to 1000 $\mathrm{mV\,s^{-1}}$. The RDE measurements (for the ORR) were measured at 10 $\mathrm{mV\,s^{-1}}$, and the electrode rotation speed was varied from 0 to 3000 $\mathrm{rev\,min^{-1}}$. Besides, the EIS measurements were conducted at 0.8 V in 0.1 $\mathrm{mol\,dm^{-3}}$ $HClO_4$ solution saturated with argon. The EIS data were collected within a frequency, f, region from 0.1 to 10 000 Hz with $\Delta E = 10\ \mathrm{mV_{rms}}$.

The Pt dissolution experiments were performed using a three-electrode system in 6 $\mathrm{mol\,dm^{-3}}$ HCl aqueous solution, which was prepared from concentrated HCl (Sigma-Aldrich, 36.5-38%, Analytical specification Pr. Eur.). The reference electrode was the Ag|AgCl saturated KCl electrode (Ag|AgCl), the auxiliary electrode was the carbon fibre electrode, and the working electrode was the GCDE covered by the catalyst layer. The potentials for dissolution experiments are reported against the Ag|AgCl electrode. Six cyclic voltammograms were measured from 0.45 to 0.95 V vs Ag|AgCl at the potential scan rate of 0.5 $\mathrm{mV\,s^{-1}}$ to collect the Pt dissolution data [73]. The background data were collected using the same electrode after the dissolution was conducted. The apparent Pt dissolution charge values used were corrected with background charge (for Pt free system) to estimate the Pt content. The dissolution of Pt follows the reaction Equation 5.3 and the results were reported as the

concentration of Pt on the electrode surface, c_{Pt} [149]:

$$\mathrm{Pt} + 6\,\mathrm{Cl}^- \longrightarrow [\mathrm{PtCl_6}]^{2-} + 4\,\mathrm{e}^-, \tag{5.3}$$

$$c_{\mathrm{Pt}}(\mu \mathrm{g_{Pt}\,cm^{-2}}) = \frac{Q_{\mathrm{corr.}} \times M_{\mathrm{Pt}} \times 10^6}{nFA_{\mathrm{electrode}}}. \tag{5.4}$$

Where $Q_{\mathrm{corr.}}$ (C), is the charge corresponding to Pt dissolution, F is Faraday constant (96485 $\mathrm{C\,mol^{-1}}$), n is number of electrons transferred (4 $\mathrm{e^-}$), M_{Pt} is atomic mass of Pt (195 $\mathrm{g\,mol^{-1}}$), and $A_{\mathrm{electrode}}$ is electrode surface area (0.196 $\mathrm{cm^2}$).

6. RESULTS AND DISCUSSIONS

6.1 Structure of Catalysts

6.1.1 Chemical Composition, Structure, and Morphology of C(Cr_3C_2) Materials

From the TGA results for C(Cr_3C_2) materials (Figure 22a), the two step oxidation in the temperature range from 400 °C to 650 °C is visible. The first step of oxidation process takes place at 470 °C and is the oxidation of amorphous carbon. The second oxidation process observed at approximately 530 °C caused by the oxidation of the more graphitized carbon structure [150]. The moisture content of studied C(Cr_3C_2) is less than 0.3 wt%. Solid residual of 6.6 wt% is retained in the case of C(Cr_3C_2, 800) material after the TGA experiment. The residual compounds confirmed by energy dispersive X-Ray spectroscopy (EDX) results (Figure 23) were quartz and chromium compounds. These residual compounds are insignificant in the case of other C(Cr_3C_2) based materials because the chlorination reaction (Equation 4.4) for other C(Cr_3C_2) was faster and more completed at higher temperature applied for the synthesis.

From the XRD results (Figure 22b), diffraction peaks at 2θ angles of 26°, 43°, 54° and 78° correspond to *hkl* planes of C(002), C(100/101), C(004), and C(110), respectively. There are no diffraction peaks corresponding to the Cr_3C_2 precursor in the diffractograms [151, 152]. However, the C(Cr_3C_2, 800) has a diffraction peak at 2θ angle of 22°, which can be a residual of CrO(OH) and/or chromium(III) oxide. The increase of diffraction peaks sharpness of C(002) plane along with the increase of the chlorination temperature indicates the higher degree of carbon graphitisation level of carbons synthesised at higher temperatures.

The graphitisation level and the degree of order of C(Cr_3C_2) materials were investigated using Raman spectroscopy and the results are presented in Figure 22c and Table 9. The graphitisation stage of C(Cr_3C_2) materials increases with the chlorination temperature. According to the classification proposed in the study of Schuepfer *et al.* [113], the C(Cr_3C_2, 800) is in stage II nanoparticular carbon material. The C(Cr_3C_2, 900) is between the stage II (nanocrystalline graphite) and III (non-graphitic carbon material). The C(Cr_3C_2, 1000) and C(Cr_3C_2, 1100) materials can be classified into the stage III. The intensity ratio of D- and G- bands, $\frac{I_D}{I_G}$, indicates the degree of ordered carbon and disordered carbon [111]. Therefore, the C(Cr_3C_2, 800) is the most disordered carbon material and the C(Cr_3C_2) materials become more ordered when the chlorination temperature increases. This agrees well with the trend of full width at half maximum (FWHM) values for the D-band, $FWHM_D$. The C(Cr_3C_2, 1000) and C(Cr_3C_2, 1100) materials are moderately graphitised carbons, and are not highly oriented pyrolytic graphites because the FWHM values for G-band, $FWHM_G$, were greater than theorectical value (15 cm^{-1}) of highly oriented pyrolytic

graphite [111, 153].

The porosity of carbon materials influenced dramatically on the electrochemical activity of the Pt catalyst materials [28, 30]. Therefore, the understanding about the porosity of $C(Cr_3C_2)$ materials was investigated using the LTNS method. The results of LTNS for $C(Cr_3C_2)$ materials are compiled in Table 10 and Figure 22d. The $C(Cr_3C_2)$ has two regions in the pore-width distribution (PWD), given in the Figure 22d. The first PWD region is around 1 nm and the second PWD is a broad region from 2 nm to 30 nm. The total pore volume, V_{total}, and the specific surface area, S_{DFT}, of the $C(Cr_3C_2, 800)$ material are dramatically higher than that of other $C(Cr_3C_2)$ materials. Besides, the $V_{mesopores}/V_{total}$ of the $C(Cr_3C_2, 800)$ is small (0.36) compared to that of the other $C(Cr_3C_2)$ materials (> 0.85), which were chlorinated at higher temperature. Although the carbon graphitization stages and ordering degree of $C(Cr_3C_2, 900)$, $C(Cr_3C_2, 1000)$, $C(Cr_3C_2, 1100)$ are different, the porosity of these materials is

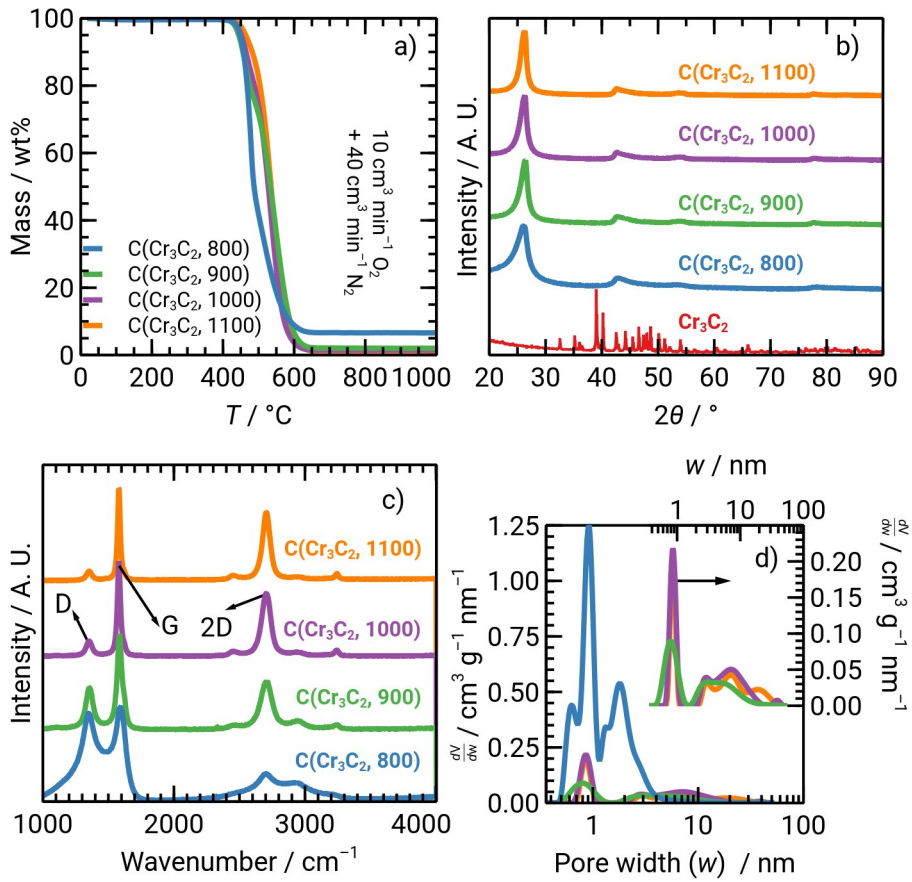

Figure 22. The physical characterization results for studied $C(Cr_3C_2)$ materials, noted in the figure.

nearly similar (Table 10). Overall, the S_{DFT} and V_{total} for these three materials are small, and the $V_{mesopores}/V_{total}$ ratio moderately increases moderately with increasing chlorination temperature.

The morphology of C(Cr_3C_2) materials is shown in Figure 23. The C(Cr_3C_2) carbon materials have the particles with irregular shape, and the particle width is from 1 to 10 µm. There are no visible differences in the morphology of C(Cr_3C_2) materials. As the chlorination temperature increased, the percentage of carbon increased and the amount of residual elements decreased according to the EDX measurement results.

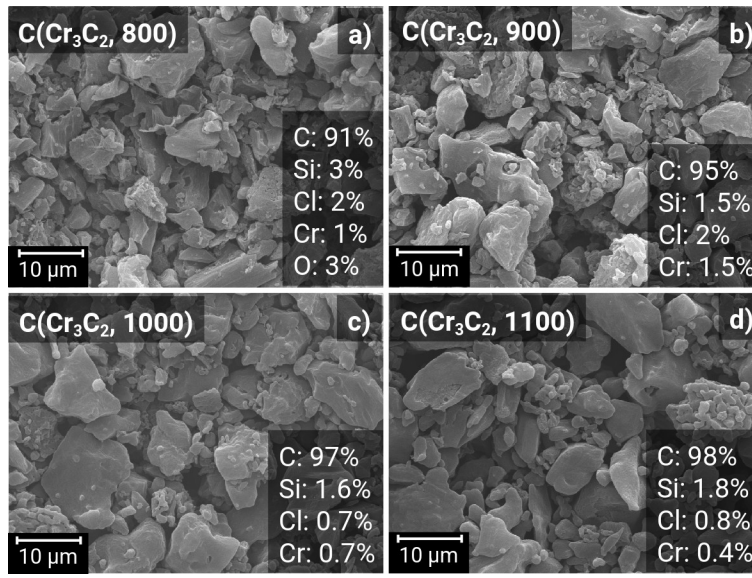

Figure 23. The scanning electron microscopic images and elemental analysis of C(Cr_3C_2) materials.

Table 9. Parameters derived from the Raman spectra of the C(Cr_3C_2) materials.

Material	$\frac{I_D}{I_G}$	$FWHM_D$ / cm^{-1}	$FWHM_G$ / cm^{-1}	$\frac{S_{\Sigma D}}{S_{\Sigma G}}$	$\frac{S_{\Sigma D}}{S_{\Sigma G+D'}}$
C(Cr_3C_2, 800)	0.93	125	59	1.90	1.51
C(Cr_3C_2, 900)	0.44	65	42	0.76	0.71
C(Cr_3C_2, 1000)	0.16	52	27	0.33	0.30
C(Cr_3C_2, 1100)	0.10	48	24	0.20	0.20

I_D, I_G are the intensity of Raman peaks
$FWHM_D$ is full width half maximum at Raman D-band peak
$FWHM_G$ is full width half maximum at Raman G-band peak
$S_{\Sigma D}$, $S_{\Sigma G}$, $S_{\Sigma G+D'}$ are relative area of Raman peaks

6.1.2 Chemical Composition, Structure, and Morphology of CeO_2/C Materials

The TGA (results are in Figure 24a) were conducted to estimate the CeO_2 content in the CeO_2/C materials (Table 11). The oxidation of CeO_2/C_{solvo} materials starts at much higher temperature compared to the CeO_2/C_{ultr} materials. The oxidation of CeO_2/C_{solvo}-1 and CeO_2/C_{solvo}-2 starts at around 550 °C and 650 °C, respectively. The increase in CeO_2 content (from 13.8 to 19.8 wt%) in this case improved the resistance of CeO_2/C_{solvo} materials against the oxygen oxidation. The oxidation of CeO_2/C_{ultr} materials is very similar and starts at roughly 350 °C although the CeO_2 content (approximately 11 wt%) in the CeO_2/C_{ultr} materials is only slightly lower than that of CeO_2/C_{solvo}-1. The oxidation at much lower temperature indicates that CeO_2 and carbon in the CeO_2/C_{ultr} materials have probably more amorphous structure than in the CeO_2/C_{solvo} materials. Since the calcination of CeO_2/C_{solvo} materials was performed at 550 °C, which enhances the graphitization process and probably the

Table 10. Low-temperature nitrogen sorption results calculated using the SAIEUS software [107] and built-in function "Carbon-N2-77, 2D-NLDFT Heterogeneous Surface" based on the nonlocal density functional theory model for nitrogen sorption at porous carbon.

Material	S_{DFT} / $m^2\,g^{-1}$	$S_{mesopores}$ / $m^2\,g^{-1}$	V_{total} / $cm^3\,g^{-1}$	$V_{mesopores}$ / $cm^3\,g^{-1}$	$V_{mesopores}/V_{total}$
$PtCe_{NaOH}$	279	116	0.41	0.33	0.80
$PtCe_{Na}$-1	328	124	0.46	0.36	0.78
$PtCe_{Na}$-2	289	122	0.45	0.36	0.80
$PtCe_{sul}$-1	458	138	0.53	0.39	0.73
$PtCe_{sul}$-2	440	142	0.53	0.39	0.74
$PtCe_{sul}$-3	516	151	0.59	0.42	0.71
$PtCe_{sul}$-4	460	128	0.52	0.36	0.70
$PtCe_{sul}$-5	103	49	0.17	0.15	0.84
$PtC(KB)_{com}$	386	134	0.51	0.39	0.76
PtC(KB)	508	149	0.59	0.42	0.71
$PtC(Cr_3C_2)$	104	47	0.17	0.15	0.85
$C(Cr_3C_2, 800)$	1632	278	1.14	0.41	0.36
$C(Cr_3C_2, 900)$	213	101	0.34	0.29	0.86
$C(Cr_3C_2, 1000)$	273	154	0.65	0.60	0.92
$C(Cr_3C_2, 1100)$	227	135	0.72	0.68	0.94
C(KB)	730	202	0.78	0.54	0.70

S_{DFT} – specific surface area from modelling data
$S_{mesopores}$ – surface area of mesopores estimated from modelling data
V_{total} – total pore volumes estimated from modelling data
$V_{mesopores}$ – volume of mesopores estimated from modelling data

CeO_2 becomes more crystalline. Besides, the sonochemical synthesis for CeO_2/C_{ultr} materials created the surface defects (discussed in subsection 4.2.4) and were not calcinated. Therefore, the huge difference in the characteristics of CeO_2 NPs obtained from two synthesis methods was predictable.

The extreme difference in material characteristics synthesised by the

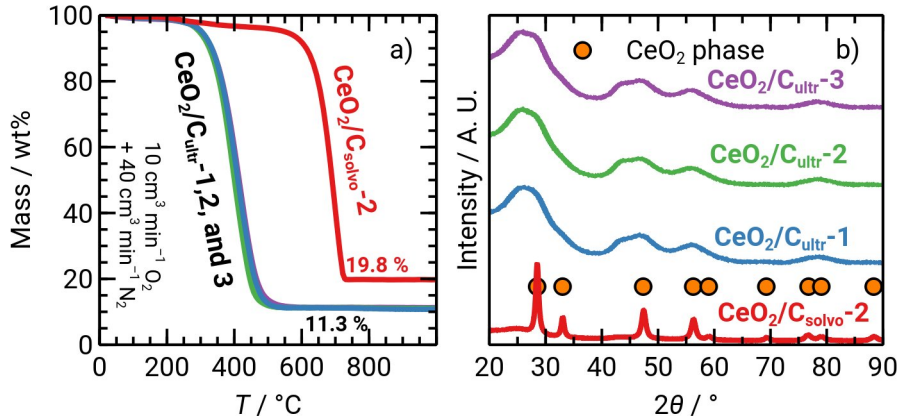

Figure 24. The thermogravimetric results (a) and X-ray diffractograms (b) for selected CeO_2/C materials, noted in the figure.

solvothermal synthesis or sonochemical synthesis methods is very well visible in the Figure 24b. The diffraction peaks of CeO_2/C_{ultr} materials are broad, and the intensity of diffraction peaks is low. The presence of CeO_2 phase in the CeO_2/C_{ultr} materials can be deduced from the difractograms, however, the diffraction peaks corresponding to CeO_2 phases rather overlap with each other and are underdeveloped. The diffraction peaks of carbon planes in the CeO_2/C_{ultr} materials overlap with the diffraction peaks of CeO_2 at 2θ angles of 26°, 43°, 54° and 78°, which corresponds to the C(002), C(100/101), C(004) and C(110) respectively. On the other hand, the diffraction peaks of CeO_2 phases developed well in the case of CeO_2/C_{solvo} materials. In this case, the diffraction peaks are narrow and sharp. The diffraction peaks at 2θ angles of 29°, 33°, 47°, 56°, 59°, 69°, 77°, 79°, and 88° correspond to the CeO_2 (111), (200), (220), (311), (222), (400), (331), (420), and (422) planes, respectively [141]. The CeO_2 crystallite size dimensions, which is noted as $d_{CeO_2,\,XRD}$ and were estimated from XRD data, of CeO_2/C_{ultr} materials were the same (around 1.2 nm), while the $d_{CeO_2,\,XRD}$ values of CeO_2/C_{solvo}-1 and CeO_2/C_{solvo}-2 materials are 9.1 and 8.5 nm, respectively (Table 11). Therefore, the slight change in reaction volume resulted in the a small difference in the $d_{CeO_2,\,XRD}$ value if concentration of $Ce(NO_3)_3 \cdot 6\,H_2O$ and carbon amount were unchanged (the ratio is given in the footnote of Table 5).

The CeO_2 NPs synthesised by the solvothermal synthesis methods are big enough (1–30 μm) to be observed using SEM method (Figure 25a,b,c). However,

Table 11. The physical characterization results of studied CeO_2/C materials.

Material	CeO_2 wt%[a]	$d_{CeO_2,\,XRD}$ / nm
CeO_2/C_{solvo}-1	13.8	9.1
CeO_2/C_{solvo}-2	19.8	8.5
CeO_2/C_{ultr}-1	10.8	1.2
CeO_2/C_{ultr}-2	11.0	1.2
CeO_2/C_{ultr}-3	11.3	1.2

[a]The absolute values calculated using changes of catalyst mass values.

the CeO_2 NPs synthesised by the sonochemical method were rather small and can be observed only using TEM (Figure 25d). In the solvothermal synthesis method, the CeO_2 particle size, which is noted as $d_{CeO_2,\,microscopy}$ and can be measured from either SEM or TEM images (Figure 25a,b), is reduced as the mass ratio of $Ce(NO_3)_3 \cdot 6\,H_2O$ and carbon increased (see the footnote of Table 5). The decrease of $d_{CeO_2,\,XRD}$ value estimated from XRD data caused by different synthesis parameters of CeO_2/C_{solvo}-1 and CeO_2/C_{solvo}-2 agrees well with CeO_2 NPs estimated from SEM and TEM. After the ball-milling treatment, the flower-shaped CeO_2 particles are broken into smaller particles (approximately 1 µm) with a distorted shape (see Figure 25c). On the other hand, the CeO_2 NPs of CeO_2/C_{ultr}-1 material are used to represent the morphology of all CeO_2/C_{ultr} materials as there is no noticeable differences amongst these materials. The CeO_2 particle size of CeO_2/C_{ultr} materials is around 3 nm, and it seems that this results from overlapping of two hexagonal CeO_2 crystallites, and the CeO_2 NPs are scattered all over the carbon pattern. In the case of CeO_2/C_{ultr} materials, the lattice fringe of CeO_2 NPs has the interplanar spacing of 0.33 nm, which corresponds to the *hkl* plane (111) [87]. Other CeO_2 planes were not found. Besides, no CeO_2 NPs were observed on $Pt{-}CeO_2$/C materials using TEM due to the low concentration of CeO_2 NPs, scattering across carbon pattern, and many crystallographic defects.

Although SEM and TEM have not been used to visualise the CeO_2 NPs deposited from Ce_{ultr} colloid solution, the $d_{CeO_2,\,XRD}$ value of $PtCe_{H_2O_2}$ and $PtCe_{sul}$-2 materials indicates the similar characteristics of the CeO_2 NPs to those of CeO_2/C_{ultr} materials (Table 12). Therefore, the morphology of CeO_2 can be the same. The use of acid solution for the co-precipitation of CeO_2 and Pt onto carbon support seems not to change the morphology of CeO_2 NPs. The co-precipitation of Ce_{MW} and Pt colloidal solution onto a support material is found to have the same morphology as in the case of CeO_2/C_{ultr} materials (see the Figure 26). The $Pt{-}CeO_2$ clusters on the $C(Cr_3C_2, 900)$ are larger than the $Pt{-}CeO_2$ cluster on C(KB). The interplanar spacing of the CeO_2 synthesised by the microwave method is 0.33 nm, which also corresponds to the CeO_2 (111) plane [87].

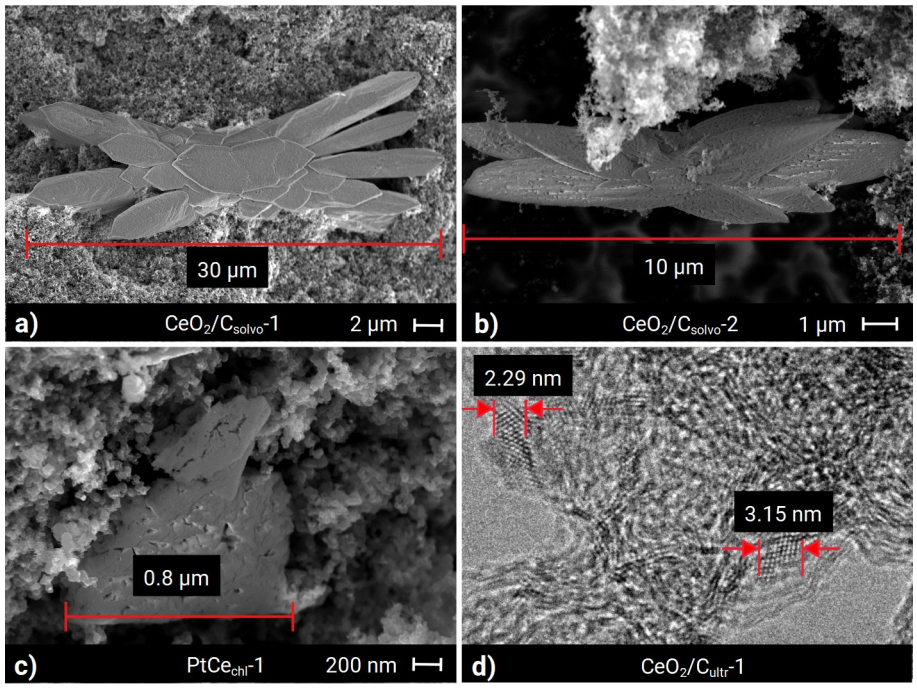

Figure 25. The morphology of ceria crystals synthesised by solvothermal synthesis method (a–c) and the sonochemical synthesis method (d). The scanning electron microscropy (a–c) and transmission electron microscopy (d) was used to visuallize ceria particles.

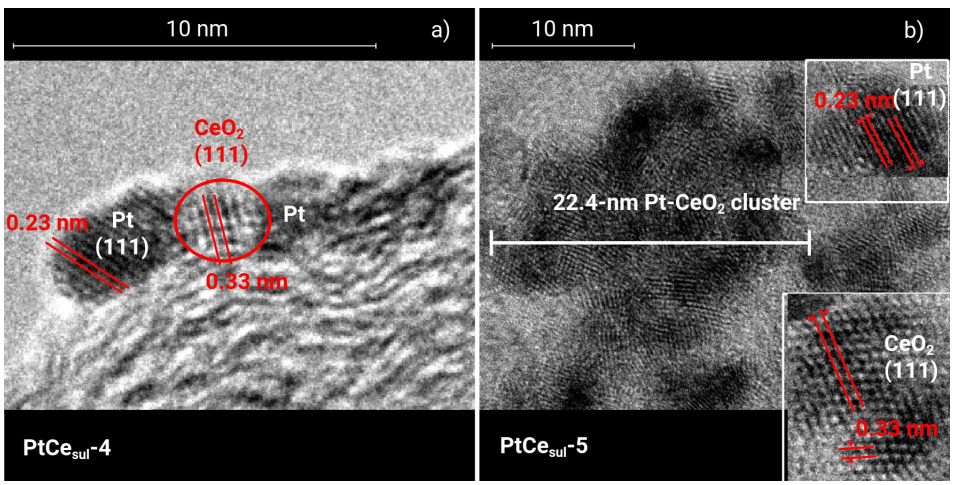

Figure 26. The Pt and CeO_2 nanoparticles of the Pt−CeO_2/C catalysts deposited onto different carbon materials. The inserts demonstrate the interplanar spacing of the Pt(111) and CeO_2(111) of the $PtCe_{sul}$-5.

6.1.3 Chemical Composition, Structure, and Morphology of PtC and Pt−CeO_2/C Materials

The residual mass of studied materials at the end of the TGA experiments (Figure 27) was used to estimated the Pt and CeO_2 wt% in synthesised materials and the completion of Pt and CeO_2 deposition (Table 12). In the case of $PtCe_{NaOH}$ and $PtCe_{Na}$-1 materials, the higher value of residual mass of $PtCe_{Na}$-1 indicates Pt deposition was more completed when the metal sodium was used instead of NaOH. The pre-generation of glycolate anions using the reaction of metallic Na and EG (Equations 6.1 and 6.2) before the EG reduction-deposition method improves the completion of deposition, thus the glycolate anions is a good stabilising reagent for (Chapter 4.2.3).

$$HOC_2H_4OH + OH^- \rightleftharpoons HOC_2H_4O^- + H_2O, \tag{6.1}$$

and

$$2\,HOC_2H_4OH + 2\,Na \longrightarrow 2\,HOC_2H_4O^- + 2\,Na^+ + H_2\uparrow. \tag{6.2}$$

Comparing the residual masses of $PtCe_{Na}$-1 and $PtCe_{Na}$-2 materials suggests that the Pt deposition is even more complete in case of the $PtCe_{Na}$-2. The enhancement of the Pt deposition in this case was caused by the longer ultrasound time ($t_{ultrasound}$ given in the Table 7). This can be explained by the ultrasound effects in the Chapter 4.2.4. The longer duration of refluxing seems not to improve the Pt deposition but facilitates the growth of Pt NPs. This conclusion is based on the results of the preliminary study where significantly larger Pt particles were observed. The deposition of Pt NPs onto the support by adjusting pH with the acid solution can be considered the optimal parameter to achieve complete deposition of Pt NPs in the case of ultrasound- and microwave-assisted methods. In the case of $PtC(KB)_{com}$, PtC(KB), $PtC(Cr_3C_2)$ and $PtCe_{chl}$-1, the residual mass of these materials is close to nominal value. Therefore, all Pt NPs synthesised were deposited completely onto the carbon support. The Pt−CeO_2/C material ($PtCe_{chl}$-1), which was synthesised by the deposition of Pt NPs onto the CeO_2/C_{solvo}-2 material, have higher residual mass than other $PtCe_{chl}$ materials. The dissolution of more crystalline and bigger CeO_2 NPs of $PtCe_{chl}$-1 is kinetically hindered in acidic solutions. On the other hand, the dissolution of amorphous CeO_2 NPs on CeO_2/C_{ultr} materials is kinetically favorable to be dissolved in acidic solution (HCl and H_2SO_4) [80, 154]. Thus, Pt NPs were deposited, however, some amorphous CeO_2 NPs were dissolved during the Pt deposition using HCl or H_2SO_4 solution. This explains the lower residual mass of the $PtCe_{chl}$-2 to 4 and $PtCe_{sul}$-1 to 3 materials.

To achieve a small CeO_2 NPs, which are more crystalline and chemically stable, the use of H_2O_2 and H_3PO_4 for the Pt and CeO_2 deposition was tested. H_2O_2 can help to oxidize Ce^{3+} to Ce^{4+}, i.e. facilitating the formation of CeO_2 [155]. CeO_2 is not so well soluble in H_3PO_4 as the CeO_2 NPs are covered with insoluble $CePO_4$. The CeO_2 NPs with $CePO_4$ layer from CeO_2 still have good

catalytic effects [156, 157]. Another approach to achieve the same goal is to increase the concentration of Ce^{3+} in the microwave synthesis methods. As the microwave treatment can improve slightly the crystallinity of CeO_2 compared to the ultrasound treatment, the higher CeO_2 content can be achieved. This explains high residual mass of the $PtCe_{H_2O_2}$, $PtCe_{H_3PO_4}$, $PtCe_{sul}$-4 and $PtCe_{sul}$-5 materials (Table 12).

The thermal stability of selected materials in synthetic air at temperatures is shown in the Figure 27. The difference in starting temperature of Pt/C and Pt−CeO_2/C materials is insignificant (Figure 27) compared to that of CeO_2/C materials (Figure 24).

The residual mass increases slightly for the materials, which were

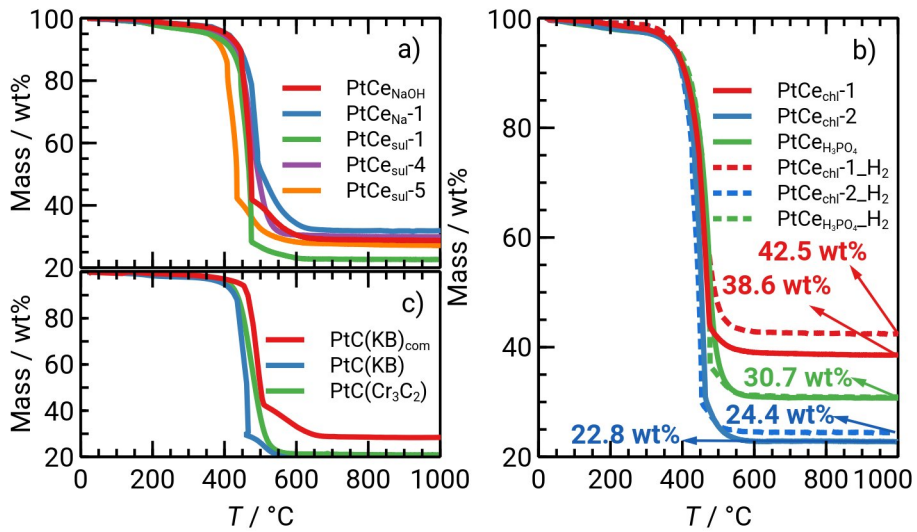

Figure 27. The thermogravimetric analysis of selected Pt-based materials, noted in the figure.

post-treated with hydrogen (Figure 27b). This phenomenon can be explained by removal of some oxides and non-metallic compounds from the catalyst surface in hydrogen environment at high temperature (from 200 °C to 300 °C). In the case of $PtCe_{H_3PO_4}$ and $PtCe_{H_3PO_4}$_H_2 materials (Figure 27b), there is no noticeable difference in residual mass after the hydrogen post-treatment.

The XRD patterns of the Pt and Pt−CeO_2/C materials are shown in the Figure 28. The Pt−CeO_2/C materials ($PtCe_{NaOH}$, $PtCe_{Na}$-1, $PtCe_{Na}$-2 and $PtCe_{chl}$-1), which have been synthesised from CeO_2/C_{solvo} materials, inherited the highly crystalline and large CeO_2 NPs from the corresponding CeO_2/C materials. The diffraction peaks for CeO_2 phase are well-developed at 2θ angles of 29°, 33°, 47°, 56°, 59°, 69°, 77°, 79° and 88°. These diffraction peaks of CeO_2 phase correspond to the *hkl* (111), (200), (220), (311), (222), (400), (331), (420), and (422) planes, respectively [141]. Similarly, the small CeO_2 NPs of the $PtCe_{chl}$-2 to 4, $PtCe_{H_3PO_4}$, $PtCe_{sul}$-1, which are based on the CeO_2/C_{ultr} materials,

Table 12. The chemico-physical characterization results for Pt and PtCe catalysts. The concentration of Pt on electrode surface (c_{Pt}) values has been calculated from CV data measured in 6 mol dm^{-3} HCl solution.

Material	TGA wt%	Pt wt%	CeO_2 wt%	c_{Pt} / $\mu g_{Pt}\,cm^{-2}$
$PtCe_{NaOH}$	29	17[a]	11[a]	18[c]
$PtCe_{Na}$-1	32	21[a]	11[a]	18[c]
$PtCe_{Na}$-2	35	24[a]	10[a]	18[c]
$PtCe_{chl}$-1	39	28[b]	10[b]	18[c]
$PtCe_{chl}$-2	23	24[b]	0.4[b]	18[c]
$PtCe_{chl}$-3	21	20[c]	0.8[c]	18[c]
$PtCe_{chl}$-4	22	20[c]	1.9[c]	18[c]
$PtCe_{H_2O_2}$	30	20[c]	10[c,e]	18[c]
$PtCe_{H_3PO_4}$	31	19[b]	6.3[b,f]	18[c]
$PtCe_{sul}$-1	23	23[b]	0.3[b]	14.4 ± 1.4[d]
$PtCe_{sul}$-2	25	22[b]	0.3[b]	13.7 ± 0.5[d]
$PtCe_{sul}$-3	20	23[b]	0.3[b]	14.9 ± 0.2[d]
$PtCe_{sul}$-4	27	23[b]	5.1[b]	14.1 ± 1.7[d]
$PtCe_{sul}$-5	30	22[b]	7.4[b]	14.5 ± 0.3[d]
$PtC(KB)_{com}$	28	28	–	18[c]
PtC(KB)	18	21[b]	–	13.0 ± 0.4[d]
$PtC(Cr_3C_2)$	21	20[b]	–	12.5 ± 2.2[d]
$PtCe_{chl}$-1_H_2	43	33[b]	12[b]	18[c]
$PtCe_{chl}$-2_H_2	24	26[b]	0.42[b]	18[c]
$PtCe_{H_3PO_4}$_H_2	31	19[b]	6.0[b,f]	18[c]

[a]The Pt wt% has been estimated from the thermogravimetric analysis (TGA) results of CeO_2-C substrate and final $Pt-CeO_2/C$ catalyst.
[b]The wt% has been estimated from the results of microwave-plasma atomic emission spectrometry.
[c]The wt% has been nominated for Pt, CeO_2 wt% is the estimated based on the TGA results and nominal Pt wt%.
[d]The Pt concentration on the electrode surface has been estimated from the electrochemical Pt dissolution results.
[e]This value should refer to the weight percentage of general cerium compounds, because many cerium phases were found, e.g CeO_2, Ce_2O_3 and $Ce(OH)_3$.
[f]This value should refer to the weight percentage of cerium, because many cerium phases were found, e.g CeO_2 and $CePO_4$.

result in the broad and low intensity diffraction peaks of CeO_2. Therefore, these diffraction peaks were underdeveloped in corresponding Pt-based catalyst. In the case of the $PtCe_{H_3PO_4}$ material, there are some visible diffraction peaks for

Table 13. The Pt diameters for Pt and PtCe catalysts estimated from various methods. The electrochemcial active surface area (ECSA) value for Pt nanoparticles in 0.5 mol dm^{-3} H_2SO_4 solution saturated with argon has been calculated from CV data.

Material	$d_{\mathrm{Pt,\,XRD}}$ / nm	$d_{\mathrm{Pt,\,microscopy}}$ / nm	$d_{\mathrm{CeO_2,\,XRD}}$ / nm	ECSA / $m^2_{Pt}\,g^{-1}_{Pt}$
$PtCe_{NaOH}$	1.6	3.0±0.7[a]	11.0	42±1
$PtCe_{Na}$-1	3.0	4.2±1.4[a]	11.0	55±3
$PtCe_{Na}$-2	2.4	4.2±0.9[a]	10.0	45±2
$PtCe_{chl}$-1	1.5	4.4 ± 3.1[b]	9.8	72±7
$PtCe_{chl}$-2	1.1	3.8 ± 1.5[b]	3.0	91±7
$PtCe_{chl}$-3	0.9	2.8 ± 0.8[b]	3.0	77±4
$PtCe_{chl}$-4	1.4	2.9 ± 1.9[b]	1.0	72±1
$PtCe_{H_2O_2}$	1.7	–	1.0[c]	23
$PtCe_{H_3PO_4}$	1.4	–	2.9[d]	56±3
$PtCe_{sul}$-1	1.1	3.6 ± 1.5	1.0	88±5
$PtCe_{sul}$-2	1.0	4.1 ± 1.4	0.7	76±12
$PtCe_{sul}$-3	0.9	3.1 ± 0.9	1.0	89±1
$PtCe_{sul}$-4	0.7	3.4 ± 1.1	0.7	87±5
$PtCe_{sul}$-5	0.9	7.2 ± 3.8	5.1	61±3
$PtC(KB)_{com}$	2.0	5.5±1.3[a]	–	55±7
PtC(KB)	1.4	3.3 ± 1.2	–	82±1
$PtC(Cr_3C_2)$	1.5	7.2 ± 3.8	–	71±4
$PtCe_{chl}$-1_H_2	2.4	–	9.8	57
$PtCe_{chl}$-2_H_2	1.1[e]	–	0.7	65±2
$PtCe_{H_3PO_4}$_H_2	2.0	–	1.0[d]	52

[a]The Pt particle size was estimated from the scanning electron microscopic images and the peak of the distribution was around values given in the table.
[b]The Pt particle size was estimated from the transmission electron microscopic images.
[c]The presence of other cerium phases such as Ce_2O_3 (with crystallite size ca. 1.6 nm) and $Ce(OH)_3$ has been observed.
[d]Another structural phase was cerium phosphate ($CePO_4$) with the crystallite size approximately 4.5 nm.
[e]Another Pt phase with bigger diameter size (ca. 13.5 nm) has been observed.

$CePO_4$ phase at 2θ of 20°, 29°, 31°, 53°, 60° and 71°. As the CeO_2, which was synthesised by ultrasound and microwave methods, tends to be small (Chapter 4.2.4), the Pt−CeO_2/C materials, which have been co-deposited with Pt and Ce_{ultr} (or Ce_{MW}) onto a carbon support, had the similar XRD pattern has discussed before. Although the C(Cr_3C_2, 900) carbon material was ball-milled before the Pt and CeO_2 deposition, the $PtCe_{sul}$-5 material still has characteristic diffraction peaks of the carbon support at 2θ angle of 26°, which corresponds to the C(002) plane. The $d_{CeO_2,\,XRD}$ of Pt−CeO_2/C materials (Table 13) increased slightly compared to that of a corresponding CeO_2/C materials (Table 11).

The diffraction peaks of Pt phase for all materials are visible at 2θ angles of 40°, 46°, 68°, 82° and 86°, which corresponds to the Pt (*hkl*) planes (111), (200), (311), (331), (222), respectively in the Figure 28 [158]. The influence of the Pt deposition method on the characteristics of Pt NPs can be observed. Although the Pt NPs of $PtCe_{NaOH}$, $PtCe_{Na}$-1 and $PtCe_{Na}$-2 materials were deposited using the combination of various heating methods, the intensity of diffraction peaks is higher, and the peaks are sharper if the metallic Na was used instead of NaOH. Therefore, larger Pt crytallites were synthesised and this agrees well with $d_{Pt,\,XRD}$, in the Table 13. Comparison of the $PtCe_{Na}$-1 and $PtCe_{Na}$-2 materials demonstrates that the increase of $t_{ultrasound}$ (given in the Table 7) does not increase the $d_{Pt,\,XRD}$ values. The Pt deposition assisted by adjusting pH value of reaction mixture resulted in the board and low intensity diffraction peaks of Pt NPs. The $d_{Pt,\,XRD}$ values for these Pt and Pt−CeO_2/C materials are smaller than 2.0 nm (Table 13). The use of H_2O_2 for Pt deposition generated Pt NPs with a $d_{Pt,\,XRD}$ value (1.7 nm) as small as that by adjusting pH of reaction mixture with the use of acid solutions, however, the diffraction peaks of Pt NPs are slightly sharper.

The hydrogen treatment increased the $d_{Pt,\,XRD}$ value, which resulted in the sharpness of Pt diffraction peaks (Figure 28c). Some Pt crystallites became dramatically bigger (14 nm) as in the case of $PtCe_{chl}$-2_H_2 while the $d_{Pt,\,XRD}$ for other two materials increased slightly, i.e. from 1.5 to 2.4 nm and from 1.4 to 2.0 nm in the case of $PtCe_{chl}$-1 and $PtCe_{H_3PO_4}$ materials, respectively (Table 13). It is obvious that the hydrogen treatment increases the Pt diameter. The CeO_2 diameter ($d_{CeO_2,\,XRD}$) for big CeO_2 particles of the $PtCe_{chl}$-1 is unchanged after the treatment, however, for smaller CeO_2 NPs of the $PtCe_{chl}$-2 and $PtCe_{H_3PO_4}$, the $d_{CeO_2,\,XRD}$ values are reduced from 3.0 to 0.7 nm, and from 2.9 to 1.0 nm, respectively. The shifts in the $d_{Pt,\,XRD}$ and $d_{CeO_2,\,XRD}$ values can caused different effects on the MOR activity.

The porosity of the Pt and Pt−CeO_2/C materials was measured and the data are presented in the Table 10 and Figure 29. The PWD inherited from the carbon support. Although C(KB) and C(Cr_3C_2, 900) have different V_{total} value, the PWD of both carbon support are similar. Both carbon materials have two regions in the PWD plot. The first PWD region is around 1 nm and the second PWD region is from 2 to 20 nm (mesopores) in the Figure 29. After the metal deposition, the

V_{total} value was reduced compared to the V_{total} value of the corresponding carbon support because the carbon amount in the catalyst is lower and the porosity in mainly caused by the catalyst support. In the case of the C(KB) and C(Cr_3C_2, 900) support materials, the relationship of V_{total} and carbon percentage is established. Therefore the pores of carbon support are not clogged. As the carbon structure is retained, the $V_{mesopores}/V_{total}$ does not influenced by the deposition of Pt and CeO_2 NPs

The Raman spectroscopy has been applied to investigate the characteristics

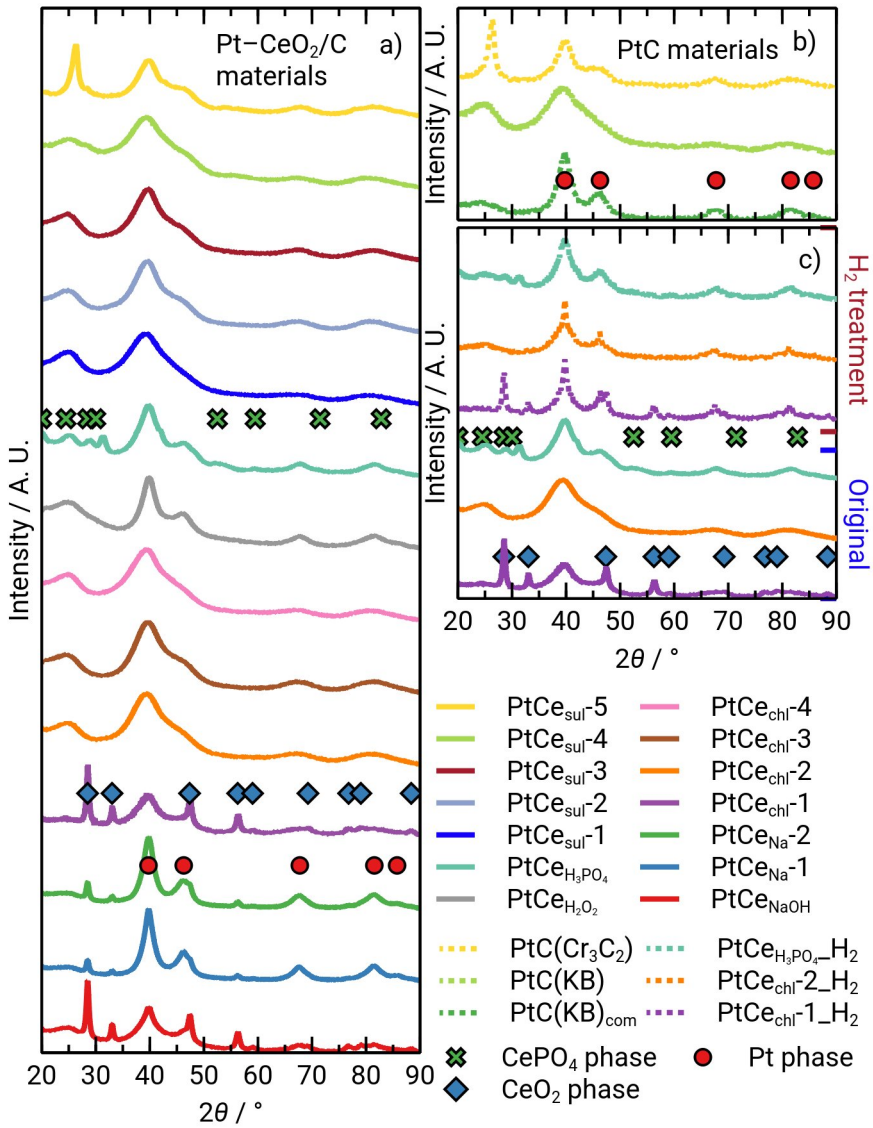

Figure 28. X-ray diffractorgrams of Pt−CeO_2/C and PtC materials, noted in the figure.

of the CeO_2 NPs parameters given in the Figure 30. Besides, the Raman spectra at the region $> 1000\,cm^{-1}$ (Figure 30a) also revealed the carbon structure of the catalyst materials. The high intensity of D-band ($\approx 1358\,cm^{-1}$) and the position of G-band at $\approx 1583\,cm^{-1}$ indicated that both C(KB) and the ball-milled C(Cr_3C_2, 900) support materials were amorphous, and probably, belong to the stage I of the carbon graphitization [111]. However, the spike of 2D-band at $2704\,cm^{-1}$ in the case of the $PtCe_{sul}$-5 was the typical feature of the stage II for a nanocrystalline graphite carbon. Obviously, the ball-milling treatment increased the amorphous carbon for the C(Cr_3C_2, 900) material, but some of the nanocrystalline graphite retained. The findings agree well with XRD results as the $PtCe_{sul}$-5 and PtC(Cr_3C_2) had a sharp spike at 26° of 2θ for C(002) plane. In the smaller wavenumber region $< 1000\,cm^{-1}$, the CeO_2/C_{solvo}-1 had the F_{2g} peak at $466\,cm^{-1}$ overlapping with data for pure CeO_2 NPs [116]. However, the

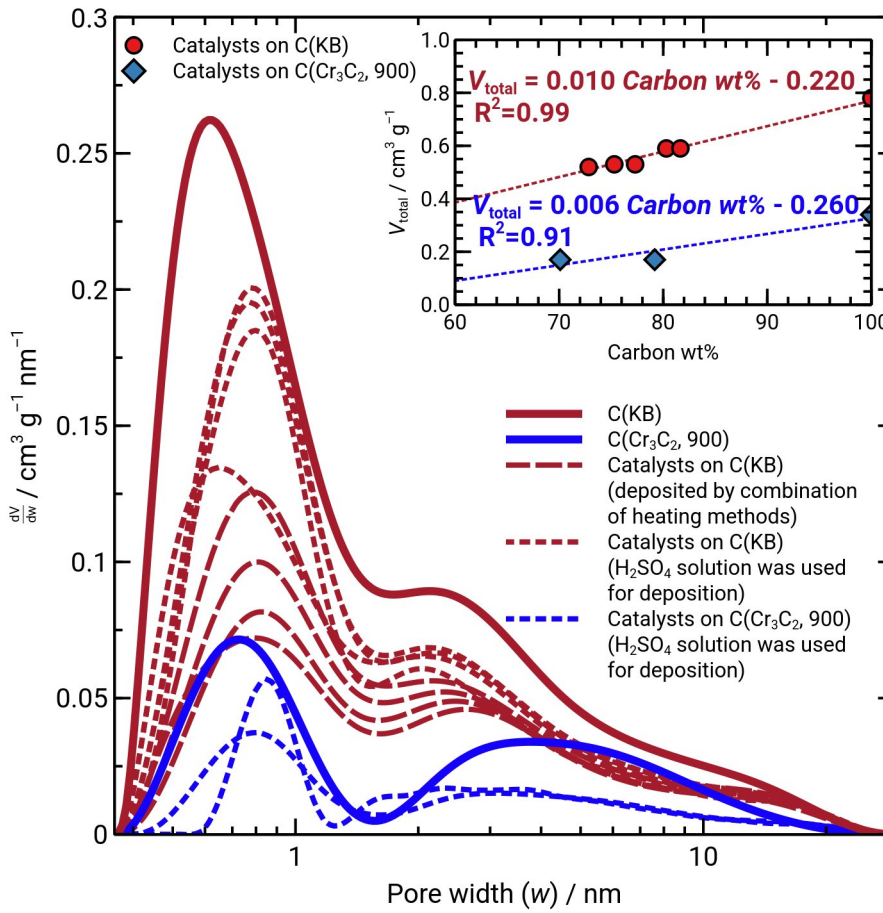

Figure 29. Pore-width distribution of different carbon supports and catalyst deposited onto these supports, noted in the figure. Insert: the correlation between the total pore volume and carbon percentatge in the catalyst.

CeO_2 NPs dispersed on a large area of the carbon support material resulted in the low signal intensity. The F_{2g} peak was blue shifted from 466 to 451 cm^{-1} after the deposition of Pt NPs. The broad peaks at around 550 and 690 cm^{-1} were the asymmetry and symmetry linkages of Pt−O−Ce, respectively [114]. The stretching mode of CeO_2 at 550 cm^{-1} (D_{CeO_2}) can be used to compare the number of oxygen vacancies [19]. The higher value for the intensity ratio of $I_{D_{CeO_2}}/I_{F_{2g}}$ indicated higher number of oxygen vacancies. Therefore, the number of oxygen vacancies in the $PtCe_{sul}$-4 and $PtCe_{sul}$-5 materials are the highest. The F_{2g} peaks for the $PtCe_{sul}$-3 have been observed at 466 cm^{-1} with weak intensity due to the low CeO_2 content and small CeO_2 NPs [19]. There were no observation for Pt−CeO_2 vibration feature of the $PtCe_{sul}$-3 material.

The dispersion of Pt NPs on carbon support materials washas been

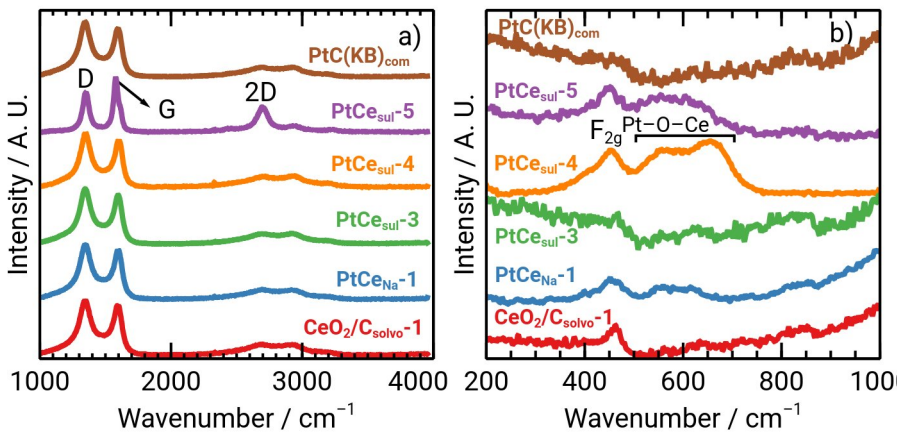

Figure 30. Raman spectra for selected materials, noted in the figure.

investigated by CV, SEM and TEM methods. The CV data measured in 0.5 mol dm^{-3} H_2SO_4 solution saturated with argon were used to estimate the ECSA of Pt from the adsorption and desorption data of protons at the active site of Pt. Therefore, the ECSA value can be used to compare the dispersion of Pt on the electrode surface.

Although the $d_{Pt,\,XRD}$ of the $PtCe_{H_2O_2}$ was small, the ECSA value was small (Table 12). This indicated that the exposed surface of Pt to the electrolyte solution is small and probably, the Pt NPs were agglomerated due to the robust reduction of concentrated H_2O_2 solution. The ECSA value for other materials calculated are from 42 to 91 $m^2_{Pt}\,g^{-1}_{Pt}$ given in the Table 12. These values were shown some improvement of the Pt dispersion, however, the ECSA value $\leq$ 55 $m^2_{Pt}\,g^{-1}_{Pt}$ indicate the agglomeration of Pt NPs.

In the Figure 31, the Pt NPs deposited using the combination of different heating methods are dispersed pretty well on the carbon support, however, some agglomeration was visible too. The dispersion of the Pt NPs deposited using the HCl solution demonstrated in the Figure 32 was much higher compared to the

previous case demonstrated in the Figure 31. From the TEM images, the Pt NPs linear dimension are around 2 to 3 nm. The interplanar spacing of Pt lattice fringe was 0.23 nm, which corresponds to the the *hkl* (111) plane structure [119]. The dispersion of Pt NPs deposited using the H_2SO_4 solution is as well as in the case of using HCl solution (see Figure 33). In the case of C(KB)-based materials (Figure 33a–c, f and h), the most particle size distribution (PSD) count is around 2.5 nm, and PSD patterns of the $PtCe_{sul}$ materials are similar. The averaged diameter for these materials ranging from 2.5 ± 0.9 to 3.3 ± 1.1 nm. Almost no agglomerates can be detected. Therefore, the synthesis method for Pt deposition on C(KB)-based materials was repeatable, even if the synthesis methods for CeO_2 particles were different in each case. The $Ce(NO_3)_3$ concentration used during the CeO_2 synthesis is not influenced the Pt deposition if Pt PSD of the $PtCe_{sul}$-4 catalyst is compared to other $PtCe_{sul}$ catalysts on C(KB). In the case of $C(Cr_3C_2, 900)$-based materials (Figure 33e and g), the Pt NPs are slightly agglomerated due to the lower S_{DFT} value of $C(Cr_3C_2, 900)$ (around $213\,m^2\,g^{-1}$, see Table 10). However, the diameter of most Pt particles ranges from 2 to 4 nm. The Pt PSD patterns of $PtCe_{sul}$-5 and $PtC(Cr_3C_2)$ materials are surprisingly similar, and the averaged diameter of Pt NPs is around (4.3 ± 2.3) nm. This confirmed the success of the Pt deposition method on $C(Cr_3C_2, 900)$-based materials. In comparison with commercial Vulcan carbon support, which has a similar S_{DFT} value (around $243\,m^2\,g^{-1}$ [73], the commercial Pt/C(Vulcan) is extensively agglomerated with diverse particle sizes and most of the Pt particles distributed from 5 to 7 nm (Figure 33d). The volume to area diameter of Pt [127], $d_{Pt,\,microscopy}$, was calculated and given in the Table 13.

The stability of the $PtCe_{Na}$-1 and $PtC(KB)_{com}$ has been analyzed using the CV measurement in the solution of $0.5\,mol\,dm^{-3}$ H_2SO_4 and $1\,mol\,dm^{-3}$ CH_3OH at the scan rate of $50\,mV\,s^{-1}$ for 5000 cycles. There were no big differences in the stability of the $PtCe_{Na}$-1 and $PtC(KB)_{com}$ materials demonstrated in the Figure 34a. The MOR activity remained roughly 60%. However, the Pt NPs of the $PtCe_{Na}$-1 material became bigger (Figure 34b), and some of the Pt was dissolved as the number of Pt NPs was observed slightly less compared to original $PtCe_{Na}$-1 material in the Figure 31.

6.2 Oxygen Reduction Reaction

6.2.1 The Oxygen Reduction Reaction on Chromium Carbide-Derived Carbon Materials

The capacitive behavior of the CDC is illustrated in the Figure 35 using the CV and EIS measurement data. The gravimetric capacitance values calculated for four CDC materials in the Figure 35a, agree well with the porosity values for these materials, which has been discussed in Chapter 6.1.1, i.e. the $C(Cr_3C_2, 800)$ material has the highest gravimetric capacitance and for other $C(Cr_3C_2)$ the gravimetric capacitance is very similar about two to three times

lower. The capacitances of series and parallel circuits are noted as C_s (Equation 6.4) and C_p (Equation 6.3), respectively.

$$C_p = \frac{-Z''}{2\pi f|Z|}, \tag{6.3}$$

$$C_s = -\frac{1}{2\pi f Z''}, \tag{6.4}$$

$$|Z| = \sqrt{Z'^2 + Z''^2}, \tag{6.5}$$

where Z' is the real and Z'' is the imaginary part of the complex impedance, and $|Z|$ impedance modulus.

All $C(Cr_3C_2)$ materials reveal the blocking capacitive behavior as the corresponding C_p and C_s calculated coincide at $f \to 0$. There is very nice agreement between the series capacitance C_s at $f \to 0$ and S_{DFT} of $C(Cr_3C_2)$ materials, i.e. series capacitance decreases in order $C(Cr_3C_2, 800) \gg C(Cr_3C_2, 1000) > C(Cr_3C_2, 900) \approx C(Cr_3C_2, 1100)$.

The CV method was used to estimate the ORR activity of $C(Cr_3C_2)$ materials in oxygen saturated 0.1 mol dm^{-3} $HClO_4$ solution (Figure 36a and b). In the

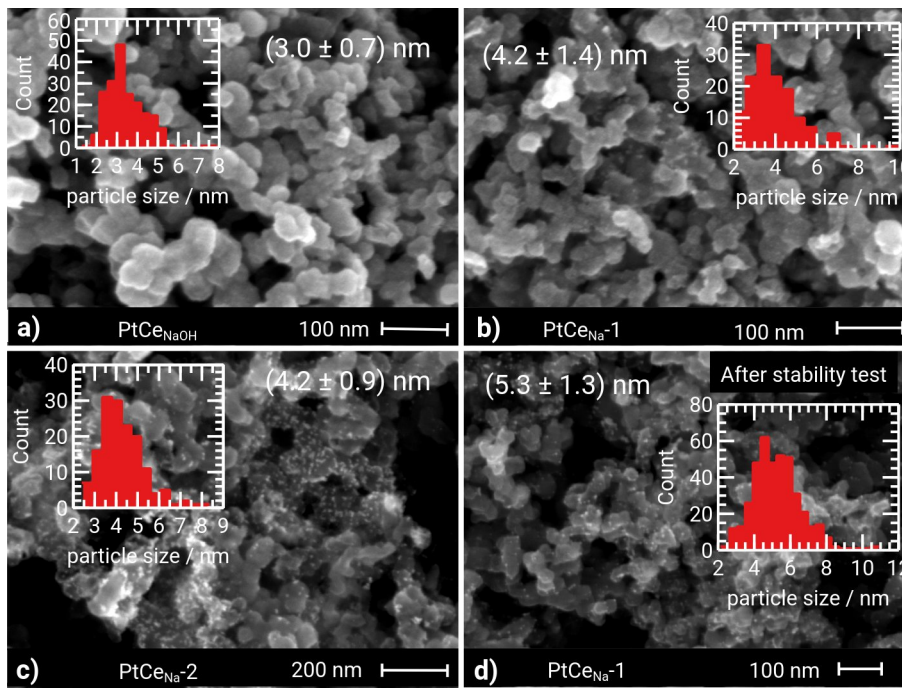

Figure 31. The Pt NPs distribution images (a–c) for Pt−CeO_2/C catalysts, synthesised using the combination of heating methods, obtained from the scanning electron microscopy (SEM) experiments were shown. The SEM image for PtCe$_{Na}$-1 (d) revealed that the Pt NPs retained after an accelerated stability test in a mixture of 0.5 mol dm^{-3} H_2SO_4 and 0.1 mol dm^{-3} CH_3OH solution.

Figure 36a, there are two ORR peaks clearly visible during the cathodic potential scan for all C(Cr_3C_2) materials. These peaks indicate the corresponding electron processes of the ORR on the carbon surface. The first ORR peak, E_{peak}, which corresponds to the first electron transfer (Equation 4.31), and E_{peak} is plotted against the ln(v) in the Figure 36b to observed the changes of ORR with different potential scan rates, and indicates that ORR is irreversible on these materials. The E_{peak} value shifts towards more negative potentials with the increase of the synthesis temperature of C(Cr_3C_2) materials, indicating that the ORR catalytic activity decreases as the carbon becomes more graphitised.

The RDE results for C(Cr_3C_2) materials, which were measured in 0.1 mol dm^{-3} $HClO_4$ solution saturated with oxygen, are presented in the Figure 36c. The E_{onset} potential value in the Figure 36c can also be used to compare the ORR activity of the CDC materials. Therefore, the ORR activity decreases in the order C(Cr_3C_2, 800) (E_{onset} = 0.63 V) > C(Cr_3C_2, 900) (E_{onset} = 0.53 V) > C(Cr_3C_2, 1000) (E_{onset} = 0.43 V) > C(Cr_3C_2, 1000) (E_{onset} = 0.23

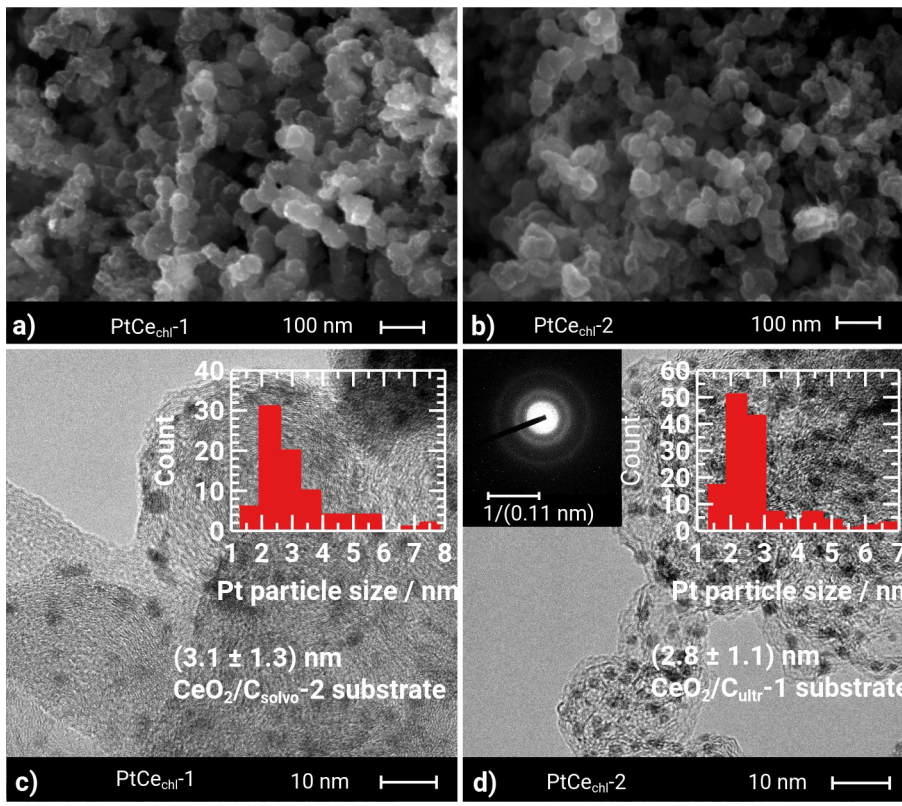

Figure 32. The Pt NPs that were deposited onto the catalyst support surface by using the HCl acid solution for sedimentation was shown under high-resolution scanning electron microscopy (a,b) and transmission electron microscopy images (c,d). Insert: Electron diffraction pattern of PtCe$_{chl}$-2 material.

V). No current density plateau has been formed, which should be reached in the diffusion-limited regime in the range of potentials applied. The Tafel-like plot given in the Figure 36d, was used to explain the ORR kinetics at CDC materials. The Tafel-like curves are not linear. However the slope values in the limited nearly linear region at low current densities can be used to estimate the kinetics. The Tafel-like slope values for the C(Cr_3C_2, 800), C(Cr_3C_2, 900), C(Cr_3C_2, 1000) and C(Cr_3C_2, 1100) materials (in the nearly linear region) were 181, 220, 253 and 253 mV, respectively. The slope values are higher compared with the typical slope value for a GCDE was around 140 mV [58]. However,

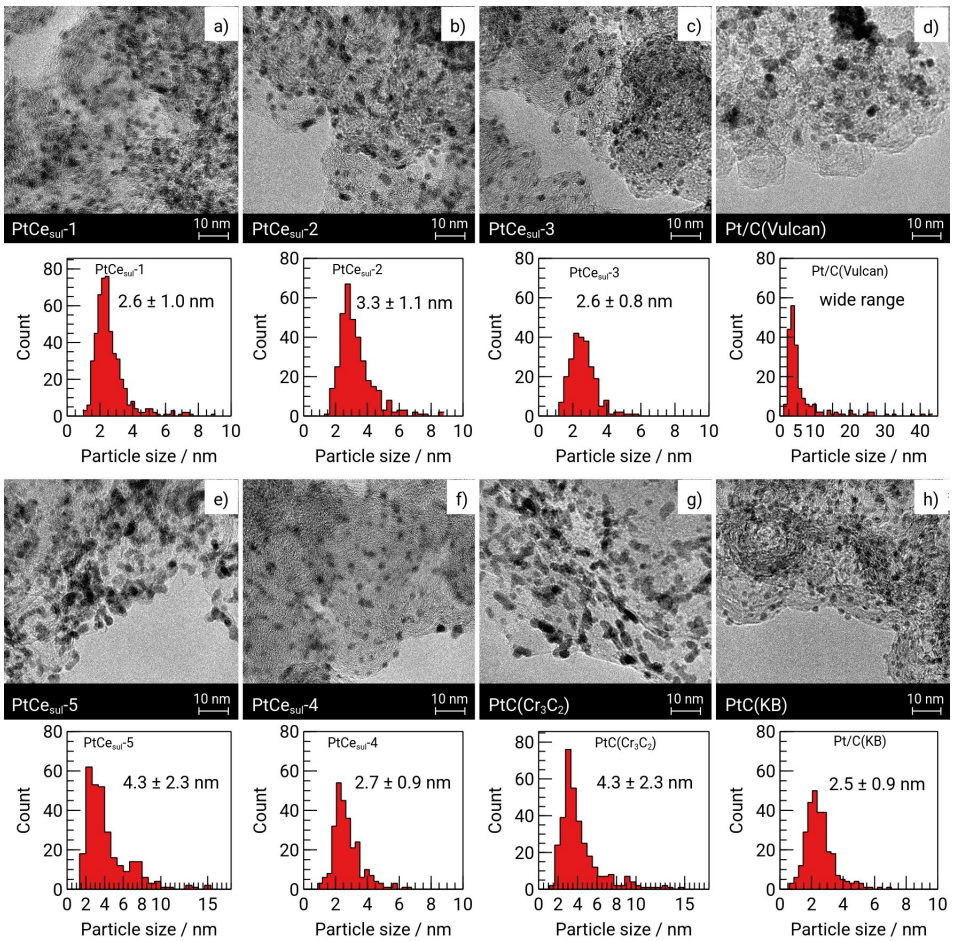

Figure 33. The dispersion of Pt nanoparticles of Pt−CeO_2/C and Pt/C materials deposited using addition of the H_2SO_4 solution to the Pt colloid solution. The histogram of the Pt particle diameter estimated by measuring more than 200 particles, is placed under the transmission electron microscopy image of the corresponding material above. The averaged number diameter of Pt nanoparticles is given in the histogram of each material.

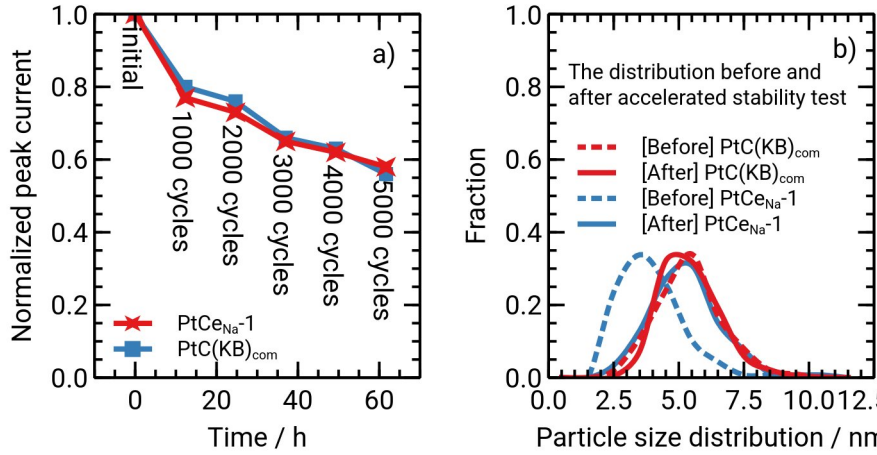

Figure 34. The accelerated stability test (AST) results (a) for $PtCe_{Na}$-1 and $PtC(KB)_{com}$ materials, and the change in the Pt particle size after the AST test (b) estimated from the high-resolution scanning electron microscopic images. The AST was carried out in a solution of 0.5 mol dm^{-3} H_2SO_4 and 1 mol dm^{-3} CH_3OH by performing the cyclic voltammetry (CV) at 0.05 V s^{-1} within the potential window from 0.06 to 1.10 V, for 5000 cycles. The normalised peak current is the ratio of CV anodic peak current at the n^{th} cycle to the initially stable anodic peak current.

these high values are not unusual for a thick electrode in an acidic solution, as observed in the work of Taleb *et al.* [57]. The higher Tafel-like slope value (>220 mV) can be caused by the hydrogen evolution [58], which is a reasonable

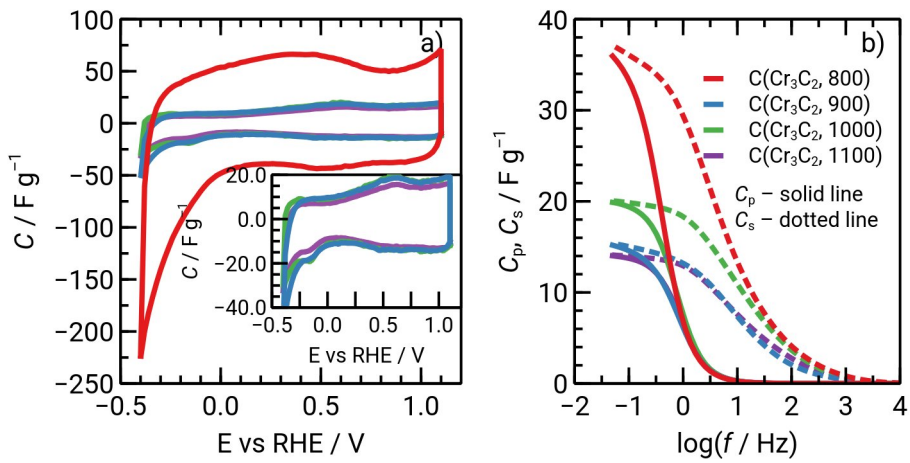

Figure 35. (a) Gravimetric capacitance vs potential, and (b) dependence of series and parallel capacitance of frequency log f at 0.80 V for the chromium carbide-derived carbon materials in 0.1 mol dm^{-3} $HClO_4$ solution saturated with argon. Insert in part a: magnification of part a for selected materials.

explanation in our case as small bubbles on the electrode surface were observed at most cathodic potentials, even during the electrode activation step in the 0.1 mol dm^{-3} $HClO_4$ solution saturated argon. The higher Tafel-like slope values indicated that the first electron transfer to $O_{2(ads)}$ (Equation 4.31) was sluggish and required a large activation energy for the ORR process. Besides, the curvature of the Tafel-like plots can be caused by diffusion-limited processes in a thick porous electrode layer.

6.2.2 Influence of Heating Method and Formation of Glycolate-Based System on Pt-based Catalysts ORR Characteristics

The $PtCe_{Na}$-1 and $PtCe_{chl}$-1 materials have the same type of CeO_2 NPs as similar EG reduction synthesis procedure was used. However, the influence of heating methods during the synthesis of Pt NPs can be revealed by comparing these two

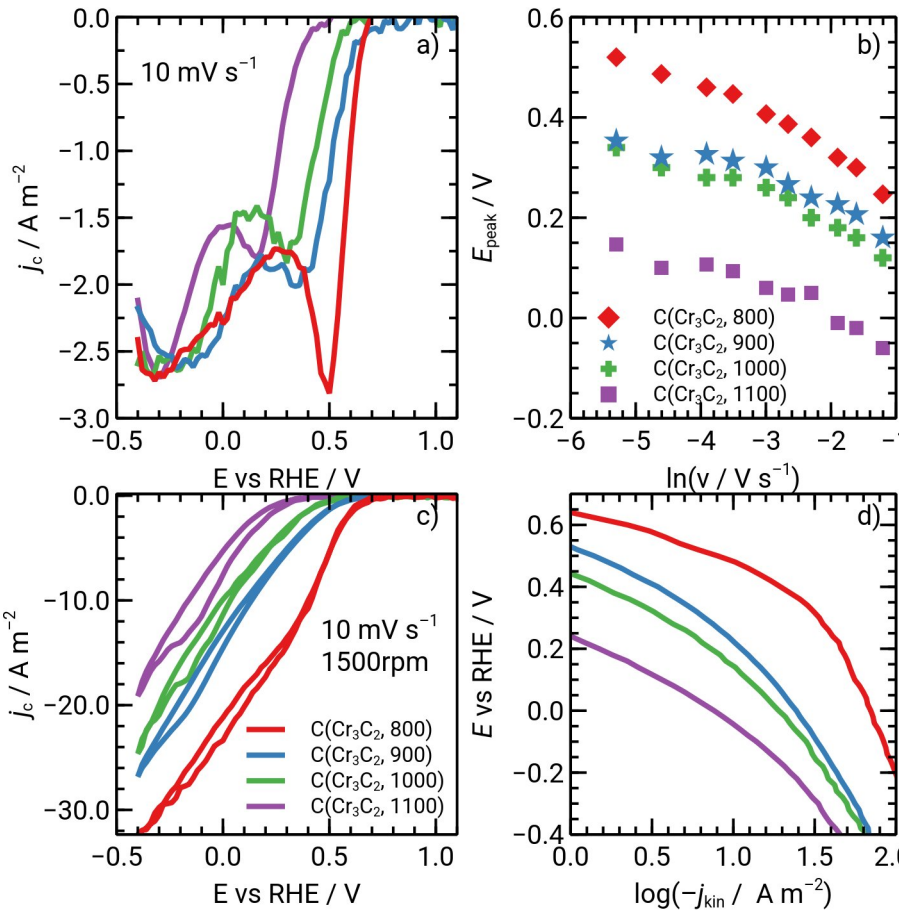

Figure 36. Oxygen reduction reaction activity of chromium carbide-derived carbon materials in 0.1 mol dm^{-3} $HClO_4$ solution saturated oxygen.

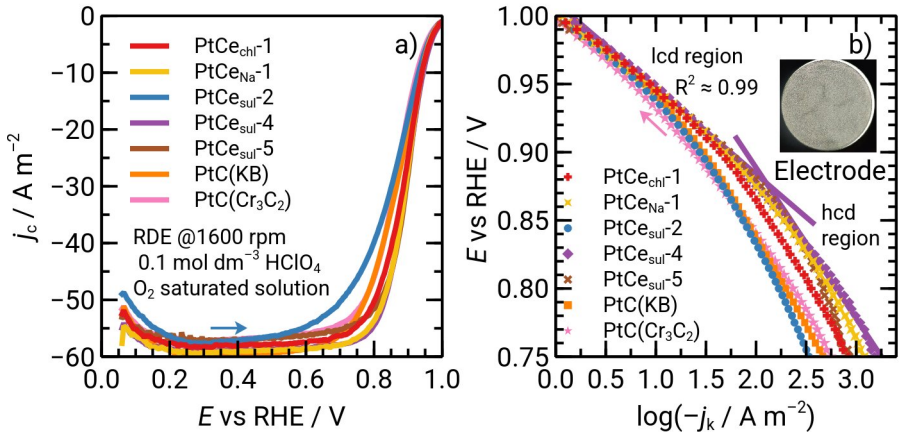

Figure 37. The rotating disk electrode (RDE) data (corrected with background current density) presented in the plot of oxygen reduction reaction current density versus the overpotentialfor Pt-based materials synthesised (a) and the Tafel-like plots constructed based on the corresponding RDE data (b). Insert: The electrode surface under the view of an optical microscope.

materials. The Tafel-like slope values of PtCe$_{Na}$-1 and PtCe$_{chl}$-1 materials in both low current density (lcd) (0.90–1.00 V) and high current density (hcd) (0.75–0.85 V) indicate that the ORR kinetics of these two materials is similar (Table 14 and Figure 37). However, the SA value of PtCe$_{Na}$-1 is 1.4 times larger than that for the PtCe$_{chl}$-1 catalyst. This indicates that PtCe$_{Na}$-1 has a higher intrinsic ORR activity than the PtCe$_{chl}$-1 catalyst. The j_k values for both materials in hcd agreed well with the SA value and were typical for a smooth surface Pt/C catalysts [133, 134]. Thus, the PtCe$_{Na}$-1 material has higher intrinsic ORR activity due to the use of glycolate anions and the combination of heating methods to synthesise Pt NPs.

6.2.3 Influences of CeO_2 on ORR Characteristics of Pt-based Catatlysts

There is no measurably electrochemical effect of using H_2SO_4 instead of HCl solution for the sedimentation of Pt NPs onto carbon support surface from colloid solution. Therefore, the comparison between the ORR activity for PtCe$_{chl}$-1 and PtCe$_{sul}$-2 materials is justified. The influence of CeO_2 NPs synthesised by solvothermal, sonochemical and microwave synthesis methods on the ORR activity can be investigated.

In the study by Lu *et al.* [19], the ORR activity of the Pt−CeO_2/C(nitrogen-doped carbon) enhances as the CeO_2 content increases. However, in case of materials investigated in this work, the PtCe$_{chl}$-1 material with the highest CeO_2 content had lower ORR activity (241 A g_{Pt}^{-1}, and 2.9 A m_{Pt}^{-2}) compared with that for PtCe$_{sul}$-4 material ((357 ± 72) A g_{Pt}^{-1}, and

$(4.0 \pm 0.1)\,\mathrm{A\,m_{Pt}^{-2}}$ Table 14). Therefore, the influence of the morphology and physical properties of CeO_2 NPs on the ORR is much stronger than CeO_2 content in catalysts. This phenomenon can be explained by different number of active sites of CeO_2 NPs, which facilitates the oxidation of peroxide to water (Equation 4.11 – 4.13), especially in the potential region below 0.8 V where the peroxide pathway may take place. The ORR activity given in the Table 14 increases in the following order of materials: $PtCe_{sul}$-2 (ultrasound method, polygon shape, $d_{CeO_2} \approx 3$ nm) < $PtCe_{chl}$-1 (solvothermal method, flower shape, $d_{CeO_2} \approx 1$ µm) < $PtCe_{sul}$-4 (microwave method, polygon shape, $d_{CeO_2} \approx 3$ nm).

It is possible to compare the ORR activities of $Pt{-}CeO_2$/C and PtC catalysts, the PtC(KB) and PtC(Cr_3C_2) were synthesised using the same carbon support and the same synthesis parameters as for the syntheses of the $PtCe_{sul}$-4 and $PtCe_{sul}$-5, respectively (given in the Table 7). The ORR activity (both MA and SA) for $Pt{-}CeO_2$/C catalysts on C(KB) ($PtCe_{sul}$-4) and on C(Cr_3C_2, 900) ($PtCe_{sul}$-5) was higher than that for PtC(KB) and PtC(Cr_3C_2), respectively, demonstrated in Table 14 and Figure 37. At the same time, ECSA is comparable for these materials. This result agrees well with the results of other studies [19, 46] indicating that the presence of CeO_2 enhances the ORR and the performance of PEMFCs.

Table 14. The oxygen reduction reaction results calculated from rotating disk electrode data that was measured $0.1\,\mathrm{mol\,dm^{-3}}$ $HClO_4$ solution saturated with oxygen.

Material	MA @0.9 V / $\mathrm{A\,g_{Pt}^{-1}}$	SA @0.9 V / $\mathrm{A\,m_{Pt}^{-2}}$	Tafel-like slope[a] (1.00–0.90 V) / mV	Tafel-like slope[a] (0.85–0.75 V) / mV
$PtCe_{Na}$-1	230	4.0	59	124
$PtCe_{chl}$-1	241	2.9	61	126
$PtCe_{sul}$-2	199±14	2.0±0.1	70±1	155±24
$PtCe_{sul}$-4	357±72	3.3±0.2	63 ±3	110±6
$PtCe_{sul}$-5	288±1	4.0±0.1	57±1	168±8
PtC(KB)	234±36	2.0±0.2	73±5	133±11
PtC(Cr_3C_2)	192±16	2.3±0.1	71±1	118±4

[a]The linear regression line has the $R^2 \approx 0.99$

6.2.4 Influence of Chromium Carbide-Derived Carbon Support on ORR Characteristics of Pt-based Catatlysts

Although the ORR activity for Pt/C materials is in the same range, the ORR activity of the PtC(Cr_3C_2) material was slightly higher than that of the PtC(KB) material (Table 14). Thus, the C(Cr_3C_2, 900) support facilitates the ORR on PtC catalysts.

The comparison of Pt−CeO_2/C catalyst activities on different carbon support materials indicates that the MA values of $PtCe_{sul}$-4 and $PtCe_{sul}$-5 materials are in the same range. However, the SA value and the Tafel-like plot slope value in lcd region of the $PtCe_{sul}$-5 indicated that this material has higher ORR activity as the oxygen dissociative pathway seems to be dominant (see Chapter 4.1.3). Therefore, the ORR kinetics at $PtCe_{sul}$-5 material is faster than that at $PtCe_{sul}$-4. As the associative pathway is domiant below 0.8 V (Chapter 4.1.3), the ORR kinetics of $PtCe_{sul}$-4 material is faster than that of $PtCe_{sul}$-5 material, and the Tafel-like plot slope value in the hcd region is smaller. Thus, the enhancement of the ORR activity can be also detected for the Pt−CeO_2/C catalyst if the C(Cr_3C_2, 900) support material. The shift of the Tafel-like plot slope value in the hcd region toward the higher value than 120 mV can be influenced by the changes in oxide coverage of Pt electrode surface [133].

6.3 Methanol Oxidation Reaction

6.3.1 Manipulation of EG Reduction Methods by Glycolate Anions

In the Chapter 6.1.3, influence of the pre-generation of glycolate anions using NaOH or Na on the characteristics of the Pt NPs was discussed (see also Chapter 6.1.3). The characteristics of Pt NPs are obviously different for $PtCe_{NaOH}$ and $PtCe_{Na}$-1 materials. Especially the ECSA value, which is higher for the $PtCe_{Na}$-1 than that for the $PtCe_{NaOH}$ material (Table 12). In the EDL potential region, the gravimetric capacitance vs electrode potential curves for the $PtCe_{NaOH}$ and $PtCe_{Na}$-1 materials overlay, as shown in the Figure 38a. This indicates that these materials have similar carbon surface area because the capacitance in the EDL region is mainly influenced by support material. In comparison of the maximum MOR activity, the $i_{ap,\,CV}$ value ($(397 \pm 15)\,A\,g_{Pt}^{-1}$) of $PtCe_{Na}$-1 was much higher than that ($(237 \pm 24)\,A\,g_{Pt}^{-1}$) of $PtCe_{NaOH}$ measured at $0.01\,V\,s^{-1}$ (Figure 38b). The stability against the MOR intermediate poisoning of the $PtCe_{Na}$-1 is better than that of the $PtCe_{NaOH}$ material as the $i_{CA\ at\ 0.50\ V}$ value for the $PtCe_{Na}$-1 and $PtCe_{NaOH}$ materials are 0.67 and $0.44\,A\,g_{Pt}^{-1}$, respectively (Table 15).

6.3.2 Influence of Ageing Catalyst Suspension on MOR Activity

The ageing effect of the catalyst suspension was investigated by preparing the electrode using a two-week aged catalyst suspension. The comparison of the electrochemical activity of electrodes prepared from fresh and two-week aged

Table 15. Methanol oxidation reduction results at different catalysts.

Material	$i_{\text{ap, CV}}$ / $\text{A g}_{\text{Pt}}^{-1}$	$i_{\text{CA at 0.85 V}}$ / $\text{A g}_{\text{Pt}}^{-1}$	$i_{\text{CA at 0.50 V}}$ / $\text{A g}_{\text{Pt}}^{-1}$	$\frac{i_{\text{CA at 0.5 V}}}{i_{\text{ap, CV}}}$
$PtCe_{NaOH}$	–[a]	–	0.44±0.02	–
$PtCe_{Na}$-1	457±25[a]	182±8	0.67±0.07	0.40
$PtCe_{Na}$-2	–[a]	–	0.45±0.03	–
$PtCe_{chl}$-1	403±11	141±8	0.60±0.08	0.34
$PtCe_{chl}$-2	457±11	140±14	0.80±0.02	0.30
$PtCe_{chl}$-3	354±43	105±3	0.63±0.05	0.30
$PtCe_{chl}$-4	446±29	162±5	0.73±0.06	0.36
$PtCe_{H_2O_2}$	190	37	0.16	0.2
$PtCe_{H_3PO_4}$	477±22	178±3	0.79±0.01	0.37
$PtCe_{sul}$-1	516±30	200±10	0.77±0.09	0.39
$PtCe_{sul}$-2	415±44	188±27	0.58±0.13	0.45
$PtCe_{sul}$-3	419±1	159±3	0.68±0.01	0.38
$PtCe_{sul}$-4	579±39	193±22	0.86±0.09	0.33
$PtCe_{sul}$-5	543±24	201±16	0.76±0.05	0.37
$PtC(KB)_{com}$	346±45	109±1	0.48±0.13	0.32
PtC(KB)	434±11	135±8	0.66±0.01	0.31
$PtC(Cr_3C_2)$	476±19	216±17	0.66±0.01	0.45
$PtCe_{chl}$-1_H_2	482	191	0.89	0.39
$PtCe_{chl}$-2_H_2	440±5	144±16	0.90±0.08	0.33
$PtCe_{H_3PO_4}$_H_2	351	122	0.71	0.35

$i_{\text{ap, CV}}$ is the mass activity for MOR. In this table, this value was measured at 50 mV s^{-1}.

$i_{\text{CA at 0.85 V}}$ is the mass activity for MOR, which was measured by chronoamperometry at the potential 0.85 V

$i_{\text{CA at 0.50 V}}$ is the mass activity for MOR, which was measured by chronoamperometry at the potential 0.50 V

[a]The $i_{\text{ap, CV}}$ values, which were measured in CV measurement at scan rate 10 mV s^{-1}, were 237 ± 24, 397 ± 15 and $323 \pm 19\ \text{A g}_{\text{Pt}}^{-1}$ for the $PtCe_{NaOH}$, $PtCe_{Na}$-1 and 2 materials, respectively.

suspension of the $PtCe_{sul}$-4 material is plotted in the Figure 39.

Although the capacitance vs potential curves in the region of the hydrogen adsorption and desorption (in the potential region from 0.06 to 0.35 V) are similar, the difference in the capacitance vs potential curve in the EDL potential region can be caused by the changes of (surface) structure of carbon support. The $i_{ap,\,CV}$, $i_{CA\ at\ 0.85\ V}$ and $i_{CA\ at\ 0.50\ V}$ values for electrodes prepared from fresh catalyst suspension (606 ± 6, 209 ± 2 and $0.92 \pm 0.01\,A\,g_{Pt}^{-1}$, respectively) are slightly higher than for electrodes prepared from two-week aged catalyst suspension (516 ± 7, 160 ± 2 and $0.71 \pm 0.02\,A\,g_{Pt}^{-1}$). Therefore, the MOR activity is obviously higher for electrodes prepared from fresh catalyst

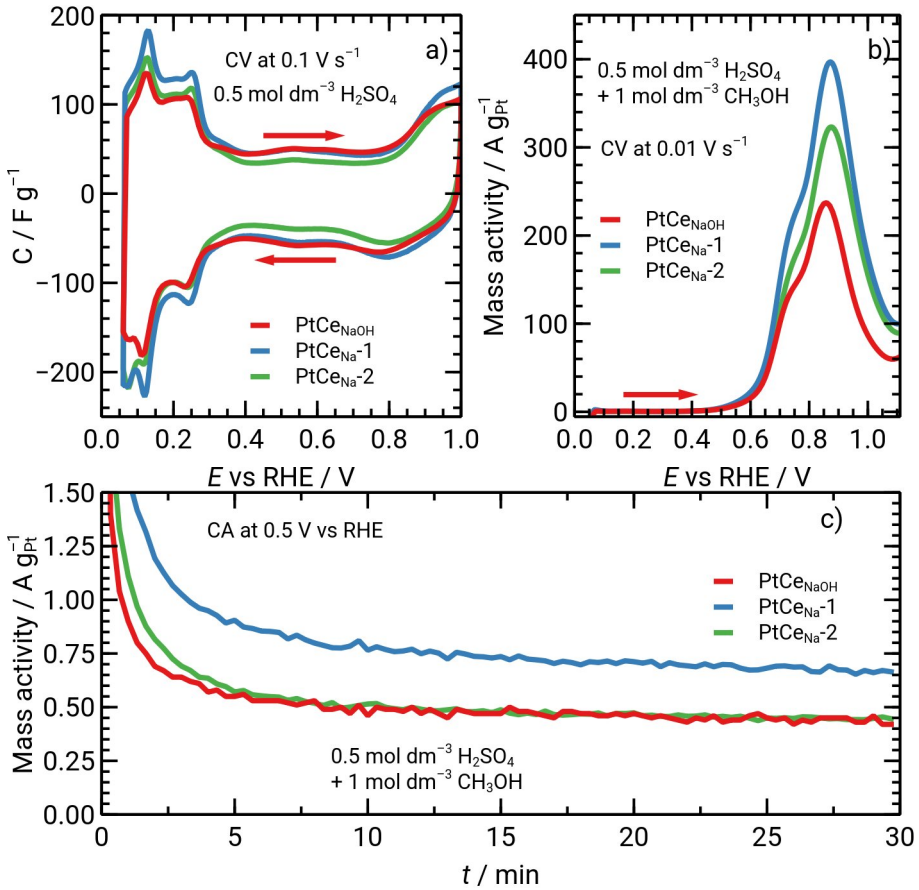

Figure 38. (a) The gravimetric capacitance vs potential curves for selected materials, noted in the figure, in a $0.5\,mol\,dm^{-3}$ H_2SO_4 electrolyte solution saturated with argon. The methanol oxidation reaction activity of selected materials in a mixture of $0.5\,mol\,dm^{-3}$ H_2SO_4 and $1\,mol\,dm^{-3}$ CH_3OH is illustrated using (b) cyclic voltammetry results at the scan rate $50\,mV\,s^{-1}$ and (c) chronoamperometry at 0.5 V vs RHE.

suspension. As the isopropanol solution was used to prepare the catalyst suspension, the adsorption of isopropanol at the catalyst surface also generates CO_{ads} poisoning over the ageing duration. The lack of Pt sites due to the occupation of CO_{ads} results in the drop of MOR activity and gravimetric capacitance.

6.3.3 Influence of Hydrogen Post-Treatment on MOR Activity of Catalysts

Three different materials were selected to study the influence of the hydrogen post-treatment on the MOR activity. It was established that the characteristics of the Pt NPs changes after the hydrogen post-treatment, which is discussed in Chapter 6.1.3. In the case of the $PtCe_{chl}$-1 material, for which the solvothermal

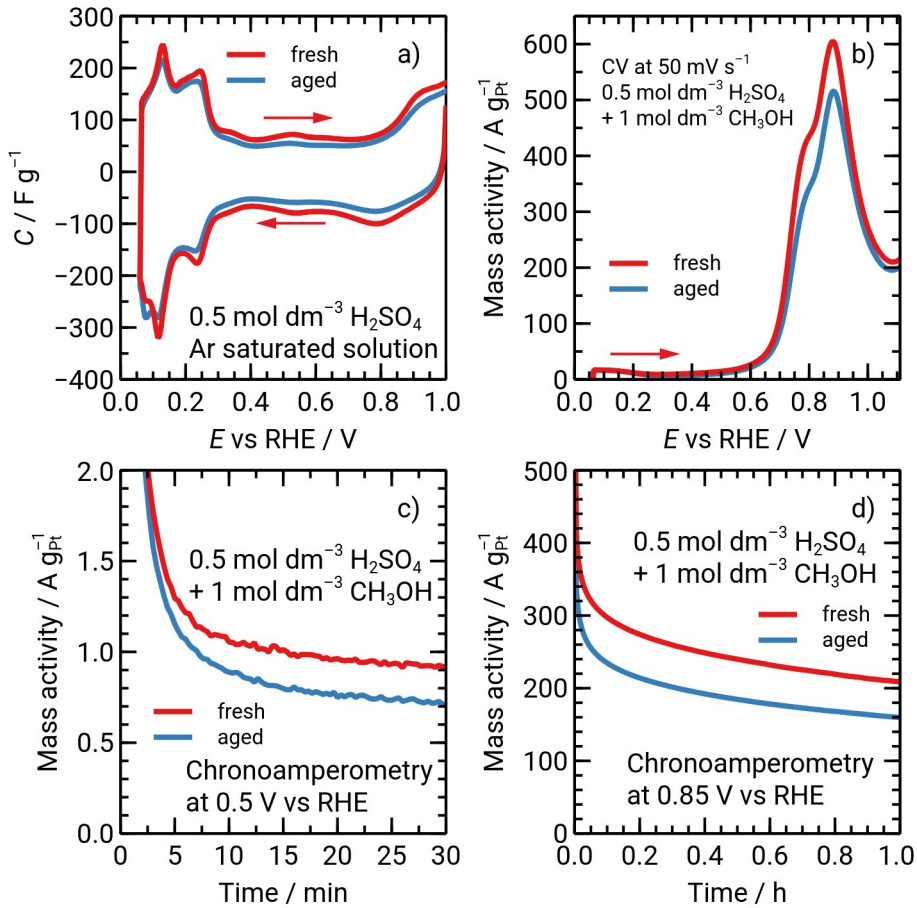

Figure 39. Changes in electrochemical behaviour ((a) capacitive behaviour and (b–d) methanol oxidation reaction activity) of electrodes made from fresh and two-week aged suspension of $PtCe_{sul}$-4 catalyst.

synthesis method was used to prepare CeO_2 NPs, the MOR activity and stability against the MOR intermediate is enhanced after the hydrogen post-treatment, i.e. after the hydrogen post-treatment, the $i_{ap,\,CV}$, $i_{CA\ at\ 0.85\ V}$ and $i_{CA\ at\ 0.50\ V}$ values increase from 403 ± 11, 141 ± 8 and $0.60 \pm 0.08\,A\,g_{Pt}^{-1}$ to 482, 191 and $0.89\,A\,g_{Pt}^{-1}$, respectively. Thus, the $PtCe_{chl}$-1_H_2 material with the synthesis parameters discussed in the Chapter 5.1.3 has higher than the $PtCe_{chl}$-1 material (Table 15). According to the $i_{ap,\,CV}$ value, there is no significant difference in the MOR activity for the $PtCe_{chl}$-2 and $PtCe_{chl}$-2_H_2, for which the sonochemical method was used to prepare the CeO_2 NPs (Figure 40). However, the stability in short-term duration of the $PtCe_{chl}$-2 was improved slightly after the hydrogen post-treatment as the $i_{CA\ at\ 0.50\ V}$ value for the $PtCe_{chl}$-2_H_2 material ($(0.90 \pm 0.08)\,A\,g_{Pt}^{-1}$) was higher than that of the $PtCe_{chl}$-2 material ($(0.80 \pm 0.02)\,A\,g_{Pt}^{-1}$). On the other hand, the hydrogen post-treatment has the opposite effect on the MOR activity and stability for the $PtCe_{H_3PO_4}$ material, for which phosphoric acid was used to deposit the Pt NPs and CeO_2 synthesis was the same as for material $PtCe_{chl}$-2_H_2. The MOR activity and stability of the $PtCe_{H_3PO_4}$ is decreased after the hydrogen post-treatment as all the MOR activity parameters of the $PtCe_{H_3PO_4}$_H_2 given in the Table 15 and Figure 40 were lower. For instances, the $i_{ap,\,CV}$, $i_{CA\ at\ 0.85\ V}$, $i_{CA\ at\ 0.50\ V}$ drop from 477 ± 22, 178 ± 3 and $0.80\,A\,g_{Pt}^{-1}$ to 351, 122 and $0.71\,A\,g_{Pt}^{-1}$, respectively.

In the case of $PtCe_{chl}$-1 material, the post-treatment seems to have high the wt% of metallic Pt and Ce on the catalyst surface as in the case of $Pt{-}RuO_x/C$ synthesised by Wei *et al.* [159], the wt% of metallic Pt remains high and wt% of metallic Ru increases after the hydrogen treatment. This reason explained the increase of the MOR activity of the $PtCe_{chl}$-1 material. In the case of $PtCe_{H_3PO_4}$ material, the presence of CeO_2 and $CePO_4$ phases in the case of $PtCe_{H_3PO_4}$_H_2 material was as for the phases in $PtCe_{H_3PO_4}$ (see Figure 28). It seems that the synergistic effect caused by the fluorite structure of this material was eliminated. The $PtCe_{chl}$-2_H_2 material was treated at a lower temperature compared to the treatment temperature of the $PtCe_{chl}$-1_H_2 material to avoid ECSA decrease caused by the hydrogen post-treatment. However, during the hydrogen post-treatment at a lower temperature, the formation of metallic Pt of the $PtCe_{chl}$-2 catalyst was not probably initiated.

6.3.4 Influences of Heating Method During The Synthesis on MOR Activity of Catalysts

The $PtCe_{chl}$-2 and $PtCe_{chl}$-3 catalysts were used to compare the influence of longer refluxing duration on MOR activity (Figure 44). The $[PtCl_6]^{2-}$ concentration in the synthesis solution, $c_{Pt(IV)}$, for the $PtCe_{chl}$-3 was two times lower compared to that for the $PtCe_{chl}$-2 (Table 7). The lower $c_{Pt(IV)}$ value usually results in the smaller $d_{Pt,\,XRD}$ (Table 12). However, the $PtCe_{chl}$-3 has

lower ECSA value ($(77 \pm 4)\ m^2_{Pt}\ g^{-1}_{Pt}$) compared with the ECSA value calculated for the $PtCe_{chl}$-2 ($(91 \pm 7)\ m^2_{Pt}\ g^{-1}_{Pt}$). This result indicates that the Pt NPs of the $PtCe_{chl}$-3 material are not dispersed as well as for the $PtCe_{chl}$-2 material. Therefore, the MOR activity and the tolerance against intermediate poisoning of $PtCe_{chl}$-2 material in CA measurements are higher than that of the $PtCe_{chl}$-3 material, i.e. the $i_{ap,\,CV}$, $i_{CA\ at\ 0.85\ V}$, and $i_{CA\ at\ 0.50\ V}$ values of $PtCe_{chl}$-2 material are 457 ± 11, 140 ± 14 and $0.80 \pm 0.02\ A\ g^{-1}_{Pt}$, respectively, compared to the same parameters of the $PtCe_{chl}$-3 material (354 ± 43, 105 ± 3 and $0.63 \pm 0.05\ A\ g^{-1}_{Pt}$, respectively). This phenomenon is also observed in the case of the $PtCe_{chl}$-4 material. The same $c_{Pt(IV)}$ and refluxing duration values for the $PtCe_{chl}$-2 and $PtCe_{chl}$-4 materials (data in the Table 7) result in the same MOR activity demonstrated in the Table 15 and Figure 44. Obviously, the longer refluxing

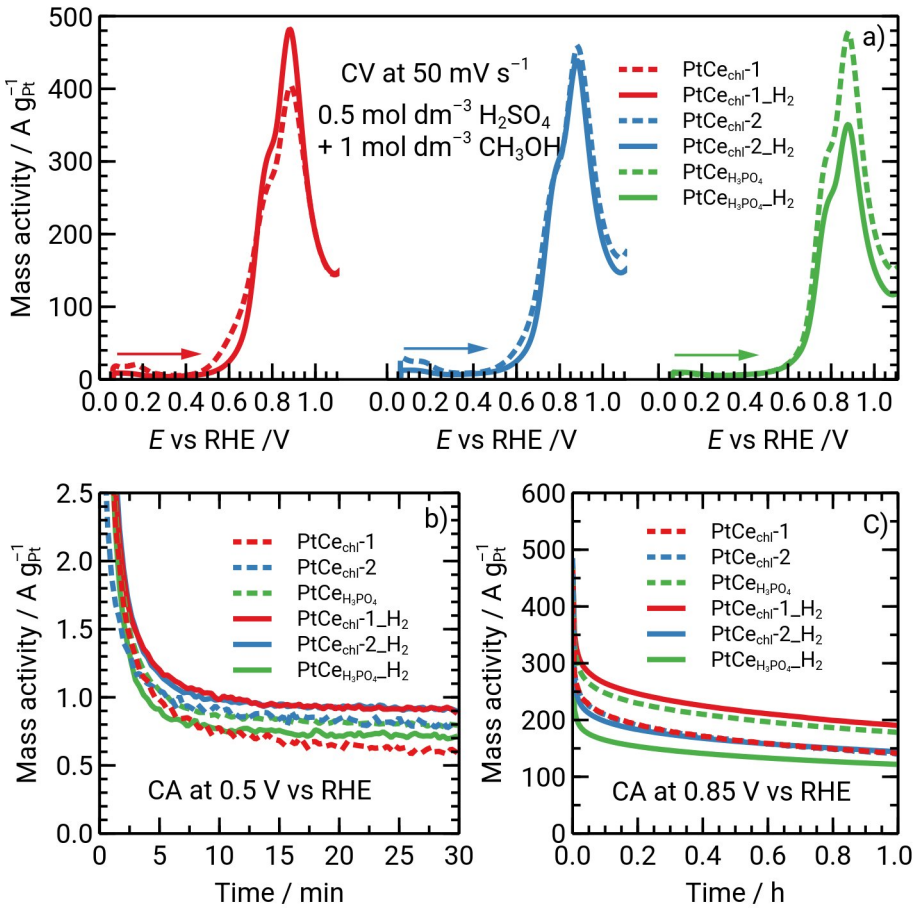

Figure 40. The methanol oxidation reaction activity of selected materials in a mixture of 0.5 mol dm^{-3} H_2SO_4 and 1 mol dm^{-3} H_2SO_4 after the hydrogen post-treatment. For materials post-treated with hydrogen, H_2 is added to the end of the material name.

duration results in the Pt NPs agglomeration and the reduction of the electrochemical activity of the Pt−CeO_2/C materials.

The longer ultrasound treatment influences both the capacitance in the EDL potential region and MOR activity. The capacitance value calculated for the $PtCe_{Na}$-2 material in the EDL potential region is smaller than for the $PtCe_{Na}$-1 material (Figure 38). This result indicates that some of the carbon pores are not accessible to the electrolyte because they are clogged with Pt (or CeO2) NPs. This might also explain 10% lower ECSA value for PtCeNa-2 material. The maximum MOR activity of the $PtCe_{Na}$-1 material is higher than that of the $PtCe_{Na}$-2 material as the $i_{ap,\,CV}$ values for the $PtCe_{Na}$-1 and $PtCe_{Na}$-2 are 397 ± 15 and $323 \pm 19\,A\,g_{Pt}^{-1}$, respectively. The stability of the $PtCe_{Na}$-1 material against the MOR intermediate poisoning is higher than that of the $PtCe_{Na}$-2 material as demonstrated in Figure 38. This difference may be caused by the slightly difference in the porosity (Table 10) and higher degree of the Pt agglomeration of the $PtCe_{Na}$-2 material.

6.3.5 Influence of the Sedimentation Method on MOR Activity of Catalysts

If the combination of heating methods was used for the EG reduction synthesis of Pt NPs, the $PtCe_{Na}$-1 was the most MOR active material compared to the $PtCe_{NaOH}$ and $PtCe_{Na}$-2 catalysts. This comparison was discussed in Chapter 6.3.1. Therefore, the comparison between the $PtCe_{Na}$-1 and $PtCe_{chl}$-1 materials is suitable to demonstrate the role of Pt deposition methods on the catalyst activities. The MOR parameters of the $PtCe_{Na}$-1 material (457 ± 25, 182 ± 8 and $0.67 \pm 0.07\,A\,g_{Pt}^{-1}$) are higher than for the $PtCe_{chl}$-1 material (403 ± 11, 141 ± 8 and $0.60 \pm 0.08\,A\,g_{Pt}^{-1}$), although the $d_{Pt,\,XRD}$ and ECSA values of the $PtCe_{chl}$-1 material (1.5 nm and $(72 \pm 7)\,A\,g_{Pt}^{-1}$, respectively) were more optimal compared to these parameters of the $PtCe_{Na}$-1 material (3.0 nm and $(55 \pm 3)\,A\,g_{Pt}^{-1}$, respectively). These catalysts have the same high crystalline flower-shaped CeO_2 particles. The only explanation for this phenomenon can be the $PtCe_{Na}$-1 had a higher percentage of metallic Pt [42] compared to that of $PtCe_{chl}$-1 material, and the Pt PSD of the $PtCe_{Na}$-1 is more uniform with the smaller uncertainty of $d_{Pt,\,microscopy}$ value ((4.2 ± 1.4) nm) compared to the Pt PSD of $PtCe_{chl}$-1 with $d_{Pt,\,microscopy}$ value of (4.4 ± 3.1) nm. As the Pt^0 is electrochemically more active than Pt^{2+} and Pt^{4+}, the higher amount of Pt^0 increases the MOR electrocatalytic activity of the catalyst material [42].

In the case of the $PtCe_{H_2O_2}$ material, the heavy agglomeration of Pt NPs due to the use of H_2O_2 for the deposition of Pt NPs is the reason for very low MOR activity and stability of the $PtCe_{H_2O_2}$ material, demonstrated in the Figure 41 and discussed in the Chapter 6.1.3. The $PtCe_{sul}$-1 material is selected to compare with the $PtCe_{H_3PO_4}$ material for these catalysts, as both materials were

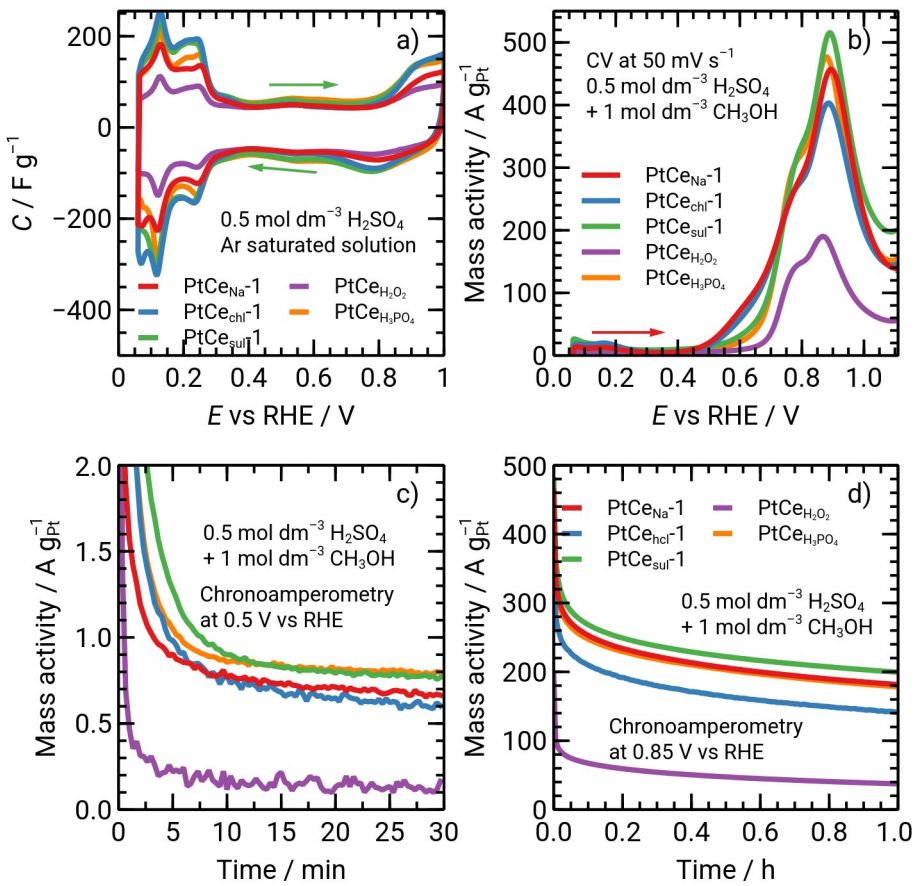

Figure 41. (a) The capacitive behaviour and (b–d) the methanol oxidation reaction activity for catalyst materials synthesised using different Pt deposition methods.

synthesised by the two-step method (see the Table 7). The use of H_3PO_4 solution for Pt deposition of the $PtCe_{H_3PO_4}$ material instead of using H_2SO_4 solution caused the differences in physical characteristics that were discussed in the Chapter 6.1.3, and the difference in the c_{NaOH} of the sonochemical method for the CeO_2/C_{ultr}-2 and CeO_2/C_{ultr} substrates, which were used to synthesise $PtCe_{sul}$-1 and $PtCe_{H_3PO_4}$ materials, respectively, does not affect the characteristics of the CeO_2 NPs, demonstrated in the Table 11. Both $PtCe_{H_3PO_4}$ and $PtCe_{sul}$-1 have small $d_{Pt,\,XRD}$ values (1.4 and 1.1 nm, respectively, given in the Table 13), but some Pt NPs of $PtCe_{H_3PO_4}$ is probably blocked by the $CePO_4$. This explained the smaller ECSA value for the $PtCe_{H_3PO_4}$ ($(56 \pm 3)\,m^2_{Pt}\,g^{-1}_{Pt}$) compared to that value of the $PtCe_{sul}$-1 material ($(88 \pm 5)\,m^2_{Pt}\,g^{-1}_{Pt}$), given in the Table 12. Although the MOR activity for the $PtCe_{H_3PO_4}$ material is high ($i_{ap,\,CV} = (477 \pm 22)\,A\,g^{-1}_{Pt}$, $i_{CA\ at\ 0.85\ V} = (178 \pm 3)\,A\,g^{-1}_{Pt}$, and $i_{CA\ at\ 0.50\ V} = (0.79 \pm 0.01)\,A\,g^{-1}_{Pt}$), the slightly higher MOR activity of $PtCe_{sul}$-1 material (516 ± 30, 200 ± 10 and $77 \pm 9\,A\,g^{-1}_{Pt}$, respectively) is observed.

Thus, the MOR activity and stability against intermediate poisoning of the studied catalysts decreased in the order of the Pt deposition methods: a combination of various heating methods > adjusting pH value ($HCl = H_2SO_4 > H_3PO_4 > H_2O_2$). The use H_2O_2 for Pt deposition results in low MOR activity, although it is possible to deposit all Pt NPs. Probably, the use H_2O_2 for the $Pt{-}CeO_2/C$ synthesis might work. However, this method requires rigorous optimization.

6.3.6 Influence of CeO_2 on MOR Activity of Catalysts

For the $PtCe_{chl}$-1 and PtC(KB) materials, in which the deposition of Pt NPs was achieved by adjusting the pH of the reaction solution, there are no significant differences in the MOR activity and in the stability, as given in the Figure 42 and in the Table 15. The $i_{ap,\,CV}$, $i_{CA\ at\ 0.85\ V}$, and $i_{CA\ at\ 0.50\ V}$ values of $PtCe_{chl}$-1 material (403 ± 11, 141 ± 8 and $0.60 \pm 0.08\,A\,g^{-1}_{Pt}$, respectively) are close to the same parameters of the PtC(KB) (434 ± 11, 135 ± 8 and $0.66 \pm 0.01\,A\,g^{-1}_{Pt}$, respectively). This observation is unexpected as the mass percentage of CeO_2 in the $PtCe_{chl}$-1 is high (ca. 10 wt%), and the gravimetric capacitance is the same for both materials in the EDL potential region. According to the MOR mechanism discussion in the Chapter 4.1.4, many steps in the MOR require the $OH_{(ads)}$ formation (Equation 4.51), especially the oxidation of $CO_{(ads)}$ to CO_2 (Equation 4.52), which is determining the total activity of catalysts. This step takes place on the adjacent Pt and CeO_2 surfaces. Therefore, with the large flower-shaped CeO_2 particles (ca. 0.8 µm) at the $PtCe_{chl}$-1 surface, the number of the adjacent surface of Pt and CeO_2 NPs is insignificant. The $CO_{(ads)}$ removal from these catalysts proceeded mainly at the junctions of $Pt{-}OH_{(ads)}$ and $Pt{-}CO_{(ads)}$ surfaces (Equation 4.50 and 4.45).

The small CeO_2 NPs on the surfaces of $PtCe_{sul}$-2 (CeO_2 synthesised by the

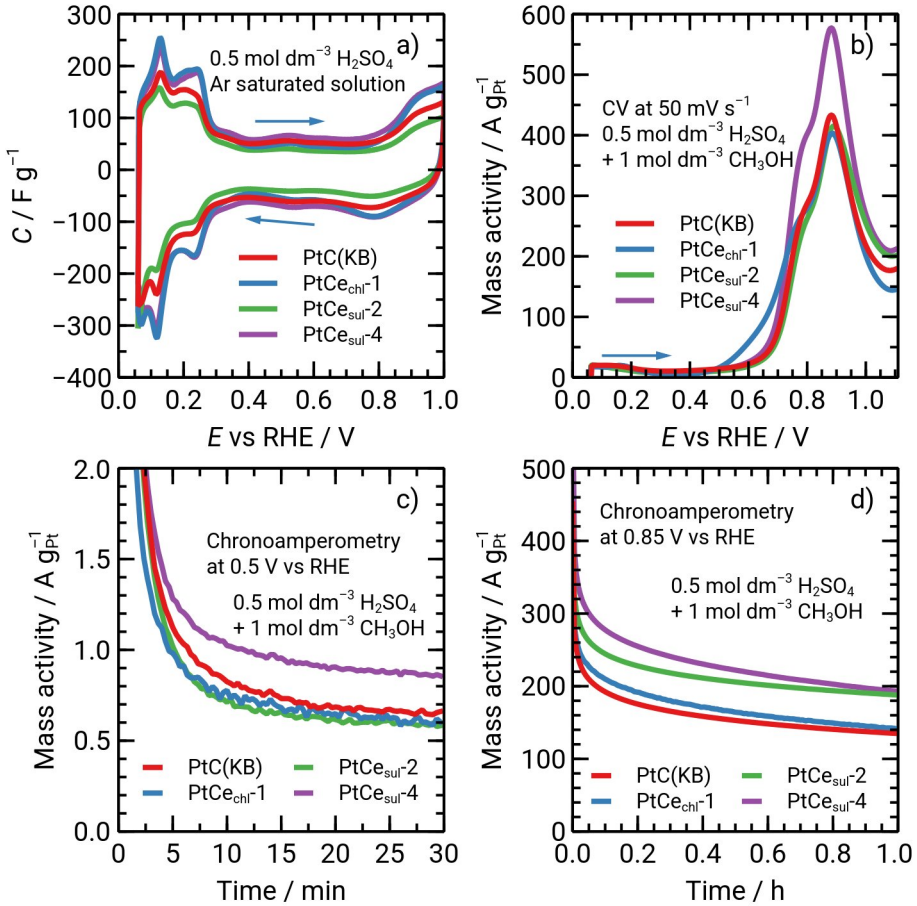

Figure 42. (a) The capacitive behaviour, and (b–d) the methanol oxidation reaction activity for synthesised Pt−CeO_2/C catalysts with different types of CeO_2 nanoparticles.

sonochemical method) and $PtCe_{sul}$-4 (CeO_2 synthesised by the microwave method) catalysts increase the number of adjacent Pt and CeO_2 NPs and improve the MOR activity of these Pt−CeO_2/C materials. The $PtCe_{sul}$-4 has much higher MOR activity ($(579 \pm 39)\,A\,g_{Pt}^{-1}$) and stability against the intermediate poisoning at low potential of 0.5 V ($(0.86 \pm 0.09)\,A\,g_{Pt}^{-1}$) compared to that of the $PtCe_{chl}$-1 (403 ± 11 and $0.60 \pm 0.08\,A\,g_{Pt}^{-1}$, respectively) and $PtCe_{sul}$-2 (415 ± 44 and $0.58 \pm 0.13\,A\,g_{Pt}^{-1}$, respectively) materials, as shown in the Figure 42b and c. However, the MOR mass activity at high MOR rate (at 0.85 V) observed for $PtCe_{sul}$-2 and $PtCe_{sul}$-4 is the same at the end of the CA measurements (Figure 42d). The ratio of $i_{CA\ at\ 0.85\ V}$ and $i_{ap,\,CV}$ values, which is noted as $i_{CA\ at\ 0.85\ V}/i_{ap,\,CV}$ and given in the Table 15, indicates the stability for the catalyst material at the intensively working condition. The higher $i_{CA\ at\ 0.85\ V}/i_{ap,\,CV}$ value of the $PtCe_{sul}$-2 material (0.45) revealed that the

$PtCe_{sul}$-2 was more stable compared to the $PtCe_{sul}$-4 material (0.33). According to the CeO_2 wt% given in the Table 12, the CeO_2 wt% of the $PtCe_{sul}$-2 material (0.3 wt%) is insignificant compared to that of $PtCe_{sul}$-4 material (5.1 wt%). As the morphology of CeO_2 NPs synthesised by sonochemical and microwave methods is the same (discussed in the subsection 6.1.2), the $PtCe_{sul}$-2 material with lower CeO_2 content has better stability. This phenomenon can also be observed when comparing the $i_{CA\ at\ 0.85\ V}/i_{ap,\ CV}$ values of $PtCe_{sul}$-1 and$PtCe_{sul}$-3 materials (0.39 and 0.38) to the $i_{CA\ at\ 0.85\ V}/i_{ap,\ CV}$ value of $PtCe_{sul}$-4 material (0.33). To explain the stability of catalysts, the CO stripping was conducted. The ECSA values measured before and after CO stripping measurements reveal the ability of catalysts towards CO removal from the Pt surface (Figure 43). Comparing the $PtCe_{sul}$-1 and the $PtCe_{sul}$-4 materials, the ECSA value of the $PtCe_{sul}$-1 material reduces lesser (-6%) compared to -18% in the case of the $PtCe_{sul}$-4 material. However, the ECSA value of PtC(KB) material reduces significantly (-13%). Thus, in the C(KB) regime, the presence of CeO_2 is necessary to have a good ability towards CO removal from Pt surface. However, high CeO_2 content may result in a worse ability to remove CO.

The influence of the CeO_2 content of the $Pt-CeO_2/C$ materials for the MOR

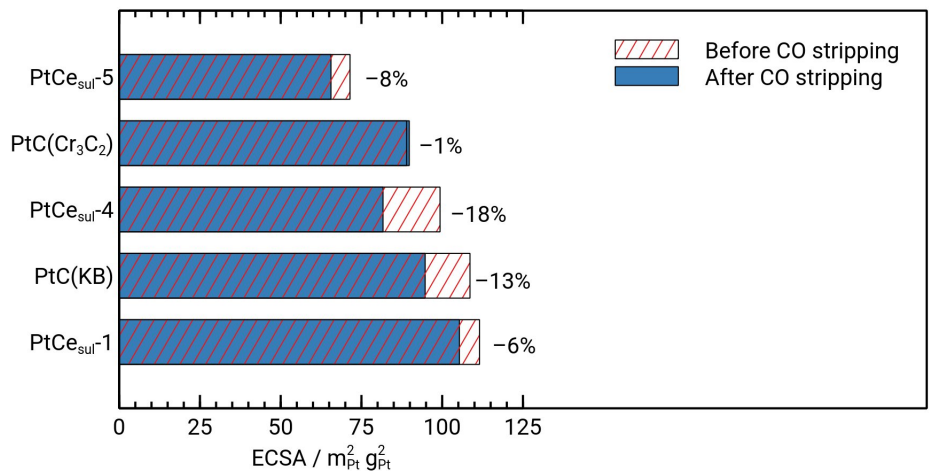

Figure 43. The electrochemically active surface area of Pt nanoparticles estimated from cyclic voltammetry data in $0.1\,mol\,dm^{-3}$ $HClO_4$ before and after the CO stripping measurements.

activity is visible if the MOR activity of $PtCe_{sul}$-3 and $PtCe_{sul}$-4 materials is compared, as demonstrated in the Figure 44. The CeO_2 NPs for both materials were synthesised using the microwave radiation method and CeO_2 was co-deposited at the same time with Pt NPs onto the carbon support. Nonetheless, the higher CeO_2 content of $PtCe_{sul}$-4 slightly enhances all the parameters for the MOR activity such as $i_{ap,\ CV}$, $i_{CA\ at\ 0.50\ V}$, and $i_{CA\ at\ 0.85\ V}$ values (from 419 ± 1, 159 ± 3 and $0.68 \pm 0.01\,A\,g_{Pt}^{-1}$, respectively to 579 ± 39, 193 ± 22 and $0.86 \pm 0.09\,A\,g_{Pt}^{-1}$). This agreed well with the hypothesis that the number of Pt

and CeO_2 adjacent particles increases along with the CeO_2 content. Nevertheless, too high CeO_2 content in the Pt−CeO_2/C can have lower the MOR [42, 48]

The influence of the CeO_2 synthesis and deposition methods on the MOR

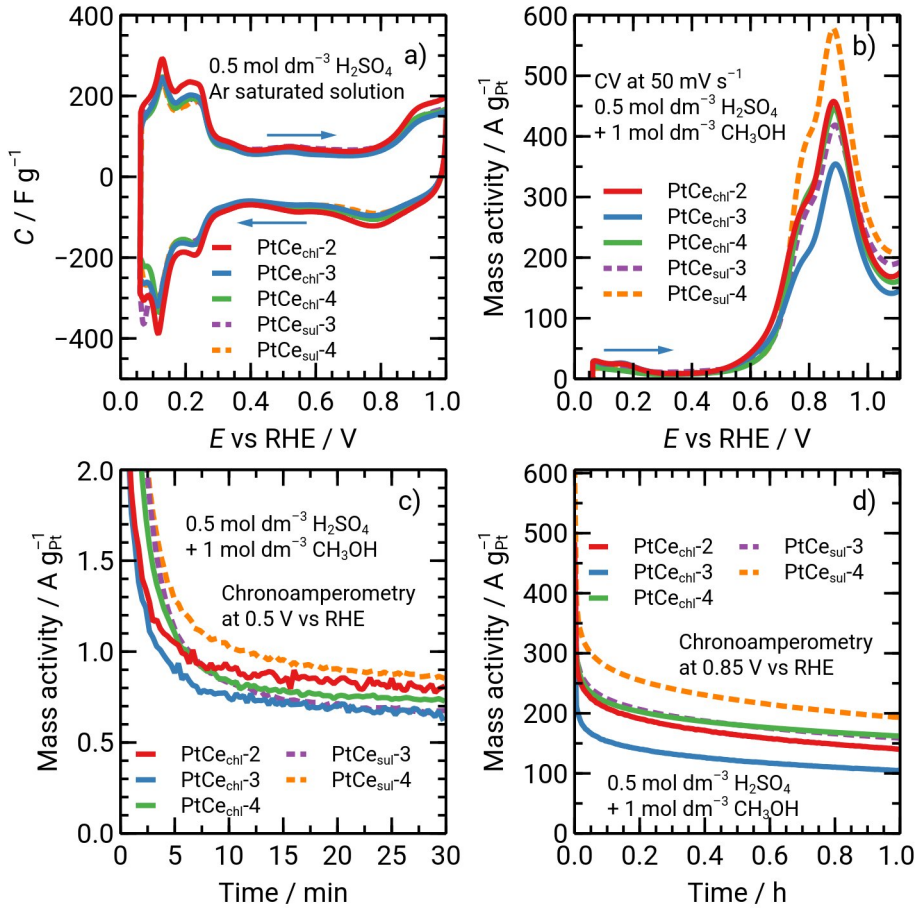

Figure 44. (a) The capacitive behaviour and (b–d) the methanol oxidation reaction data for synthesised catalyst materials with various content of CeO_2.

activity is not observed if the PtCe$_{sul}$-1 (two-step method), PtCe$_{sul}$-2 (sonochemical method, and co-precipitation) and PtCe$_{sul}$-4 (microwave method, and co-precipitation) catalysts are compared. The MOR activity of these materials are very similar (as in the Table 15).

6.3.7 Influence of Sodium Hydroxide Concentration in Synthesis Mixture on MOR Activity of Catalysts

The influence of sodium hydroxide concentration, which can be considered as the concentration of sodium ions and noted as c_{Na^+}, in the synthesis mixture during the EG reduction method has been studied by many researchers [64, 76,

160]. There is a correlation between the c_{Na^+} and the $d_{Pt,\,XRD}$ values, however, this influence always depends on the specific synthesis condition. The increase of c_{Na^+} in the synthesis mixture in the synthesis where microwave radiation or the refluxing method were used at high temperature ($> 160\,^{\circ}C$) reduces the $d_{Pt,\,XRD}$ value [64, 143]. However, at relative low temperature ($< 140\,^{\circ}C$), if the c_{Na^+} value is high enough in the synthesis mixture using the refluxing method, there is no observation for the difference in $d_{Pt,\,XRD}$ value [76]. In the study of Quinson *et al.* [76], the c_{Na^+} value was controlled by the NaOH/Pt ratio, and the $d_{Pt,\,XRD}$ was small and constant if the NaOH/Pt ratio was above ten. If the refluxing system for the Pt NPs synthesis was used in this study, NaOH/Pt in the synthesis mixture is higher than 10. Therefore, the c_{Na^+}in this study is sufficient to have a good dispersion of Pt NPs.

In this study, the c_{Na^+} value for the synthesis of the $PtCe_{chl}$-4 material was three times higher than that for the synthesis of the $PtCe_{chl}$-2 material (Table 7). However, the physico-chemical characteristics of these two materials are deviated slightly (data in the Tables 12 and 13), i.e. the $d_{Pt,\,XRD}$ and ECSA values of the $PtCe_{chl}$-2 and $PtCe_{chl}$-4 catalysts are 1.1 and 1.4 nm, and, 91 ± 7 and $72 \pm 1\,m^2_{Pt}\,g^{-1}_{Pt}$, respectively. Thus, this result is different from the conclusions made by Quinson *et al.* [143] because two parameters were controlled at the same time in this study, and high c_{Na^+} value can affect the physical characteristics [76]. Nevertheless, the MOR activity and stability to the MOR intermediate poisoning of the $PtCe_{chl}$-2 and $PtCe_{chl}$-4 materials are in the same range as shown in the Figure 44 and Table 15, the $i_{ap,\,CV}$, $i_{CA\ at\ 0.85\ V}$, and $i_{CA\ at\ 0.50\ V}$ values are 457 ± 11, 140 ± 14 and $0.80 \pm 0.02\,A\,g^{-1}_{Pt}$, respectively for the $PtCe_{chl}$-2, and are 446 ± 29, 162 ± 5 and $0.73 \pm 0.06\,A\,g^{-1}_{Pt}$. The two times

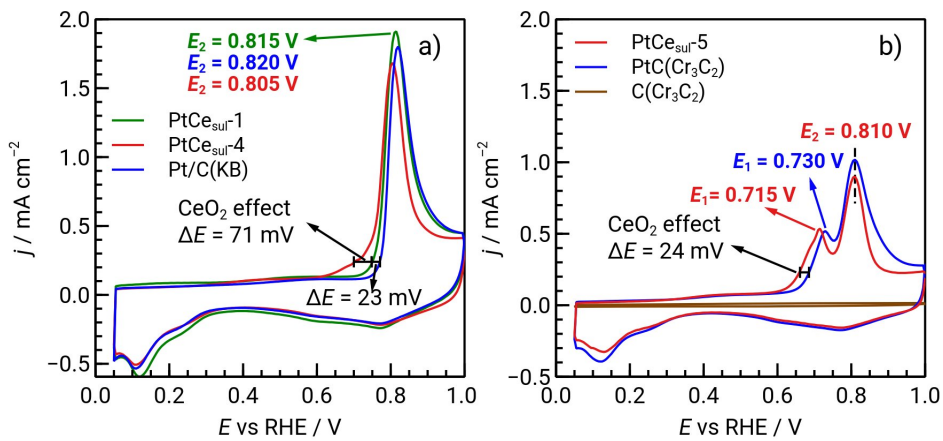

Figure 45. The CO stripping voltammograms of C(KB)-based (a) and $C(Cr_3C_2)$-based (b) catalysts in 0.1 mol dm^{-3} $HClO_4$ saturated with CO before the stripping while the argon gas is flowing above the solution (20 mV s^{-1}).

lower $c_{Pt(IV)}$ value (Table 7) for the $PtCe_{chl}$-4 catalyst affects the physico-chemical characteristics of catalysts. Therefore, the MOR activity is not influenced by the $c_{Pt(IV)}$ and c_{Na^+} values if the $PtCe_{chl}$-4 material is compared with the $PtCe_{chl}$-2 material (data in Table 12 and 15).

6.3.8 Influence of Chromium Carbide-Derived Carbon Support on MOR Activity of Catalysts

The influence of carbon support material on the MOR activity was investigated for both Pt-based and $Pt-CeO_2$-based materials and the results are shown in the Figure 46. In case of PtC materials, there is slight or no significant difference in $i_{ap,\,CV}$ and $i_{CA\ at\ 0.50\ V}$ values for the PtC(KB) and $PtC(Cr_3C_2)$ materials, i.e. the $i_{ap,\,CV}$ values are 434 ± 11 and $476 \pm 19\,A\,g_{Pt}^{-1}$, and $i_{CA\ at\ 0.50\ V}$ values are $(0.66 \pm 0.01)\,A\,g_{Pt}^{-1}$ for the PtC(KB) and $PtC(Cr_3C_2)$ materials, respectively. However, the $i_{CA\ at\ 0.85\ V}$ value for the $PtC(Cr_3C_2)$ material ($(216 \pm 17)\,A\,g_{Pt}^{-1}$) is much higher than that for the PtC(KB) material ($(135 \pm 8)\,A\,g_{Pt}^{-1}$). The same phenomenon can be also observed for the $PtCe_{sul}$-4 material (deposited C(KB) carbon support material) and $PtCe_{sul}$-5 (deposited on the $C(Cr_3C_2, 900)$ carbon support material). However, the catalytic differences between two $PtCe_{sul}$ materials (579 ± 39, 193 ± 22 and $0.86 \pm 0.09\,A\,g_{Pt}^{-1}$ for the $PtCe_{sul}$-4 material, and 543 ± 24, 201 ± 16 and $0.76 \pm 0.05\,A\,g_{Pt}^{-1}$ for the $PtCe_{sul}$-5 material) were small compared to that established for PtC materials (Table 15). Thus, the $C(Cr_3C_2, 900)$ support material enhanced the MOR activity and the enhancement effect is stronger without the presence of the CeO_2. Besides, the optimal content of CeO_2 in the $Pt-CeO_2$/C catalysts established in other studies was varied from 10 to 40 wt% for different investigated reactions [19, 42, 161].

The stable MOR activity of the $PtC(Cr_3C_2)$ material at high MOR rate (0.85 V) was even higher than value for the $PtCe_{sul}$-5 catalyst material. The similar effect has been observed in the study of Huang *et al.* [162], where the CA current of Pt/C(reduced graphene oxide) at 0.60 V in the solution of $1\,mol\,dm^{-3}$ KOH and $1\,mol\,dm^{-3}$ CH_3OH is as stable as in the case of 20 wt% PtRu/C(commercial) although the CA current is much lower. The possible reason for this phenomenon was that the active site at the carbon surface can provide the $OH_{(ads)}$ for $CO_{(ads)}$ oxidation. Unfortunately, in the study of Zhang and Shen [163], the CA current of $Pt-CeO_2$/C(reduced graphene oxide) at 0.85 V in the solution of $1\,mol\,dm^{-3}$ H_2SO_4 and $1\,mol\,dm^{-3}$ CH_3OH solutions drops quite faster within 1200 s. This type of carbon effect has not been observed on the C(KB) support material because the $C(Cr_3C_2, 900)$ contains some nanocrystalline graphite particles and trace amount of chromium while the C(KB) does not have.

To explain observation from the MOR activity of studied catalysts on both C(KB) and $C(Cr_3C_2, 900)$ regimes, the CO stripping results are helpful

(Figure 45). The CO stripping peak of C(Cr_3C_2, 900) splits into two peaks at potential E_1 (from 0.715 to 0.730 V) and E_2 (at 0.810 V). The CO oxidation charge under the first peak E_1 is 40% and 24% of the total charges for the $PtCe_{sul}$-5 and PtC(Cr_3C_2) catalysts, respectively. According to Yuan *et al.* [164], in the case of Pt−CeO_2/C(CNT), the splitting of CO stripping peak can be caused by the participation of the hydroxyl groups on the CeO_2 surface on the CO oxidation and the water adsorption is more favourable on Pt−CeO_2 surface, even at low potentials, e.g. around 0.63 V [164]. This phenomenon has been also observed for Pt−CeO_2/C and PtRu catalysts before [164, 165]. However, the presence of the CO oxidation peak splitting for the PtC(Cr_3C_2) points out the fact that, in our case, this is the synergistic influence of C(Cr_3C_2, 900) support surface and Pt. The C(Cr_3C_2, 900) alone is not able to oxidise CO (see Figure 45). Nevertheless, if activie sites on C(Cr_3C_2, 900) support are coupled with the Pt NPs, these sites enhance the CO oxidation on the Pt NPs. As our C(Cr_3C_2, 900)

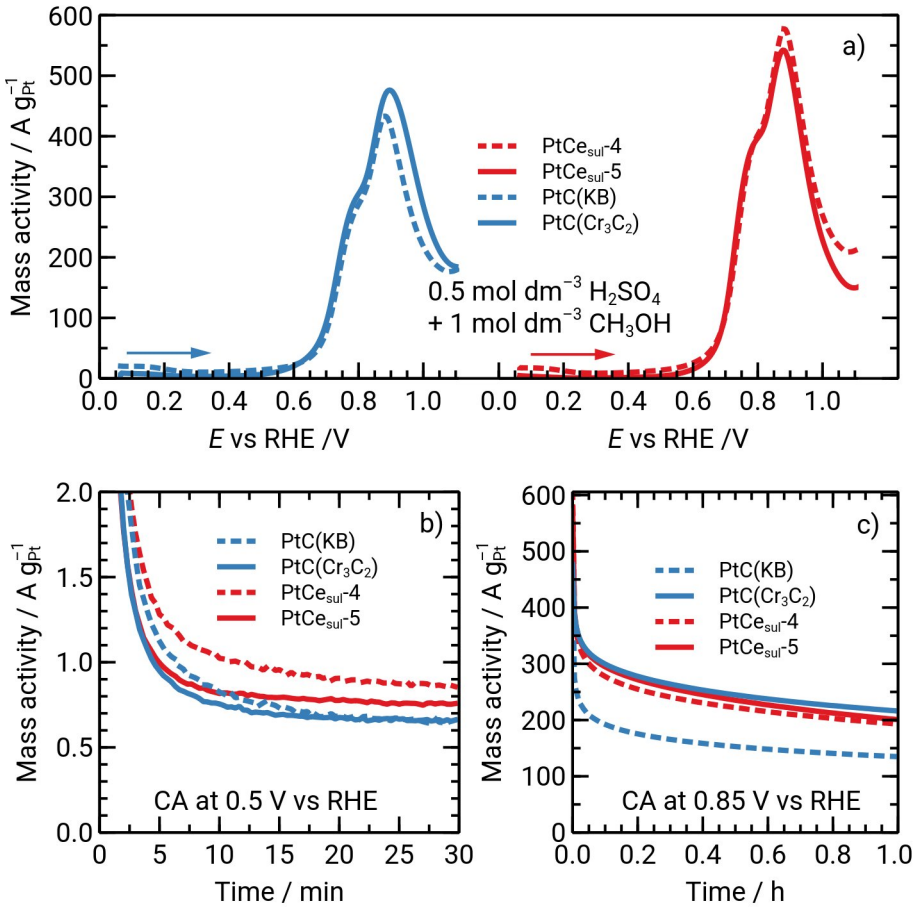

Figure 46. The influence of catalyst support (chromium carbide-derived carbon or carbon black) on methanol oxidation activity of selected catalysts.

possesses a trace amount of chromium [166], the chromium NPs covered by carbon layers can be a part of the active site. The CO oxidation activity of the $PtCe_{sul}$-5 catalyst is slightly higher than that of $PtC(Cr_3C_2)$ catalyst, as the E_1 values are 0.715 and 0.730 V, respectively. Therefore, the CeO_2 alone does contribute to overall CO oxidation activity. The CO oxidation peak potential E_2 values of the $PtCe_{sul}$-5 and $PtC(Cr_3C_2)$ catalysts are smaller than the E_2 values of the $PtCe_{sul}$-1 and PtC(KB) catalysts (see Figure 45). Moreover, the current density values of the $PtCe_{sul}$-5 and $PtC(Cr_3C_2)$ catalysts in the potential region from 0.68 to 0.73 V are higher than that of the $PtCe_{sul}$-4 catalyst. This indicates the CO oxidation for the $C(Cr_3C_2)$-based catalysts start at less positive potentials and is more aggressive.

6.4 The Best Catalyst Materials

This study focuses on the development of $Pt{-}CeO_2/C$ catalyst materials for the MOR. The comparable type of catalyst materials measured in the comparable conditions from other studies are compiled into the Table 16. The most important value for comparing the MOR activity of these materials is MOR mass activity, i_{CA}, determined from CA measurement. The CA measurement is performed at a potential corresponding to the MOR peak of the anode sweep in the CV experiment. This i_{CA} value reflects the stable MOR activity of a catalyst at the high reaction rate conditions (at 0.85 V) during short time period (1 h).

The comparison in the Table 16 reveals that the MOR activity of $Pt{-}CeO_2/C$ and PtC catalyst materials is in the range as for the best catalyst materials of the same type. The catalyst materials in the Table 16 are amongst the best Pt-based catalysts based on the literature. The $Pt{-}CeO_2/C$ catalyst material synthesised by Chen *et al.* [47] has lower activity because Pt was deposited onto the CeO_2 to form the $Pt{-}CeO_2$ complexes. Later, the $Pt{-}CeO_2$ complexes were mixed with carbon to deposit them onto the electrode surface for the electrochemical measurement. As a final result, the MOR activity of this material ($i_{CA} = 10$ $A\,g_{Pt}^{-1}$) is low due to the low electric conductivity of the CeO_2 NPs, deposited onto carbon support.

Table 16. The methanol oxidation reaction (MOR) activity of our most active materials compared to the activity of the best catalysts from other studies.

Material	Pt wt%	Electrolyte	E_{CA}/ V vs RHE	i_{CA}/ $A\,g_{Pt}^{-1}$	Reference
$PtCe_{sul}$-5	22	$1\,mol\,dm^{-3}$ CH_3OH + $0.5\,mol\,dm^{-3}$ H_2SO_4	0.85	201±16	this work
$PtC(Cr_3C_2)$	20	$1\,mol\,dm^{-3}$ CH_3OH + $0.5\,mol\,dm^{-3}$ H_2SO_4	0.85	216±17	this work
Pt/CeO_2-C	20	$1\,mol\,dm^{-3}$ CH_3OH + $0.5\,mol\,dm^{-3}$ H_2SO_4	0.90	210	[48]
$Pt/His-CeO_2-C$	20	$1\,mol\,dm^{-3}$ CH_3OH + $0.5\,mol\,dm^{-3}$ H_2SO_4	0.90	310	[48]
$PtRu/CeO_2-C$ (CeO_2 20 wt%)	6.7	$1\,mol\,dm^{-3}$ CH_3OH + $0.5\,mol\,dm^{-3}$ H_2SO_4	0.86	210	[43]
$Pt-CeO_2/C$	9	$1\,mol\,dm^{-3}$ CH_3OH + $0.5\,mol\,dm^{-3}$ H_2SO_4	0.85	10	[47]
PtPdCr/C	6	$0.5\,mol\,dm^{-3}$ CH_3OH + $0.1\,mol\,dm^{-3}$ $HClO_4$	1.08[a]	60	[167]

[a]The potential value at the anode peak in cyclic voltammetry for the MOR. i_{CA} is the mass activity for MOR, which is measured by chronoamperometry at the potential E_{CA}.

7. SUMMARY

New composite catalysts based on Pt and CeO_2 nanoparticles (NPs) deposited on carbon were developed for the methanol oxidation reaction (MOR) and oxygen reduction reaction (ORR) in the doctoral thesis.

The optimisation of CeO_2 NPs synthesis was performed. CeO_2 particles with various shapes (flower-shaped and polygonal), sizes (from 3 nm to 30 μm) were synthesised successfully. It was established that the parameters of ultrasound and microwave radiation method did not influence the physicochemical characteristics of the synthesised CeO_2 NPs.

The ethylene glycol (EG) reduction method was applied for the synthesis and deposition of Pt NPs. It was found that the generation of glycolate anions in the reaction mixture before the EG reduction synthesis changed the physical characteristics of the Pt NPs and enhanced the electrochemical activity of the Pt−CeO_2/C catalysts. Three excitation methods were used to induce the formation of Pt NPs: ultrasonic treatment, microwave synthesis, and heating the reaction mixture in an oil bath. The duration of ultrasound and microwave radiation somewhat influenced the properties of the NPs. Longer microwave treatment tended to cause the agglomeration of Pt NPs on the carbon support surface, while a longer refluxing duration caused the growth of the Pt NPs. The initial substrate materials (chromium carbide-derived carbon (CDC) and commercial Ketjenblack carbon) and chemical concentrations (Na^+, OH^-, $[PtCl_6]_2^-$, and glycolate ions) in the reaction mixture affected the physicochemical characteristics and the electrochemical activity of synthesised Pt−CeO_2/C catalysts. Various strategies (combination of different heating methods, adjusting pH, using stronger reducing reagents) to deposit Pt and CeO_2 NPs on the carbon surface were studied. When the optimal synthesis conditions were used, the average Pt NP diameter was around 3.0 nm, and the Pt NPs were not agglomerated according to TEM images.

The CDC support materials were found to be suitable for developing highly active catalysts for proton exchange membrane fuel cell applications. The chromium CDCs had a micro-mesoporous structure, and the synthesis temperature of CDCs significantly influenced the carbon crystallographic structure, including the graphitisation ratio and micropore and mesopore volume values. When the C(Cr_3C_2, 900) material was used as catalyst support, the MOR as well as ORR activity of the Pt−CeO_2/C and Pt/C catalysts were enhanced. The most promising catalyst was PtC(Cr_3C_2), which achieved outstanding MOR activity. The MOR activity at 0.85 V vs reversible hydrogen electrode (RHE) of the Pt/C catalyst on the C(Cr_3C_2) support was as good as the MOR activity of the best Pt−CeO_2/C on commercial Ketjenblack carbon.

It was found that hydrogen post-treatment after the EG reduction synthesis altered the physical properties of Pt−CeO_2/C catalysts. The hydrogen post-treatment improved the MOR activity and stability of some Pt−CeO_2/C

materials. The increased metallic Pt content in the catalyst likely caused the improvement. On the other hand, the MOR activity of the $PtCe_{H_3PO_4}$ catalyst, which was the Pt-based catalyst containing both CeO_2 and $CePO_4$ NPs, decreased significantly after the hydrogen post-treatment. This was an expected result because the hydrogen post-treatment broke the fluorite structure of the $PtCe_{H_3PO_4}$ material. Therefore, the synergistic effects of cerium compounds coupled with Pt were eliminated.

The synthesis of the $Pt-CeO_2/C$ catalysts was successful. The synergistic effect of CeO_2 coupled with Pt was observed as an improvement in the catalytic activity for both MOR and ORR. Many catalysts achieved comparably high MOR and ORR activity; however, the $PtCe_{sul}$-5 material was the best catalyst for both MOR and ORR. In the ORR, MA and SA values calculated for the best catalyst, $PtCe_{sul}$-5, at 0.90 V were $(288 \pm 1)\,A\,g_{Pt}^{-1}$ and $(4.0 \pm 0.1)\,A\,m_{Pt}^{-2}$, respectively. In the MOR, the i_{CA} at 0.85 V vs RHE was as high as $(201 \pm 16)\,A\,g_{Pt}^{-1}$ and this result is in the range of top materials with very high MOR activity.

8. REFERENCES

[1] D. Howell, S. Boyd, B. Cunningham, S. Gillard, L. Slezak Enabling Fast Charging: A Technology Gap Assessment U.S. Department of Energy **2017**.

[2] P. Mishra, E. Miller, S. Santhanagopalan, K. Bennion, A. Meintz, Energies 15 (**2022**) 3788. DOI: 10.3390/en15103788.

[3] M. M. Whiston, I. L. Azevedo, S. Litster, K. S. Whitefoot, C. Samaras, J. F. Whitacre, Proc. Natl. Acad. Sci. 116 (**2019**) 4899–4904. DOI: 10.1073/pnas.1804221116.

[4] H. R. Corti, E. R. Gonzalez, *Direct Alcohol Fuel Cells*, Springer Netherlands, Dordrecht, **2014**. 370 pp. DOI: 10.1007/978-94-007-7708-8.

[5] G. Kerangueven, C. Coutanceau, E. Sibert, J. .-. Léger, C. Lamy, J. Power Sources 157 (**2006**) 318–324. DOI: 10.1016/j.jpowsour.2005.07.080.

[6] K. Yamada, K. Yasuda, H. Tanaka, Y. Miyazaki, T. Kobayashi, Journal of Power Sources 122 (**2003**) 132–137. DOI: 10.1016/S0378-7753(03)00440-3.

[7] K. Asazawa, K. Yamada, H. Tanaka, A. Oka, M. Taniguchi, T. Kobayashi, Angewandte Chemie International Edition 46 (**2007**) 8024–8027. DOI: 10.1002/anie.200701334.

[8] Y. Wang, K. S. Chen, J. Mishler, S. C. Cho, X. C. Adroher, Appl. Energy 88 (**2011**) 981–1007. DOI: 10.1016/j.apenergy.2010.09.030.

[9] O. Siddiqui, I. Dincer, Therm. Sci. Eng. Prog. 5 (**2018**) 568–578. DOI: 10.1016/j.tsep.2018.02.011.

[10] A. Serov, C. Kwak, Appl. Catal. B: Environ. 98 (**2010**) 1–9. DOI: 10.1016/j.apcatb.2010.05.005.

[11] T. Li, P. B. Balbuena, J. Phys. Chem. B 105 (**2001**) 9943–9952. DOI: 10.1021/jp0118219.

[12] J. Huang, M. Eikerling, Curr. Opin. Electrochem. 13 (**2019**) 157–165. DOI: 10.1016/j.coelec.2019.01.004.

[13] E. Yeager, J. Mol. Catal. 38 (**1986**) 5–25. DOI: 10.1016/0304-5102(86)87045-6.

[14] N. M. Marković, T. J. Schmidt, V. Stamenković, P. N. Ross, Fuel Cells 1 (**2001**) 105–116. DOI: 10.1002/1615-6854(200107)1:2<105::AID-FUCE105>3.0.CO;2-9.

[15] A. Dushina, H. Schmies, D. Schonvogel, A. Dyck, P. Wagner, Int. J. Hydrog. Energy 45 (**2020**) 35073–35084. DOI: 10.1016/j.ijhydene.2020.05.038.

[16] R. Venkataraman, H. R. Kunz, J. M. Fenton, J. Electrochem. Soc. 151 (**2004**) A710. DOI: 10.1149/1.1701870.

[17] C. Y. Du, T. S. Zhao, W. W. Yang, Electrochim. Acta 52 (**2007**) 5266–5271. DOI: 10.1016/j.electacta.2007.01.089.

[18] Y. V. Tolmachev, O. A. Petrii, J Solid State Electrochem 21 (**2017**) 613–639. DOI: 10.1007/s10008-016-3382-5.

[19] Q. Lu, Z. Wang, Y. Tang, C. Huang, A. Zhang, F. Liu, X. Liu, B. Shan, R. Chen, Sustain. Energy Fuels 6 (**2022**) 2989–2995. DOI: 10.1039/D2SE00586G.

[20] Y.-Y. Feng, H.-S. Hu, G.-H. Song, S. Si, R.-J. Liu, D.-N. Peng, D.-S. Kong, J. Alloys Compd. 798 (**2019**) 706–713. DOI: 10.1016/j.jallcom.2019.05.287.

[21] E. Antolini, J. Perez, Int. J. Hydrog. Energy 36 (**2011**) 15752–15765. DOI: 10.1016/j.ijhydene.2011.08.104.

[22] C. Xu, R. Zeng, P. K. Shen, Z. Wei, Electrochim. Acta 51 (**2005**) 1031–1035. DOI: 10.1016/j.electacta.2005.05.041.

[23] D. Y. Chung, K.-J. Lee, Y.-E. Sung, J. Phys. Chem. C 120 (**2016**) 9028–9035. DOI: 10.1021/acs.jpcc.5b12303.

[24] J. E. Sulaiman, S. Zhu, Z. Xing, Q. Chang, M. Shao, ACS Catal. 7 (**2017**) 5134–5141. DOI: 10.1021/acscatal.7b01435.

[25] Z. Yang, M. Chen, M. Xia, M. Wang, X. Wang, Appl. Surf. Sci. 487 (**2019**) 655–663. DOI: 10.1016/j.apsusc.2019.04.237.

[26] A. A. Yaroshevsky, Geochem. Int. 44 (**2006**) 48–55. DOI: 10.1134/S001670290601006X.

[27] S. Samad, K. S. Loh, W. Y. Wong, T. K. Lee, J. Sunarso, S. T. Chong, W. R. Wan Daud, Int. J. Hydrogen Energ. 43 (**2018**) 7823–7854. DOI: 10.1016/j.ijhydene.2018.02.154.

[28] S. Sharma, B. G. Pollet, J. Power Sources 208 (**2012**) 96–119. DOI: 10.1016/j.jpowsour.2012.02.011.

[29] E. Antolini, Appl. Catal. B-Environ. 88 (**2009**) 1–24. DOI: 10.1016/j.apcatb.2008.09.030.

[30] M. Yaldagard, M. Jahanshahi, N. Seghatoleslami, World J. Nano Sci. Eng. 03 (**2013**) 121. DOI: 10.4236/wjnse.2013.34017.

[31] J. Tae Hwang, J. Shik Chung, Electrochim. Acta 38 (**1993**) 2715–2723. DOI: 10.1016/0013-4686(93)85090-L.

[32] K. Vaarmets, J. Nerut, S. Sepp, R. Kanarbik, E. Lust, J. Electrochem. Soc. 164 (**2017**) F338–F346. DOI: 10.1149/2.1021704jes.

[33] S. Sepp, K. Vaarmets, J. Nerut, I. Tallo, E. Tee, H. Kurig, J. Aruväli, R. Kanarbik, E. Lust, Electrochim. Acta 203 (**2016**) 221–229. DOI: 10.1016/j.electacta.2016.03.158.

[34] A. Jänes, T. Thomberg, H. Kurig, E. Lust, Carbon 47 (**2009**) 23–29. DOI: 10.1016/j.carbon.2008.07.010.

[35] E. Härk, J. Nerut, K. Vaarmets, I. Tallo, H. Kurig, J. Eskusson, K. Kontturi, E. Lust, J. Electroanal. Chem. 689 (**2013**) 176–184. DOI: 10.1016/j.jelechem.2012.09.039.

[36] A. Jänes, T. Thomberg, E. Lust, Carbon 45 (**2007**) 2717–2722. DOI: 10.1016/j.carbon.2007.09.041.

[37] I. Tallo, T. Thomberg, H. Kurig, K. Kontturi, A. Jänes, E. Lust, Carbon 67 (**2014**) 607–616. DOI: 10.1016/j.carbon.2013.10.034.

[38] I. Tallo, T. Thomberg, H. Kurig, A. Jänes, K. Kontturi, E. Lust, J. Solid State Electrochem. 17 (**2013**) 19–28. DOI: 10.1007/s10008-012-1850-0.

[39] T. Thomberg, H. Kurig, A. Jänes, E. Lust, Micropor. Mesopor. Mat. 141 (**2011**) 88–93. DOI: 10.1016/j.micromeso.2010.11.006.

[40] J. Xu, R. Zhang, J. Wang, S. Ge, H. Zhou, Y. Liu, P. Chen, Carbon 52 (**2013**) 499–508. DOI: 10.1016/j.carbon.2012.10.002.

[41] E. N. Hoffman, G. Yushin, T. El-Raghy, Y. Gogotsi, M. W. Barsoum, Micropor. Mesopor. Mat. 112 (**2008**) 526–532. DOI: 10.1016/j.micromeso.2007.10.033.

[42] M. A. Scibioh, S.-K. Kim, E. A. Cho, T.-H. Lim, S.-A. Hong, H. Y. Ha, Appl. Catal. B: Environ. 84 (**2008**) 773–782. DOI: 10.1016/j.apcatb.2008.06.017.

[43] S.-Y. Huang, C.-M. Chang, C.-T. Yeh, J. Catal. 241 (**2006**) 400–406. DOI: 10.1016/j.jcat.2006.04.020.

[44] C. L. Perkins, M. A. Henderson, C. H. F. Peden, G. S. Herman, J. Vac. Sci. Technol. A 19 (**2001**) 1942–1946. DOI: 10.1116/1.1336831.

[45] P. Bera, A. Gayen, M. S. Hegde, N. P. Lalla, L. Spadaro, F. Frusteri, F. Arena, J. Phys. Chem. B 107 (**2003**) 6122–6130. DOI: 10.1021/jp022132f.

[46] H. Xu, X. Hou, Int. J. Hydrog. Energy 32 (**2007**) 4397–4401. DOI: 10.1016/j.ijhydene.2007.05.041.

[47] W. Chen, J. Xue, Y. Bao, L. Feng, Chem. Eng. J. 381 (**2020**) 122752. DOI: 10.1016/j.cej.2019.122752.

[48] S. Dai, J. Zhang, Y. Fu, W. Li, New J. Chem. 42 (**2018**) 18159–18165. DOI: 10.1039/C8NJ03972K.

[49] E. Yeager, Electrochim. Acta 29 (**1984**) 1527–1537. DOI: 10.1016/0013-4686(84)85006-9.

[50] J. K. Nørskov, J. Rossmeisl, A. Logadottir, L. Lindqvist, J. R. Kitchin, T. Bligaard, H. Jónsson, J. Phys. Chem. B 108 (**2004**) 17886–17892. DOI: 10.1021/jp047349j.

[51] H. S. Wroblowa, Yen-Chi-Pan, G. Razumney, J. Electroanal. Chem. Interfacial Electrochem. 69 (**1976**) 195–201. DOI: 10.1016/S0022-0728(76)80250-1.

[52] J. R. Kitchin, J. K. Nørskov, M. A. Barteau, J. G. Chen, J. Chem. Phys. 120 (**2004**) 10240–10246. DOI: 10.1063/1.1737365.

[53] Y. Xu, A. V. Ruban, M. Mavrikakis, J. Am. Chem. Soc. 126 (**2004**) 4717–4725. DOI: 10.1021/ja031701+.

[54] N. M. Marković, P. N. Ross, Surf. Sci. Rep. 45 (**2002**) 117–229. DOI: 10.1016/S0167-5729(01)00022-X.

[55] T. Toda, H. Igarashi, H. Uchida, M. Watanabe, J. Electrochem. Soc. 146 (**1999**) 3750. DOI: 10.1149/1.1392544.

[56] V. Stamenković, T. J. Schmidt, P. N. Ross, N. M. Marković, J. Phys. Chem. B 106 (**2002**) 11970–11979. DOI: 10.1021/jp021182h.

[57] M. Taleb, J. Nerut, T. Tooming, T. Thomberg, A. Jänes, E. Lust, J. Electrochem. Soc. 162 (**2015**) F651. DOI: 10.1149/2.0231507jes.

[58] R. J. Taylor, A. A. Humffray, J. Electroanal. Chem. Interfacial Electrochem. 64 (**1975**) 85–94. DOI: 10.1016/S0022-0728(75)80279-8.

[59] J. L. Cohen, D. J. Volpe, H. D. Abruña, Phys. Chem. Chem. Phys. 9 (**2006**) 49–77. DOI: 10.1039/B612040G.

[60] M. J. S. Farias, W. Cheuquepán, A. A. Tanaka, J. M. Feliu, ACS Catal. 10 (**2020**) 543–555. DOI: 10.1021/acscatal.9b04275.

[61] Y. X. Chen, A. Miki, S. Ye, H. Sakai, M. Osawa, J. Am. Chem. Soc. 125 (**2003**) 3680–3681. DOI: 10.1021/ja029044t.

[62] F. Maillard, G.-Q. Lu, A. Wieckowski, U. Stimming, J. Phys. Chem. B 109 (**2005**) 16230–16243. DOI: 10.1021/jp052277x.

[63] T. Yao, S. Liu, Z. Sun, Y. Li, S. He, H. Cheng, Y. Xie, Q. Liu, Y. Jiang, Z. Wu, Z. Pan, W. Yan, S. Wei, J. Am. Chem. Soc. 134 (**2012**) 9410–9416. DOI: 10.1021/ja302642x.

[64] C. Bock, C. Paquet, M. Couillard, G. A. Botton, B. R. MacDougall, J. Am. Chem. Soc. 126 (**2004**) 8028–8037. DOI: 10.1021/ja0495819.

[65] I. Schrader, J. Warneke, S. Neumann, S. Grotheer, A. A. Swane, J. J. K. Kirkensgaard, M. Arenz, S. Kunz, J. Phys. Chem. C 119 (**2015**) 17655–17661. DOI: 10.1021/acs.jpcc.5b03863.

[66] I. M. Lifshitz, V. V. Slyozov, J. Phys. Chem. Solids 19 (**1961**) 35–50. DOI: 10.1016/0022-3697(61)90054-3.

[67] D. Erdemir, A. Y. Lee, A. S. Myerson, Acc. Chem. Res. 42 (**2009**) 621–629. DOI: 10.1021/ar800217x.

[68] V. K. LaMer, R. H. Dinegar, J. Am. Chem. Soc. 72 (**1950**) 4847–4854. DOI: 10.1021/ja01167a001.

[69] Y. Sun, Chem. Soc. Rev. 42 (**2013**) 2497–2511. DOI: 10.1039/C2CS35289C.

[70] A. Henglein, M. Giersig, J. Phys. Chem. B 104 (**2000**) 6767–6772. DOI: 10.1021/jp000801o.

[71] A. A. Alekseenko, V. E. Guterman, V. A. Volochaev, S. V. Belenov, Inorg. Mater. 51 (**2015**) 1258–1263. DOI: 10.1134/S0020168515120018.

[72] M. Danilenko, V. Guterman, K. Paperzh, A. Alekseenko, A. Nikulin, IOP Conf. Ser.: Earth Environ. Sci. 987 (**2022**) 012022. DOI: 10.1088/1755-1315/987/1/012022.

[73] P. Valk, J. Nerut, R. Kanarbik, I. Tallo, J. Aruväli, E. Lust, J. Electrochem. Soc. 165 (**2018**) F315–F323. DOI: 10.1149/2.0781805jes.

[74] J. Yang, T. Deivaraj, H.-P. Too, J. Lee, Langmuir 20 (**2004**) 4241–4245. DOI: 10.1021/la0361159.

[75] K. Takahashi, S. Yokoyama, T. Matsumoto, J. L. C. Huaman, H. Kaneko, J.-Y. Piquemal, H. Miyamura, J. Balachandran, New J. Chem. 40 (**2016**) 8632–8642. DOI: 10.1039/C6NJ01738J.

[76] J. Quinson, A. Dworzak, S. B. Simonsen, L. Theil Kuhn, K. M. Ø. Jensen, A. Zana, M. Oezaslan, J. J. K. Kirkensgaard, M. Arenz, Appl. Surf. Sci. 549 (**2021**) 149263. DOI: 10.1016/j.apsusc.2021.149263.

[77] M. E. Hyde, R. G. Compton, J. Electroanal. Chem. 549 (**2003**) 1–12. DOI: 10.1016/S0022-0728(03)00250-X.

[78] N. T. K. Thanh, N. Maclean, S. Mahiddine, Chem. Rev. 114 (**2014**) 7610–7630. DOI: 10.1021/cr400544s.

[79] M. V. Danilenko, V. E. Guterman, E. V. Vetrova, A. V. Metelitsa, K. O. Paperzh, I. V. Pankov, O. I. Safronenko, Colloids Surf. A 630 (**2021**) 127525. DOI: 10.1016/j.colsurfa.2021.127525.

[80] D. R. Lide, G. Baysinger, S. Chemistry, L. I. Berger, R. N. Goldberg, H. V. Kehiaian, *CRC Handbook of Chemistry and Physics*, **2005**. 2661 pp.

[81] J. Shen, Z. Li, Q. Yan, Y. Chen, J. Phys. Chem. 97 (**1993**) 8504–8511. DOI: 10.1021/j100134a020.

[82] H.-S. Oh, J.-G. Oh, Y.-G. Hong, H. Kim, Electrochim. Acta 52 (**2007**) 7278–7285. DOI: 10.1016/j.electacta.2007.05.080.

[83] J.-B. Joo, P. Kim, K. Wooyoung, Y. Kim, J. Yi, J. Appl. Electrochem. 39 (**2009**) 135–140. DOI: 10.1007/s10800-008-9645-9.

[84] J. Speder, L. Altmann, M. Roefzaad, M. Bäumer, J. J. K. Kirkensgaard, K. Mortensen, M. Arenz, Phys. Chem. Chem. Phys. 15 (**2013**) 3602–3608. DOI: 10.1039/C3CP50195G.

[85] J. Quinson, L. Kacenauskaite, J. Bucher, S. B. Simonsen, L. Theil Kuhn, M. Oezaslan, S. Kunz, M. Arenz, ChemSusChem 12 (**2019**) 1229–1239. DOI: 10.1002/cssc.201802897.

[86] J. Solla-Gullón, F. J. Vidal-Iglesias, A. López-Cudero, E. Garnier, J. M. Feliu, A. Aldaz, Phys. Chem. Chem. Phys. 10 (**2008**) 3689–3698. DOI: 10.1039/B802703J.

[87] H.-X. Mai, L.-D. Sun, Y.-W. Zhang, R. Si, W. Feng, H.-P. Zhang, H.-C. Liu, C.-H. Yan, J. Phys. Chem. B 109 (**2005**) 24380–24385. DOI: 10.1021/jp055584b.

[88] M. Omran, T. Fabritius, G. Chen, A. He, RSC Adv. 9 (**2019**) 6859–6870. DOI: 10.1039/C9RA00009G.

[89] D. Nunes, A. Pimentel, L. Santos, P. Barquinha, L. Pereira, E. Fortunato, R. Martins, in: D. Nunes, A. Pimentel, L. Santos, P. Barquinha, L. Pereira, E. Fortunato, R. Martins (Eds.), *Metal Oxide Nanostructures*, Elsevier, Amsterdam, **2019**, pp. 21–57. DOI: 10.1016/B978-0-12-811512-1.00002-3.

[90] R. Sharma, Y. Wang, F. Li, J. Chamier, S. M. Andersen, ACS Omega 4 (**2019**) 15711–15720. DOI: 10.1021/acsomega.9b02351.

[91] L.-b. Zhang, A.-y. Ma, C.-h. Liu, W.-w. Qu, J.-h. Peng, Y.-g. Luo, Y.-g. Zuo, Trans. Nonferrous Met. Soc. China 24 (**2014**) 4004–4011. DOI: 10.1016/S1003-6326(14)63562-7.

[92] A. Arafat, J. C. Jansen, A. R. Ebaid, H. van Bekkum, Zeolites 13 (**1993**) 162–165. DOI: 10.1016/S0144-2449(05)80272-6.

[93] D. Patil, B. Mutsuddy, R. Garard, J. Microw. Power Electromagn. Energy 27 (**1992**) 49–53. DOI: 10.1080/08327823.1992.11688170.

[94] M. Tsuji, M. Kubokawa, R. Yano, N. Miyamae, T. Tsuji, M.-S. Jun, S. Hong, S. Lim, S.-H. Yoon, I. Mochida, Langmuir 23 (**2007**) 387–390. DOI: 10.1021/la062223u.

[95] R. N. Gedye, W. Rank, K. C. Westaway, Can. J. Chem. 69 (**1991**) 706–711. DOI: 10.1139/v91-106.

[96] G. Majetich, R. Hicks, J. Microw. Power Electromagn. Energy 30 (**1995**) 27–45. DOI: 10.1080/08327823.1995.11688258.

[97] R. Laurent, A. Laporterie, J. Dubac, J. Berlan, S. Lefeuvre, M. Audhuy, J. Org. Chem. 57 (**1992**) 7099–7102. DOI: 10.1021/jo00052a022.

[98] J. H. Bang, K. S. Suslick, Adv. Mater. 22 (**2010**) 1039–1059. DOI: 10.1002/adma.200904093.

[99] R.-J. Qi, Y.-J. Zhu, G.-F. Cheng, Y.-H. Huang, Nanotechnology 16 (**2005**) 2502–2506. DOI: 10.1088/0957-4484/16/11/006.

[100] D. V. Pinjari, A. B. Pandit, Ultrason. Sonochem. 18 (**2011**) 1118–1123. DOI: 10.1016/j.ultsonch.2011.01.008.

[101] S. B. Atla, M.-N. Wu, W. Pan, Y. T. Hsiao, A.-C. Sun, M.-J. Tseng, Y.-J. Chen, C.-Y. Chen, Mater. Charact. 98 (**2014**) 202–208. DOI: 10.1016/j.matchar.2014.10.022.

[102] G. Zhang, Z. Shen, M. Liu, C. Guo, P. Sun, Z. Yuan, B. Li, D. Ding, T. Chen, J. Phys. Chem. B 110 (**2006**) 25782–25790. DOI: 10.1021/jp0648285.

[103] P. H. Emmett, S. Brunauer, J. Am. Chem. Soc. 59 (**1937**) 1553–1564. DOI: 10.1021/ja01287a041.

[104] S. Brunauer, P. H. Emmett, E. Teller, J. Am. Chem. Soc. 60 (**1938**) 309–319. DOI: 10.1021/ja01269a023.

[105] J. H. de Boer, B. C. Lippens, B. G. Linsen, J. C. P. Broekhoff, A. van den Heuvel, T. J. Osinga, J. Colloid Interf. Sci. 21 (**1966**) 405–414. DOI: 10.1016/0095-8522(66)90006-7.

[106] J. Jagiello, J. P. Olivier, Adsorption 19 (**2013**) 777–783. DOI: 10.1007/s10450-013-9517-4.

[107] J. Jagiello, J. P. Olivier, Carbon 55 (**2013**) 70–80. DOI: 10.1016/j.carbon.2012.12.011.

[108] P. C. Hansen, D. P. O'Leary, SIAM J. Sci. Comput. 14 (**1993**) 1487–1503. DOI: 10.1137/0914086.

[109] C. L. Lawson, R. J. Hanson, *Solving Least Squares Problems*, Society for Industrial and Applied Mathematics, Philadelphia, **1987**. 350 pp.

[110] R. L. Snyder, J. Fiala, H. J. Bunge, *Defect and Microstructure Analysis by Diffraction*, International Union of Crystallography, Oxford, **1999**. 785 pp.

[111] A. Ferrari, J. Robertson, Phys. Rev. B: Condens. Matter Mater. Phys. 61 (**2000**) 14095–14107. DOI: 10.1103/PhysRevB.61.14095.

[112] L. M. Malard, M. A. Pimenta, G. Dresselhaus, M. S. Dresselhaus, Phys. Rep. 473 (**2009**) 51–87. DOI: 10.1016/j.physrep.2009.02.003.

[113] D. B. Schuepfer, F. Badaczewski, J. M. Guerra-Castro, D. M. Hofmann, C. Heiliger, B. Smarsly, P. J. Klar, Carbon 161 (**2020**) 359–372. DOI: 10.1016/j.carbon.2019.12.094.

[114] M. S. Brogan, T. J. Dines, J. A. Cairns, J. Chem. Soc. Faraday Trans. 90 (**1994**) 1461–1466. DOI: 10.1039/FT9949001461.

[115] C. Schilling, A. Hofmann, C. Hess, M. V. Ganduglia-Pirovano, J. Phys. Chem. C 121 (**2017**) 20834–20849. DOI: 10.1021/acs.jpcc.7b06643.

[116] I. Kosacki, T. Suzuki, H. U. Anderson, P. Colomban, Solid State Ion. 149 (**2002**) 99–105. DOI: 10.1016/S0167-2738(02)00104-2.

[117] S. Loridant, Catal. Today 373 (**2021**) 98–111. DOI: 10.1016/j.cattod.2020.03.044.

[118] Z. L. Wang, J. Phys. Chem. B 104 (**2000**) 1153–1175. DOI: 10.1021/jp993593c.

[119] V.-L. Nguyen, M. Ohtaki, V. N. Ngo, M.-T. Cao, M. Nogami, Adv. Nat. Sci: Nanosci. Nanotechnol. 3 (**2012**) 025005. DOI: 10.1088/2043-6262/3/2/025005.

[120] D. Chen, Y. Zhao, X. Peng, X. Wang, W. Hu, C. Jing, S. Tian, J. Tian, Electrochim. Acta 177 (**2015**) 86–92. DOI: 10.1016/j.electacta.2015.03.066.

[121] P. Valk, J. Nerut, I. Tallo, E. Tee, K. Vaarmets, T. Romann, H. Kurig, R. Palm, E. Lust, Electrochim. Acta 191 (**2016**) 337–345. DOI: 10.1016/j.electacta.2016.01.048.

[122] D. A. Skoog, F. J. Holler, S. R. Crouch, *Principles of Instrumental Analysis - Seventh Edition* 7th ed., Cengage Learning, Boston, **2017**. 992 pp.

[123] R. G. Compton, C. E. Banks, *Understanding Voltammetry (Third Edition)* 3rd, World Scientific, New Jersey, **2018**. 456 pp.

[124] B. E. Conway, V. Birss, J. Wojtowicz, J. Power Sources 66 (**1997**) 1–14. DOI: 10.1016/S0378-7753(96)02474-3.

[125] T. J. Schmidt, H. A. Gasteiger, G. D. Stäb, P. M. Urban, D. M. Kolb, R. J. Behm, J. Electrochem. Soc. 145 (**1998**) 2354–2358. DOI: 10.1149/1.1838642.

[126] F. J. Nores-Pondal, I. M. J. Vilella, H. Troiani, M. Granada, S. R. de Miguel, O. A. Scelza, H. R. Corti, Int. J. Hydrog. Energy 34 (**2009**) 8193–8203. DOI: 10.1016/j.ijhydene.2009.07.073.

[127] S. Trasatti, O. A. Petrii, J. Electroanal. Chem. 327 (**1992**) 353–376. DOI: 10.1016/0022-0728(92)80162-W.

[128] T. Biegler, D. A. J. Rand, R. Woods, J. Electroanal. Chem. Interfacial Electrochem. 29 (**1971**) 269–277. DOI: 10.1016/S0022-0728(71)80089-X.

[129] F. Maillard, M. Martin, F. Gloaguen, J. .-. Léger, Electrochim. Acta 47 (**2002**) 3431–3440. DOI: 10.1016/S0013-4686(02)00279-7.

[130] A. J. Bard, L. R. Faulkner, *Electrochemical Methods: Fundamentals and Applications* 2nd, Wiley, New York, **2001**. 833 pp.

[131] N. M. Marković, H. A. Gasteiger, B. N. Grgur, P. N. Ross, J. Electroanal. Chem. 467 (**1999**) 157–163. DOI: 10.1016/S0022-0728(99)00020-0.

[132] L. H. Brickwedde, J. Res. Natl. Bur. Stan. 42 (**1949**) 309. DOI: 10.6028/jres.042.026.

[133] A. Holewinski, S. Linic, J. Electrochem. Soc. 159 (**2012**) H864–H870. DOI: 10.1149/2.022211jes.

[134] A. Parthasarathy, S. Srinivasan, A. J. Appleby, C. R. Martin, J. Electroanal. Chem. 339 (**1992**) 101–121. DOI: 10.1016/0022-0728(92)80447-C.

[135] É. C. G. Rufino, P. Olivi, Int. J. Hydrog. Energy 35 (**2010**) 13298–13308. DOI: 10.1016/j.ijhydene.2010.09.020.

[136] Z. Yang, S. Xu, J. Xie, J. Liu, J. Tian, P. Wang, Z. Zou, J. Appl. Electrochem. 46 (**2016**) 895–900. DOI: 10.1007/s10800-016-0963-z.

[137] Z. Cai, Z. Lu, Y. Bi, Y. Li, Y. Kuang, X. Sun, Chem. Commun. 52 (**2016**) 3903–3906. DOI: 10.1039/C5CC10513G.

[138] T. Zhang, Y. Sun, X. Li, X. Li, D. Liu, G. Liu, C. Li, H. J. Fan, Y. Li, Small Methods 4 (**2020**) 1900709. DOI: 10.1002/smtd.201900709.

[139] H. Q. V. Nguyen, J. Nerut, H. Kasuk, M. Härmas, P. Valk, T. Romann, M. Koppel, P. Teppor, J. Aruväli, O. Korjus, O. Volobujeva, E. Lust, J. Solid State Electrochem. 27 (**2023**) 313–326. DOI: 10.1007/s10008-022-05326-4.

[140] H. Q. V. Nguyen, J. Nerut, H. Kasuk, T. Thomberg, T. Romann, J. Aruvali, M. Külaviir, P. Paaver, Z. Kochovski, E. Härk, E. Lust, ECS Adv. (**2024**) DOI: 10.1149/2754-2734/ad456c.

[141] D. Zhang, H. Fu, L. Shi, C. Pan, Q. Li, Y. Chu, W. Yu, Inorg. Chem. 46 (**2007**) 2446–2451. DOI: 10.1021/ic061697d.

[142] H. Q. V. Nguyen, J. Nerut, H. Kasuk, T. Thomberg, T. Romann, J. Aruväli, E. Lust, ECS Trans. 111 (**2023**) 17. DOI: 10.1149/11105.0017ecst.

[143] J. Quinson, M. Inaba, S. Neumann, A. A. Swane, J. Bucher, S. B. Simonsen, L. Theil Kuhn, J. J. K. Kirkensgaard, K. M. Ø. Jensen, M. Oezaslan, S. Kunz, M. Arenz, ACS Catal. 8 (**2018**) 6627–6635. DOI: 10.1021/acscatal.8b00694.

[144] D. Balzar, in: R. L. Snyder, J. Fiala, H. J. Bunge (Eds.), *Defect and Microstructure Analysis by Diffraction*, International Union of Crystallography, Oxford, **1999**, p 785.

[145] P. I. Ravikovitch, A. V. Neimark, Colloids Surf. A 187-188 (**2001**) 11–21. DOI: 10.1016/S0927-7757(01)00614-8.

[146] Y. Garsany, O. A. Baturina, K. E. Swider-Lyons, S. S. Kocha, Anal. Chem. 82 (**2010**) 6321–6328. DOI: 10.1021/ac100306c.

[147] F. Dionigi, C. C. Weber, M. Primbs, M. Gocyla, A. M. Bonastre, C. Spöri, H. Schmies, E. Hornberger, S. Kühl, J. Drnec, M. Heggen, J. Sharman, R. E. Dunin-Borkowski, P. Strasser, Nano Lett. 19 (**2019**) 6876–6885. DOI: 10.1021/acs.nanolett.9b02116.

[148] H. Schulenburg, J. Durst, E. Müller, A. Wokaun, G. G. Scherer, J. Electroanal. Chem. 642 (**2010**) 52–60. DOI: 10.1016/j.jelechem.2010.02.005.

[149] F. A. Adekola, C. Colin, D. Bauer, Electrochim. Acta 37 (**1992**) 507–512. DOI: 10.1016/0013-4686(92)87043-Y.

[150] A. G. Bannov, M. V. Popov, P. B. Kurmashov, J. Therm. Anal. Calorim. 142 (**2020**) 349–370. DOI: 10.1007/s10973-020-09647-2.

[151] K. Hirota, K. Mitani, M. Yoshinaka, O. Yamaguchi, Mater. Sci. Eng. A 399 (**2005**) 154–160. DOI: 10.1016/j.msea.2005.02.062.

[152] Z. Zhao, H. Zheng, Y. Wang, S. Mao, J. Niu, Y. Chen, M. Shang, Int. J. Refract. Met. Hard Mater. 29 (**2011**) 614–617. DOI: 10.1016/j.ijrmhm.2011.04.007.

[153] R. L. McCreery, Chem. Rev. 108 (**2008**) 2646–2687. DOI: 10.1021/cr068076m.

[154] F. Lemont, A. Barbier, Hydrometallurgy 183 (**2019**) 193–198. DOI: 10.1016/j.hydromet.2018.12.009.

[155] P. Abellan, T. H. Moser, I. T. Lucas, J. W. Grate, J. E. Evans, N. D. Browning, RSC Adv. 7 (**2017**) 3831–3837. DOI: 10.1039/C6RA27066B.

[156] J. Park, Y. Oh, Y. Park, S. Nam, J. Moon, J. Kang, D.-R. Jung, S. Byun, B. Park, Curr. Appl. Phys. 11 (**2011**) S2–S5. DOI: 10.1016/j.cap.2011.07.005.

[157] Y. Wang, H. Liu, Z. Ma, Chin. J. Chem. Eng. 26 (**2018**) 2055–2063. DOI: 10.1016/j.cjche.2017.08.008.

[158] Y. Holade, C. Morais, K. Servat, T. W. Napporn, K. B. Kokoh, Phys. Chem. Chem. Phys. 16 (**2014**) 25609–25620. DOI: 10.1039/C4CP03851G.

[159] Y.-C. Wei, C.-W. Liu, W.-J. Chang, K.-W. Wang, Journal of Alloys and Compounds 509 (**2011**) 535–541. DOI: 10.1016/j.jallcom.2010.09.096.

[160] K. Vaarmets, P. Valk, J. Nerut, I. Tallo, J. Aruväli, S. Sepp, E. Lust, ECS Trans. 80 (**2017**) 743–755. DOI: 10.1149/08008.0743ecst.

[161] D.-M. Gu, Y.-Y. Chu, Z.-B. Wang, Z.-Z. Jiang, G.-P. Yin, Y. Liu, Appl. Catal. B: Environ. 102 (**2011**) 9–18. DOI: 10.1016/j.apcatb.2010.11.018.

[162] W. Huang, H. Wang, J. Zhou, J. Wang, P. N. Duchesne, D. Muir, P. Zhang, N. Han, F. Zhao, M. Zeng, J. Zhong, C. Jin, Y. Li, S.-T. Lee, H. Dai, Nat. Commun. 6 (**2015**) 10035. DOI: 10.1038/ncomms10035.

[163] L. Zhang, Y. Shen, ChemElectroChem 2 (**2015**) 887–895. DOI: 10.1002/celc.201402432.

[164] H. Yuan, D. Guo, X. Li, L. Yuan, W. Zhu, L. Chen, X. Qiu, Fuel Cells 9 (**2009**) 121–127. DOI: 10.1002/fuce.200800100.

[165] P. Ochal, J. L. Gomez de la Fuente, M. Tsypkin, F. Seland, S. Sunde, N. Muthuswamy, M. Rønning, D. Chen, S. Garcia, S. Alayoglu, B. Eichhorn, J. Electroanal. Chem. 655 (**2011**) 140–146. DOI: 10.1016/j.jelechem.2011.02.027.

[166] H. Q. V. Nguyen, J. Nerut, H. Kasuk, V. Grozovski, T. Thomberg, I. Tallo, R. Palm, M. Koppel, T. Romann, R. Härmas, J. Aruväli, M. Külaviir, E. Lust, Russ. J. Electrochem. 58 (**2022**) 781–797. DOI: 10.1134/S1023193522090130.

[167] K. Peng, N. Bhuvanendran, S. Ravichandran, W. Zhang, Q. Ma, L. Xing, Q. Xu, L. Khotseng, H. Su, Int. J. Hydrog. Energy 45 (**2020**) 22752–22760. DOI: 10.1016/j.ijhydene.2020.06.101.

9. SISUKOKKUVÕTE (SUMMARY IN ESTONIAN)

Süsinikule sadestatud Pt−CeO_2 katalüsaatorite väljatöötamine prootonvahetusmembraan kütuseelementidele

Kuna Euroopa on üleminekul säästvale ja rohelisele energiale, on vesinik lõimitud energiasüsteemi jaoks ülioluline. Vastavalt Euroopa Liidu (EL) energiasüsteemide lõimimise strateegiale (COM/2020/299) peab integratsioon hõlmama erinevaid energiakandjaid, nagu elekter, soojus, külm, gaasilised, tahked ja vedelkütused, kusjuures vesinik on dekarboniseeritud Euroopa energiasüsteemi alustalaks. Lisaks eeldab ELi vesinikualane strateegia (COM/2020/301), et lõppkasutaja nõudluse suurendamisel tuleb ammoniaagi ja metanooli tootmiseks kasutada vahetult vesinikku. Kuigi praegu on transpordisektori põhifookuses vesinikul töötavad kütuseelemendid ja vesinikutanklad, otsib EL kahtlemata alternatiivseid rohelisi kütuseid, mis on sünteesitud vesiniku baasil, nagu ammoniaak, metanool ja muud vedelad sünteetilised kütused. Selles valguses on oluline ka otsemetanool-kütuseelementide (DMFC) alane arendustöö. Metanooli kasutamisel transpordi sektoris on mõned eelised. ühe liitri metanooli energiasisaldus on 27 korda kõrgem kui vesiniku energiasisaldus rõhul 70 baari ning seetõttu võtab metanooli sisaldav kütusepaak oluliselt vähem ruumi. Ka võib metanooli pidada oluliselt kasutajasõbralikumaks kütuseks, sest seda on lihtsam hoiustada ja transportida kui vesinikku. Samas on hetkel jätkuvalt probleem DMFC anoodkatalüsaatori madal kasutegur ja ajaline stabiilsus.

Doktoritöös töötati välja metanooli oksüdeerimisreaktsiooni (MOR) ja hapniku redutseerimise reaktsiooni (ORR) uued süsinikule sadestatud Pt ja CeO_2 nanosakestel põhinevad komposiitkatalüsaatorid.

Selleks optimeeriti CeO_2 nanoosakeste sünteesi. Edukalt sünteesiti erineva kuju: lillekujulised ja hulknurksed, suuruse: 3,0 nm kuni 30 μm ja struktuuriga: kristallilised ja amorfsed CeO_2 osakesed. Leiti, et ultraheli ja mikrolainete rakendamisel põhinevate meetodite parameetrid ei mõjutanud olulisel määral sünteesitud CeO_2 nanoosakeste füsiko-keemilisi omadusi.

Pt nanoosakeste sünteesiks ja sadestamiseks kasutati etüleenglükooli redutseerimismeetodit. Kusjuures etüleenglükool oli nii reaktsioonikeskkond kui ka redutseerija. Leiti, et glükolaat-anioonide tekitamine reaktsioonisegus enne etüleenglükooliga redutseerimist muutis Pt nanoosakeste füüsikalisi omadusi ja suurendas Pt−CeO_2/C katalüsaatorite elektrokeemilist aktiivsust. Sünteesis kasutati Pt nanoosakeste tekke esilekutsumiseks kolme ergastusmeetodit: reaktsioonisegu ultrahelitöötlus, süntees mikrolaineahjus ning reaktsioonisegu kuumutamine õlivannil. Ultrahelitöötluse ja mikrolainete kiirguse kestvus mõjutas ainult mõnevõrra Pt nanoosakeste omadusi. Pikem mikrolainetöötlus põhjustas Pt nanoosakeste aglomeerumist süsiniku osakeste pinnal, samas kui pikem reaktsioonisegu kuumutamine õlivannil põhjustas Pt nanoosakeste kasvu. Katalüsaatori kandja (kommertsiaalne süsiniktahm Ketjenblack või

kroomkarbiidist sünteesitud süsinik) ja reagentide (naatrium-, hüdroksiid-, heksakloroplatinaat- ja glükolaatioonid) kontsentratsioonid reaktsioonisegus mõjutasid sünteesitud $Pt{-}CeO_2/C$ komplekskatalüsaatori füüsikalisi omadusi ja elektrokeemilist aktiivsust. Pt ja CeO_2 nanoosakeste sadestamiseks süsinikkandaje pinnale kasutati mitmesuguseid strateegiaid: erinevate erastusmeetodite kombineerimine, pH järsk muutmine ja tugevamate redutseerivate reagentide kasutamine. Optimaalsete sünteesitingimuste rakendamisel oli Pt nanoosakeste keskmine läbimõõt umbes 3,0 nm ja Pt nanoosakesed ei olnud transmissioonelektronmikroskoopia piltide järgi aglomeerunud.

Leiti, et karbiidset päritolu süsinikalusmaterjalid on sobilikud rakendamiseks prootovahetusmembraaniga kütuseelementides. Kroomkarbiidset päritolu süsinikel oli mikro-mesopoorne struktuur ning karbiidset päritolu süsiniku sünteesitemperatuur mõjutas märkimisväärselt süsiniku kristallograafilist struktuuri sealhulgas grafitiseerumisastet ning mikro- ja mesopooride ruumala. Kui kroom(II)karbiidist temperatuuril 900 °C sünteesitud süsinikku $C(Cr_3C_2)$ kasutati katalüsaatori alusmaterjalina, siis suurenesid nii $Pt{-}CeO_2$ kui ka Pt katalüsaatorite MOR ja ORR aktiivsuse. Kõige paljutõotavam katalüsaator oli alusmaterjalile $C(Cr_3C_2)$ sadestatud Pt katalüsaator, mis saavutas väga kõrge MOR aktiivsuse. Alusmaterjalile $C(Cr_3C_2)$ sadestatud Pt katalüsaatori MOR aktiivsus potentsiaalil 0,85 V (pöörduva vesinikelektroodi suhtes) oli sama hea kui kommertsiaalsele süsiniktahmale Ketjenblack sadestatud $Pt{-}CeO_2$ katalüsaatoril.

Vesiniku järeltöötlus pärast EG redutseerimissünteesi muutis $Pt{-}CeO_2/C$ katalüsaatorite füüsilisi omadusi. Vesiniku järeltöötlus parandas teatud $Pt{-}CeO_2/C$ materjalide MOR aktiivsust ja ajalist stabiilsust. See võis olla põhjustatud metallise Pt osakaalu suurenemisest katalüsaatoris. Teisalt vähenes $PtCe_{H_3PO_4}$ katalüüsitori MOR aktiivsus pärast vesiniku järeltöötlust märkimisväärselt. $PtCe_{H_3PO_4}$ katalüsaator oli Pt-põhine katalüsaator ning sisaldas nii CeO_2 kui ka $CePO_4$ nanoosakesi. Elektrokeemilise aktiivsuse vähenemine oli oodatud tulemus, kuna vesiniku järeltöötlus lõhkus $PtCe_{H_3PO_4}$ materjali fluoriitse struktuuri. Seega kadus ka Pt nanososkeste ja tseriumühendite kontaktist tingitud sünergistlik efekt.

10. ACKNOWLEDGEMENTS

I am proud of my attainment of a doctorate degree in philosophy of chemistry at the Institute of Chemistry, University of Tartu. This achievement is the most significant milestone in my academic journey. I'm immensely grateful for these years of research that have enriched me much valuable knowledge, little by little progress and unforgettable memories.

I would like to thank my supervisors, Prof. Enn Lust, Prof. Jaak Nerut and Dr Heili Kasuk, for their invaluable support throughout my studies. The dedicated presence of Prof. Enn Lust in the office, even on weekends or during non-working hours, has been inspiring. His lifelong commitment to science has left a lasting impact on my future academic career. I got acquainted with my two other supervisors while in my Master's program at the University of Tartu. When I started working with Prof. Jaak Nerut, he has consistently shown dedication and enthusiasm in research, a strong commitment and calmness in trouble. He gave me many valuable guidances, advice and reviews, which helped me enhance my research abilities day by day. Dr Heili Kasuk also plays an important role in this journey. Thanks for being a consistently reliable presence and offering assistance whenever I struggle with academics. Lastly, thank you so much to my three supervisors for all their support.

I also want to thank my parents in Vietnam for all your sacrifices, unconditional support, strong belief in me, and encouragement in my journey of maturity to this point. I would like to thank my wife, Thao Pham, for her constant support through rough patches and good times. Your meal saved me from starving during late-night work. Thank you for tidying up our apartment when I am busy with my deadlines. I adopted a fresh perspective to view my life events during our accompany. Besides, our little dog, Mun, often disrupts me when I am working at home, but she brings a new colour to our home.

Nevertheless, I would like to thank my opponent, Asst. Prof. Jonathan Quinson, Aarhus University, for spending his time reviewing my dissertation. In addition, his presence (in person) at my doctoral defence is my great honour.

I would like to acknowledge all my dedicated colleagues Dr Kersti Vaarmets, Dr Rasmus Palm, Dr Peeter Valk, Dr Patrick Teppor, Ms Miriam Koppel, Dr Jaan Aruvati, Assoc. Prof. Thomas Thomberg, Dr Tavo Romann, Dr Meelis Härmas, Dr Riinu Härmas, Dr Mirian Külaviir, Dr Peeter Paaver, Dr Ove Korjus, Dr Eneli Härk, Dr. Zdravko Kochovski, Dr Olga Volobujeva, and Mr Karl-Ander Kasuk who have been supportive collaborators throughout my doctoral journey. Thank my office companions for making my years in the Institute of Chemistry become a memorial.

During the time in Estonia, I'm very grateful to have small Vietnamese community in Estonia, e.g. Ngan Bui, Tram Nguyen, Thai Nguyen, Nga Vu, Quan Tran, Ha Nguyen, Trang Nguyen, Dong Bui, Phuong Nguyen, Bao Nguyen, Huyen Pham, Linh Nguyen, Dam Tran, Ty Tran, Dong Bui, Nhung

Dang and Anh Vu. Their presence improves my social life during the stay and share the joyfulness. I feel the warmth through the cold winter seasons with my small circle, especially the support of friends through the hardships is precious. I would like to thank Dr Carolin Siimenson, Assoc. Liis Siinor, Dr Piret Pikma, and Dr Jinfeng Zhao for the occasional invitation to social activities in the town. I would like to thank my old friends, Thang Bui, Bien Trinh, Tho Le, Vo Nguyen, İsmail Sarıgül and Aravindan Sooryanarain, for hanging out and having good conversations.

This work was supported by:

- Estonian Research Council (Proof-of-Concept Grant EAG273),
- Project ”Increasing the knowledge intensity of Ida-Viru entrepreneurship” co-funded by the European Union (ÕÜF1),
- Estonian Ministry of Education and Research (Center of Excellence TK210 and TK141),
- Personal Research Grant PRG676.

11. PUBLICATIONS

CURRICULUM VITAE

Name:	Huy Quí Vinh Nguyen
Date of birth:	April 04th, 1992
Citizenship:	Vietnam
Contact:	Institute of Chemistry, University of Tartu Ravila 14a, 50411, Tartu, Estonia
Email:	vinh.nguyen@ut.ee nhqvinh92@gmail.com

Education:

2019–...	University of Tartu, Institute of Chemistry, Ph.D. studies (Chemistry)
2017–2019	University of Tartu, Institute of Chemistry, M.Sc. (Applied Measurement Science)
2010–2016	International University - Vietnam National University HCM City, BE. (Food Technology)

Professional Employments:

2023–...	University of Tartu, Institute of Chemistry, Chemist
2019–2019	University of Tartu, Institute of Chemistry, Chemist

Scientific Publications:

- **H. Q. V. Nguyen**, J. Nerut, H. Kasuk, T. Thomas, T. Romann, J. Aruväli, M. Külaviir, P. Paaver, Z. Kochovski, E. Härk and E. Lust, Influence of Chromium Carbide-Derived Carbon and Ceria Nanocrystals on Pt−CeO_2/C Catalysts for Fuel Cell Application, *ECS Adv.* 3 (2024) 024505.
- **H. Q. V. Nguyen**, J. Nerut, H. Kasuk, T. Thomas, T. Romann, J. Aruväli, and E. Lust, Ultra-Small Ceria Nanocrystals at Carbon Surface Synthesized by Ultrasound Sonication: A Study of Highly Active Platinum-Cerium Bifunctional Catalysts for Methanol Oxidation and Oxygen Reduction, *ECS Trans.* 5 (2023) 17.
- **H. Q. V. Nguyen**, J. Nerut, H. Kasuk, M. Härmas, P. Valk, T. Romann, M. Koppel, P. Teppor, J. Aruväli, O. Korjus, O. Volobujeva, and E. Lust, Optimisation of The Ethylene Glycol Reduction Method for The Synthesis of Platinum-Ceria-Carbon Materials as Catalysts for The Methanol Oxidation Reaction, *J. Solid State Electrochem.* 27 (2023) 313-326.
- **H. Q. V. Nguyen**, J. Nerut, H. Kasuk, V. Grozovski, T. Thomberg, I. Tallo, R. Palm, M. Koppel, T. Romann, J. Aruväli, M. Külaviir, and E. Lust, Oxygen Reduction Reaction on Chromium Carbide-Derived Carbons, *Russ. J. Electrochem.* 58 (2022) 781-797.

- **H. Q. V. Nguyen**, J. Nerut, H. Kasuk, P. Valk, M. Härmas, J. Aruväli, and E. Lust, Methanol Oxidation Reaction on Platinum Catalysts Deposited onto Ceria-Carbon Substrate, *EFSF2021* Zenodo (2022). DOI: 10.5281/zenodo.7264933

Participation in International Conferences:

- **H. Q. V. Nguyen**, H. Kasuk, M. Härmas, J. Aruväli, O. Volobujeva, E. Härk, Z. Kochovski, E. Lust, J. Nerut, Hydrogen Post-Treatment Enhances the Electrochemical Activity of Carbon-Supported Pt-CeO_2 Catalysts, 8th Baltic Electrochemistry Conference; Tartu, Estonia; April 14th – 17th, 2024 (**oral presentation**).
- **H. Q. V. Nguyen**, J. Nerut, H. Kasuk, T. Thomberg, T. Romann, J. Aruväli, and E. Lust, Ultra-Small Ceria Nanocrystals at Carbon Surface synthesized by Ultrasound Sonication: A Study of Highly Active Platinum-Cerium Bifunctional Catalysts for Methanol Oxidation and Oxygen Reduction, 243rd Electrochemical Society Meeting, Boston, MA, USA, May 28th – June 2nd, 2023 (**oral presentation**).
- **H. Q. V. Nguyen**, J. Nerut, H. Kasuk, P. Valk, M. Härmas, J. Aruväli, and E. Lust, Methanol Oxidation Reaction (MOR) on Platinum Catalysts Deposited onto Ceria-Carbon Substrate, 25th European Fuel Cell Forum 2021 (EFSF2021), Lucerne, Switzerland, June 29th – July 2nd, 2021 (**oral presentation**).
- **H. Q. V. Nguyen**, H. Kasuk, J. Nerut, T. Thomberg, J. Aruväli, Oxygen Reduction on Platinum Nanoparticles Deposited onto Chromium Carbide Derived Carbon Support, 7th Batic Electrochemistry Conference, Tartu, Estonia, November 4th – 7th, 2018 (**poster presentation**)

ELULOOKIRJELDUS

Nimi:	Huy Quí Vinh Nguyen
Sünniaeg:	04 Aprill, 1992
Kodakondsus:	Vietnami
Kontakt:	Tartu Ülikool keemia instituut Ravila 14a, 50411, Tartu, Eesti
E-post:	vinh.nguyen@ut.ee nhqvinh92@gmail.com

Haridus:

2019–...	Tartu Ülikool keemia instituut, doktoriõpe (keemia)
2017–2019	Tartu Ülikool keemia instituut, M.Sc. (rakenduslik mõõteteadus)
2010–2016	International University - Vietnam National University HCM City, BE. (toidutehnoloogia)

Teenistuskäik:

2023–...	Tartu Ülikool keemia instituu, keemik
2019–2019	Tartu Ülikool keemia instituu, keemik

Teaduspublikatsioonid:

- **H. Q. V. Nguyen**, J. Nerut, H. Kasuk, T. Thomas, T. Romann, J. Aruväli, M. Külaviir, P. Paaver, Z. Kochovski, E. Härk and E. Lust, Influence of Chromium Carbide-Derived Carbon and Ceria Nanocrystals on Pt−CeO_2/C Catalysts for Fuel Cell Application, *ECS Adv.* 3 (2024) 024505.
- **H. Q. V. Nguyen**, J. Nerut, H. Kasuk, T. Thomas, T. Romann, J. Aruväli, and E. Lust, Ultra-Small Ceria Nanocrystals at Carbon Surface Synthesized by Ultrasound Sonication: A Study of Highly Active Platinum-Cerium Bifunctional Catalysts for Methanol Oxidation and Oxygen Reduction, *ECS Trans.* 5 (2023) 17.
- **H. Q. V. Nguyen**, J. Nerut, H. Kasuk, M. Härmas, P. Valk, T. Romann, M. Koppel, P. Teppor, J. Aruväli, O. Korjus, O. Volobujeva, and E. Lust, Optimisation of The Ethylene Glycol Reduction Method for The Synthesis of Platinum-Ceria-Carbon Materials as Catalysts for The Methanol Oxidation Reaction, *J. Solid State Electrochem.* 27 (2023) 313-326.
- **H. Q. V. Nguyen**, J. Nerut, H. Kasuk, V. Grozovski, T. Thomberg, I. Tallo, R. Palm, M. Koppel, T. Romann, J. Aruväli, M. Külaviir, and E. Lust, Oxygen Reduction Reaction on Chromium Carbide-Derived Carbons, *Russ. J. Electrochem.* 58 (2022) 781-797.

- **H. Q. V. Nguyen**, J. Nerut, H. Kasuk, P. Valk, M. Härmas, J. Aruväli, and E. Lust, Methanol Oxidation Reaction on Platinum Catalysts Deposited onto Ceria-Carbon Substrate, *EFSF2021* Zenodo (2022). DOI: 10.5281/zenodo.7264933

Rahvusvahelistel konverentsidel osalemine:

- **H. Q. V. Nguyen**, H. Kasuk, M. Härmas, J. Aruväli, O. Volobujeva, E. Härk, Z. Kochovski, E. Lust, J. Nerut, Hydrogen Post-Treatment Enhances the Electrochemical Activity of Carbon-Supported Pt-CeO_2 Catalysts, 8th Baltic Electrochemistry Conference, Tartu, Estonia, April 14 – 17th, 2024 (**suuline ettekanne**).
- **H. Q. V. Nguyen**, J. Nerut, H. Kasuk, T. Thomberg, T. Romann, J. Aruväli, and E. Lust, Ultra-Small Ceria Nanocrystals at Carbon Surface synthesized by Ultrasound Sonication: A Study of Highly Active Platinum-Cerium Bifunctional Catalysts for Methanol Oxidation and Oxygen Reduction, 243rd Electrochemical Society Meeting, Boston, MA, USA, May 28th – June 2nd, 2023 (**suuline ettekanne**).
- **H. Q. V. Nguyen**, J. Nerut, H. Kasuk, P. Valk, M. Härmas, J. Aruväli, and E. Lust, Methanol Oxidation Reaction (MOR) on Platinum Catalysts Deposited onto Ceria-Carbon Substrate, 25th European Fuel Cell Forum 2021 (EFSF2021), Lucerne, Switzerland, June 29th – July 2nd, 2021 (**suuline ettekanne**).
- **H. Q. V. Nguyen**, H. Kasuk, J. Nerut, T. Thomberg, J. Aruväli, Oxygen Reduction on Platinum Nanoparticles Deposited onto Chromium Carbide Derived Carbon Support, 7th Batic Electrochemistry Conference, Tartu, Estonia, November 4th – 7th, 2018 (**poster ettekanne**)

DISSERTATIONES CHIMICAE UNIVERSITATIS TARTUENSIS

1. **Toomas Tamm.** Quantum-chemical simulation of solvent effects. Tartu, 1993, 110 p.
2. **Peeter Burk.** Theoretical study of gas-phase acid-base equilibria. Tartu, 1994, 96 p.
3. **Victor Lobanov.** Quantitative structure-property relationships in large descriptor spaces. Tartu, 1995, 135 p.
4. **Vahur Mäemets.** The ^{17}O and ^{1}H nuclear magnetic resonance study of H_2O in individual solvents and its charged clusters in aqueous solutions of electrolytes. Tartu, 1997, 140 p.
5. **Andrus Metsala.** Microcanonical rate constant in nonequilibrium distribution of vibrational energy and in restricted intramolecular vibrational energy redistribution on the basis of slater's theory of unimolecular reactions. Tartu, 1997, 150 p.
6. **Uko Maran.** Quantum-mechanical study of potential energy surfaces in different environments. Tartu, 1997, 137 p.
7. **Alar Jänes.** Adsorption of organic compounds on antimony, bismuth and cadmium electrodes. Tartu, 1998, 219 p.
8. **Kaido Tammeveski.** Oxygen electroreduction on thin platinum films and the electrochemical detection of superoxide anion. Tartu, 1998, 139 p.
9. **Ivo Leito.** Studies of Brønsted acid-base equilibria in water and non-aqueous media. Tartu, 1998, 101 p.
10. **Jaan Leis.** Conformational dynamics and equilibria in amides. Tartu, 1998, 131 p.
11. **Toonika Rinken.** The modelling of amperometric biosensors based on oxidoreductases. Tartu, 2000, 108 p.
12. **Dmitri Panov.** Partially solvated Grignard reagents. Tartu, 2000, 64 p.
13. **Kaja Orupõld.** Treatment and analysis of phenolic wastewater with microorganisms. Tartu, 2000, 123 p.
14. **Jüri Ivask.** Ion Chromatographic determination of major anions and cations in polar ice core. Tartu, 2000, 85 p.
15. **Lauri Vares.** Stereoselective Synthesis of Tetrahydrofuran and Tetrahydropyran Derivatives by Use of Asymmetric Horner-Wadsworth-Emmons and Ring Closure Reactions. Tartu, 2000, 184 p.
16. **Martin Lepiku.** Kinetic aspects of dopamine D_2 receptor interactions with specific ligands. Tartu, 2000, 81 p.
17. **Katrin Sak.** Some aspects of ligand specificity of P2Y receptors. Tartu, 2000, 106 p.
18. **Vello Pällin.** The role of solvation in the formation of iotsitch complexes. Tartu, 2001, 95 p.
19. **Katrin Kollist.** Interactions between polycyclic aromatic compounds and humic substances. Tartu, 2001, 93 p.

20. **Ivar Koppel.** Quantum chemical study of acidity of strong and superstrong Brønsted acids. Tartu, 2001, 104 p.
21. **Viljar Pihl.** The study of the substituent and solvent effects on the acidity of OH and CH acids. Tartu, 2001, 132 p.
22. **Natalia Palm.** Specification of the minimum, sufficient and significant set of descriptors for general description of solvent effects. Tartu, 2001, 134 p.
23. **Sulev Sild.** QSPR/QSAR approaches for complex molecular systems. Tartu, 2001, 134 p.
24. **Ruslan Petrukhin.** Industrial applications of the quantitative structure-property relationships. Tartu, 2001, 162 p.
25. **Boris V. Rogovoy.** Synthesis of (benzotriazolyl)carboximidamides and their application in relations with *N*- and *S*-nucleophyles. Tartu, 2002, 84 p.
26. **Koit Herodes.** Solvent effects on UV-vis absorption spectra of some solvatochromic substances in binary solvent mixtures: the preferential solvation model. Tartu, 2002, 102 p.
27. **Anti Perkson.** Synthesis and characterisation of nanostructured carbon. Tartu, 2002, 152 p.
28. **Ivari Kaljurand.** Self-consistent acidity scales of neutral and cationic Brønsted acids in acetonitrile and tetrahydrofuran. Tartu, 2003, 108 p.
29. **Karmen Lust.** Adsorption of anions on bismuth single crystal electrodes. Tartu, 2003, 128 p.
30. **Mare Piirsalu.** Substituent, temperature and solvent effects on the alkaline hydrolysis of substituted phenyl and alkyl esters of benzoic acid. Tartu, 2003, 156 p.
31. **Meeri Sassian.** Reactions of partially solvated Grignard reagents. Tartu, 2003, 78 p.
32. **Tarmo Tamm.** Quantum chemical modelling of polypyrrole. Tartu, 2003. 100 p.
33. **Erik Teinemaa.** The environmental fate of the particulate matter and organic pollutants from an oil shale power plant. Tartu, 2003. 102 p.
34. **Jaana Tammiku-Taul.** Quantum chemical study of the properties of Grignard reagents. Tartu, 2003. 120 p.
35. **Andre Lomaka.** Biomedical applications of predictive computational chemistry. Tartu, 2003. 132 p.
36. **Kostyantyn Kirichenko.** Benzotriazole – Mediated Carbon–Carbon Bond Formation. Tartu, 2003. 132 p.
37. **Gunnar Nurk.** Adsorption kinetics of some organic compounds on bismuth single crystal electrodes. Tartu, 2003, 170 p.
38. **Mati Arulepp.** Electrochemical characteristics of porous carbon materials and electrical double layer capacitors. Tartu, 2003, 196 p.
39. **Dan Cornel Fara.** QSPR modeling of complexation and distribution of organic compounds. Tartu, 2004, 126 p.
40. **Riina Mahlapuu.** Signalling of galanin and amyloid precursor protein through adenylate cyclase. Tartu, 2004, 124 p.

41. **Mihkel Kerikmäe.** Some luminescent materials for dosimetric applications and physical research. Tartu, 2004, 143 p.
42. **Jaanus Kruusma.** Determination of some important trace metal ions in human blood. Tartu, 2004, 115 p.
43. **Urmas Johanson.** Investigations of the electrochemical properties of polypyrrole modified electrodes. Tartu, 2004, 91 p.
44. **Kaido Sillar.** Computational study of the acid sites in zeolite ZSM-5. Tartu, 2004, 80 p.
45. **Aldo Oras.** Kinetic aspects of dATPαS interaction with $P2Y_1$ receptor. Tartu, 2004, 75 p.
46. **Erik Mölder.** Measurement of the oxygen mass transfer through the air-water interface. Tartu, 2005, 73 p.
47. **Thomas Thomberg.** The kinetics of electroreduction of peroxodisulfate anion on cadmium (0001) single crystal electrode. Tartu, 2005, 95 p.
48. **Olavi Loog.** Aspects of condensations of carbonyl compounds and their imine analogues. Tartu, 2005, 83 p.
49. **Siim Salmar.** Effect of ultrasound on ester hydrolysis in aqueous ethanol. Tartu, 2006, 73 p.
50. **Ain Uustare.** Modulation of signal transduction of heptahelical receptors by other receptors and G proteins. Tartu, 2006, 121 p.
51. **Sergei Yurchenko.** Determination of some carcinogenic contaminants in food. Tartu, 2006, 143 p.
52. **Kaido Tämm.** QSPR modeling of some properties of organic compounds. Tartu, 2006, 67 p.
53. **Olga Tšubrik.** New methods in the synthesis of multisubstituted hydrazines. Tartu. 2006, 183 p.
54. **Lilli Sooväli.** Spectrophotometric measurements and their uncertainty in chemical analysis and dissociation constant measurements. Tartu, 2006, 125 p.
55. **Eve Koort.** Uncertainty estimation of potentiometrically measured ph and pK_a values. Tartu, 2006, 139 p.
56. **Sergei Kopanchuk.** Regulation of ligand binding to melanocortin receptor subtypes. Tartu, 2006, 119 p.
57. **Silvar Kallip.** Surface structure of some bismuth and antimony single crystal electrodes. Tartu, 2006, 107 p.
58. **Kristjan Saal.** Surface silanization and its application in biomolecule coupling. Tartu, 2006, 77 p.
59. **Tanel Tätte.** High viscosity $Sn(OBu)_4$ oligomeric concentrates and their applications in technology. Tartu, 2006, 91 p.
60. **Dimitar Atanasov Dobchev**. Robust QSAR methods for the prediction of properties from molecular structure. Tartu, 2006, 118 p.
61. **Hannes Hagu**. Impact of ultrasound on hydrophobic interactions in solutions. Tartu, 2007, 81 p.
62. **Rutha Jäger.** Electroreduction of peroxodisulfate anion on bismuth electrodes. Tartu, 2007, 142 p.

63. **Kaido Viht.** Immobilizable bisubstrate-analogue inhibitors of basophilic protein kinases: development and application in biosensors. Tartu, 2007, 88 p.
64. **Eva-Ingrid Rõõm.** Acid-base equilibria in nonpolar media. Tartu, 2007, 156 p.
65. **Sven Tamp.** DFT study of the cesium cation containing complexes relevant to the cesium cation binding by the humic acids. Tartu, 2007, 102 p.
66. **Jaak Nerut.** Electroreduction of hexacyanoferrate(III) anion on Cadmium (0001) single crystal electrode. Tartu, 2007, 180 p.
67. **Lauri Jalukse.** Measurement uncertainty estimation in amperometric dissolved oxygen concentration measurement. Tartu, 2007, 112 p.
68. **Aime Lust.** Charge state of dopants and ordered clusters formation in CaF_2:Mn and CaF_2:Eu luminophors. Tartu, 2007, 100 p.
69. **Iiris Kahn**. Quantitative Structure-Activity Relationships of environmentally relevant properties. Tartu, 2007, 98 p.
70. **Mari Reinik.** Nitrates, nitrites, N-nitrosamines and polycyclic aromatic hydrocarbons in food: analytical methods, occurrence and dietary intake. Tartu, 2007, 172 p.
71. **Heili Kasuk.** Thermodynamic parameters and adsorption kinetics of organic compounds forming the compact adsorption layer at Bi single crystal electrodes. Tartu, 2007, 212 p.
72. **Erki Enkvist.** Synthesis of adenosine-peptide conjugates for biological applications. Tartu, 2007, 114 p.
73. **Svetoslav Hristov Slavov**. Biomedical applications of the QSAR approach. Tartu, 2007, 146 p.
74. **Eneli Härk.** Electroreduction of complex cations on electrochemically polished Bi(*hkl*) single crystal electrodes. Tartu, 2008, 158 p.
75. **Priit Möller.** Electrochemical characteristics of some cathodes for medium temperature solid oxide fuel cells, synthesized by solid state reaction technique. Tartu, 2008, 90 p.
76. **Signe Viggor.** Impact of biochemical parameters of genetically different pseudomonads at the degradation of phenolic compounds. Tartu, 2008, 122 p.
77. **Ave Sarapuu.** Electrochemical reduction of oxygen on quinone-modified carbon electrodes and on thin films of platinum and gold. Tartu, 2008, 134 p.
78. **Agnes Kütt.** Studies of acid-base equilibria in non-aqueous media. Tartu, 2008, 198 p.
79. **Rouvim Kadis.** Evaluation of measurement uncertainty in analytical chemistry: related concepts and some points of misinterpretation. Tartu, 2008, 118 p.
80. **Valter Reedo.** Elaboration of IVB group metal oxide structures and their possible applications. Tartu, 2008, 98 p.
81. **Aleksei Kuznetsov.** Allosteric effects in reactions catalyzed by the cAMP-dependent protein kinase catalytic subunit. Tartu, 2009, 133 p.

82. **Aleksei Bredihhin.** Use of mono- and polyanions in the synthesis of multisubstituted hydrazine derivatives. Tartu, 2009, 105 p.
83. **Anu Ploom.** Quantitative structure-reactivity analysis in organosilicon chemistry. Tartu, 2009, 99 p.
84. **Argo Vonk.** Determination of adenosine A_{2A}- and dopamine D_1 receptor-specific modulation of adenylate cyclase activity in rat striatum. Tartu, 2009, 129 p.
85. **Indrek Kivi.** Synthesis and electrochemical characterization of porous cathode materials for intermediate temperature solid oxide fuel cells. Tartu, 2009, 177 p.
86. **Jaanus Eskusson.** Synthesis and characterisation of diamond-like carbon thin films prepared by pulsed laser deposition method. Tartu, 2009, 117 p.
87. **Marko Lätt.** Carbide derived microporous carbon and electrical double layer capacitors. Tartu, 2009, 107 p.
88. **Vladimir Stepanov.** Slow conformational changes in dopamine transporter interaction with its ligands. Tartu, 2009, 103 p.
89. **Aleksander Trummal.** Computational Study of Structural and Solvent Effects on Acidities of Some Brønsted Acids. Tartu, 2009, 103 p.
90. **Eerold Vellemäe.** Applications of mischmetal in organic synthesis. Tartu, 2009, 93 p.
91. **Sven Parkel.** Ligand binding to 5-HT_{1A} receptors and its regulation by Mg^{2+} and Mn^{2+}. Tartu, 2010, 99 p.
92. **Signe Vahur.** Expanding the possibilities of ATR-FT-IR spectroscopy in determination of inorganic pigments. Tartu, 2010, 184 p.
93. **Tavo Romann**. Preparation and surface modification of bismuth thin film, porous, and microelectrodes. Tartu, 2010, 155 p.
94. **Nadežda Aleksejeva.** Electrocatalytic reduction of oxygen on carbon nanotube-based nanocomposite materials. Tartu, 2010, 147 p.
95. **Marko Kullapere.** Electrochemical properties of glassy carbon, nickel and gold electrodes modified with aryl groups. Tartu, 2010, 233 p.
96. **Liis Siinor.** Adsorption kinetics of ions at Bi single crystal planes from aqueous electrolyte solutions and room-temperature ionic liquids. Tartu, 2010, 101 p.
97. **Angela Vaasa.** Development of fluorescence-based kinetic and binding assays for characterization of protein kinases and their inhibitors. Tartu 2010, 101 p.
98. **Indrek Tulp.** Multivariate analysis of chemical and biological properties. Tartu 2010, 105 p.
99. **Aare Selberg.** Evaluation of environmental quality in Northern Estonia by the analysis of leachate. Tartu 2010, 117 p.
100. **Darja Lavõgina.** Development of protein kinase inhibitors based on adenosine analogue-oligoarginine conjugates. Tartu 2010, 248 p.
101. **Laura Herm.** Biochemistry of dopamine D_2 receptors and its association with motivated behaviour. Tartu 2010, 156 p.

102. **Terje Raudsepp.** Influence of dopant anions on the electrochemical properties of polypyrrole films. Tartu 2010, 112 p.
103. **Margus Marandi.** Electroformation of Polypyrrole Films: *In-situ* AFM and STM Study. Tartu 2011, 116 p.
104. **Kairi Kivirand.** Diamine oxidase-based biosensors: construction and working principles. Tartu, 2011, 140 p.
105. **Anneli Kruve.** Matrix effects in liquid-chromatography electrospray mass-spectrometry. Tartu, 2011, 156 p.
106. **Gary Urb.** Assessment of environmental impact of oil shale fly ash from PF and CFB combustion. Tartu, 2011, 108 p.
107. **Nikita Oskolkov.** A novel strategy for peptide-mediated cellular delivery and induction of endosomal escape. Tartu, 2011, 106 p.
108. **Dana Martin.** The QSPR/QSAR approach for the prediction of properties of fullerene derivatives. Tartu, 2011, 98 p.
109. **Säde Viirlaid.** Novel glutathione analogues and their antioxidant activity. Tartu, 2011, 106 p.
110. **Ülis Sõukand.** Simultaneous adsorption of Cd^{2+}, Ni^{2+}, and Pb^{2+} on peat. Tartu, 2011, 124 p.
111. **Lauri Lipping.** The acidity of strong and superstrong Brønsted acids, an outreach for the "limits of growth": a quantum chemical study. Tartu, 2011, 124 p.
112. **Heisi Kurig.** Electrical double-layer capacitors based on ionic liquids as electrolytes. Tartu, 2011, 146 p.
113. **Marje Kasari.** Bisubstrate luminescent probes, optical sensors and affinity adsorbents for measurement of active protein kinases in biological samples. Tartu, 2012, 126 p.
114. **Kalev Takkis.** Virtual screening of chemical databases for bioactive molecules. Tartu, 2012, 122 p.
115. **Ksenija Kisseljova**. Synthesis of aza-β^3-amino acid containing peptides and kinetic study of their phosphorylation by protein kinase A. Tartu, 2012, 104 p.
116. **Riin Rebane.** Advanced method development strategy for derivatization LC/ESI/MS. Tartu, 2012, 184 p.
117. **Vladislav Ivaništšev.** Double layer structure and adsorption kinetics of ions at metal electrodes in room temperature ionic liquids. Tartu, 2012, 128 p.
118. **Irja Helm.** High accuracy gravimetric Winkler method for determination of dissolved oxygen. Tartu, 2012, 139 p.
119. **Karin Kipper.** Fluoroalcohols as Components of LC-ESI-MS Eluents: Usage and Applications. Tartu, 2012, 164 p.
120. **Arno Ratas.** Energy storage and transfer in dosimetric luminescent materials. Tartu, 2012, 163 p.
121. **Reet Reinart-Okugbeni**. Assay systems for characterisation of subtype-selective binding and functional activity of ligands on dopamine receptors. Tartu, 2012, 159 p.

122. **Lauri Sikk.** Computational study of the Sonogashira cross-coupling reaction. Tartu, 2012, 81 p.
123. **Karita Raudkivi.** Neurochemical studies on inter-individual differences in affect-related behaviour of the laboratory rat. Tartu, 2012, 161 p.
124. **Indrek Saar.** Design of GalR2 subtype specific ligands: their role in depression-like behavior and feeding regulation. Tartu, 2013, 126 p.
125. **Ann Laheäär.** Electrochemical characterization of alkali metal salt based non-aqueous electrolytes for supercapacitors. Tartu, 2013, 127 p.
126. **Kerli Tõnurist.** Influence of electrospun separator materials properties on electrochemical performance of electrical double-layer capacitors. Tartu, 2013, 147 p.
127. **Kaija Põhako-Esko.** Novel organic and inorganic ionogels: preparation and characterization. Tartu, 2013, 124 p.
128. **Ivar Kruusenberg.** Electroreduction of oxygen on carbon nanomaterial-based catalysts. Tartu, 2013, 191 p.
129. **Sander Piiskop.** Kinetic effects of ultrasound in aqueous acetonitrile solutions. Tartu, 2013, 95 p.
130. **Ilona Faustova**. Regulatory role of L-type pyruvate kinase N-terminal domain. Tartu, 2013, 109 p.
131. **Kadi Tamm.** Synthesis and characterization of the micro-mesoporous anode materials and testing of the medium temperature solid oxide fuel cell single cells. Tartu, 2013, 138 p.
132. **Iva Bozhidarova Stoyanova-Slavova.** Validation of QSAR/QSPR for regulatory purposes. Tartu, 2013, 109 p.
133. **Vitali Grozovski**. Adsorption of organic molecules at single crystal electrodes studied by *in situ* STM method. Tartu, 2014, 146 p.
134. **Santa Veikšina**. Development of assay systems for characterisation of ligand binding properties to melanocortin 4 receptors. Tartu, 2014, 151 p.
135. **Jüri Liiv.** PVDF (polyvinylidene difluoride) as material for active element of twisting-ball displays. Tartu, 2014, 111 p.
136. **Kersti Vaarmets.** Electrochemical and physical characterization of pristine and activated molybdenum carbide-derived carbon electrodes for the oxygen electroreduction reaction. Tartu, 2014, 131 p.
137. **Lauri Tõntson**. Regulation of G-protein subtypes by receptors, guanine nucleotides and Mn^{2+}. Tartu, 2014, 105 p.
138. **Aiko Adamson.** Properties of amine-boranes and phosphorus analogues in the gas phase. Tartu, 2014, 78 p.
139. **Elo Kibena**. Electrochemical grafting of glassy carbon, gold, highly oriented pyrolytic graphite and chemical vapour deposition-grown graphene electrodes by diazonium reduction method. Tartu, 2014, 184 p.
140. **Teemu Näykki.** Novel Tools for Water Quality Monitoring – From Field to Laboratory. Tartu, 2014, 202 p.
141. **Karl Kaupmees.** Acidity and basicity in non-aqueous media: importance of solvent properties and purity. Tartu, 2014, 128 p.

142. **Oleg Lebedev**. Hydrazine polyanions: different strategies in the synthesis of heterocycles. Tartu, 2015, 118 p.
143. **Geven Piir.** Environmental risk assessment of chemicals using QSAR methods. Tartu, 2015, 123 p.
144. **Olga Mazina.** Development and application of the biosensor assay for measurements of cyclic adenosine monophosphate in studies of G protein-coupled receptor signalinga. Tartu, 2015, 116 p.
145. **Sandip Ashokrao Kadam.** Anion receptors: synthesis and accurate binding measurements. Tartu, 2015, 116 p.
146. **Indrek Tallo.** Synthesis and characterization of new micro-mesoporous carbide derived carbon materials for high energy and power density electrical double layer capacitors. Tartu, 2015, 148 p.
147. **Heiki Erikson.** Electrochemical reduction of oxygen on nanostructured palladium and gold catalysts. Tartu, 2015, 204 p.
148. **Erik Anderson.** *In situ* Scanning Tunnelling Microscopy studies of the interfacial structure between Bi(111) electrode and a room temperature ionic liquid. Tartu, 2015, 118 p.
149. **Girinath G. Pillai.** Computational Modelling of Diverse Chemical, Biochemical and Biomedical Properties. Tartu, 2015, 140 p.
150. **Piret Pikma.** Interfacial structure and adsorption of organic compounds at Cd(0001) and Sb(111) electrodes from ionic liquid and aqueous electrolytes: an *in situ* STM study. Tartu, 2015, 126 p.
151. **Ganesh babu Manoharan.** Combining chemical and genetic approaches for photoluminescence assays of protein kinases. Tartu, 2016, 126 p.
152. **Carolin Siimenson**. Electrochemical characterization of halide ion adsorption from liquid mixtures at Bi(111) and pyrolytic graphite electrode surface. Tartu, 2016, 110 p.
153. **Asko Laaniste.** Comparison and optimisation of novel mass spectrometry ionisation sources. Tartu, 2016, 156 p.
154. **Hanno Evard.** Estimating limit of detection for mass spectrometric analysis methods. Tartu, 2016, 224 p.
155. **Kadri Ligi.** Characterization and application of protein kinase-responsive organic probes with triplet-singlet energy transfer. Tartu, 2016, 122 p.
156. **Margarita Kagan.** Biosensing penicillins' residues in milk flows. Tartu, 2016, 130 p.
157. **Marie Kriisa.** Development of protein kinase-responsive photoluminescent probes and cellular regulators of protein phosphorylation. Tartu, 2016, 106 p.
158. **Mihkel Vestli.** Ultrasonic spray pyrolysis deposited electrolyte layers for intermediate temperature solid oxide fuel cells. Tartu, 2016, 156 p.
159. **Silver Sepp**. Influence of porosity of the carbide-derived carbon on the properties of the composite electrocatalysts and characteristics of polymer electrolyte fuel cells. Tartu, 2016, 137 p.
160. **Kristjan Haav**. Quantitative relative equilibrium constant measurements in supramolecular chemistry. Tartu, 2017, 158 p.

161. **Anu Teearu**. Development of MALDI-FT-ICR-MS methodology for the analysis of resinous materials. Tartu, 2017, 205 p.
162. **Taavi Ivan**. Bifunctional inhibitors and photoluminescent probes for studies on protein complexes. Tartu, 2017, 140 p.
163. **Maarja-Liisa Oldekop**. Characterization of amino acid derivatization reagents for LC-MS analysis. Tartu, 2017, 147 p.
164. **Kristel Jukk**. Electrochemical reduction of oxygen on platinum- and palladium-based nanocatalysts. Tartu, 2017, 250 p.
165. **Siim Kukk**. Kinetic aspects of interaction between dopamine transporter and *N*-substituted nortropane derivatives. Tartu, 2017, 107 p.
166. **Birgit Viira**. Design and modelling in early drug development in targeting HIV-1 reverse transcriptase and Malaria. Tartu, 2017, 172 p.
167. **Rait Kivi**. Allostery in cAMP dependent protein kinase catalytic subunit. Tartu, 2017, 115 p.
168. **Agnes Heering**. Experimental realization and applications of the unified acidity scale. Tartu, 2017, 123 p.
169. **Delia Juronen**. Biosensing system for the rapid multiplex detection of mastitis-causing pathogens in milk. Tartu, 2018, 85 p.
170. **Hedi Rahnel.** ARC-inhibitors: from reliable biochemical assays to regulators of physiology of cells. Tartu, 2018, 176 p.
171. **Anton Ruzanov.** Computational investigation of the electrical double layer at metal–aqueous solution and metal–ionic liquid interfaces. Tartu, 2018, 129 p.
172. **Katrin Kestav.** Crystal Structure-Guided Development of Bisubstrate-Analogue Inhibitors of Mitotic Protein Kinase Haspin. Tartu, 2018, 166 p.
173. **Mihkel Ilisson.** Synthesis of novel heterocyclic hydrazine derivatives and their conjugates. Tartu, 2018, 101 p.
174. **Anni Allikalt.** Development of assay systems for studying ligand binding to dopamine receptors. Tartu, 2018, 160 p.
175. **Ove Oll.** Electrical double layer structure and energy storage characteristics of ionic liquid based capacitors. Tartu, 2018, 187 p.
176. **Rasmus Palm.** Carbon materials for energy storage applications. Tartu, 2018, 114 p.
177. **Jörgen Metsik.** Preparation and stability of poly(3,4-ethylenedioxythiophene) thin films for transparent electrode applications. Tartu, 2018, 111 p.
178. **Sofja Tšepelevitš.** Experimental studies and modeling of solute-solvent interactions. Tartu, 2018, 109 p.
179. **Märt Lõkov.** Basicity of some nitrogen, phosphorus and carbon bases in acetonitrile. Tartu, 2018, 104 p.
180. **Anton Mastitski**. Preparation of α-aza-amino acid precursors and related compounds by novel methods of reductive one-pot alkylation and direct alkylation. Tartu, 2018, 155 p.
181. **Jürgen Vahter**. Development of bisubstrate inhibitors for protein kinase CK2. Tartu, 2019, 186 p.

182. **Piia Liigand.** Expanding and improving methodology and applications of ionization efficiency measurements. Tartu, 2019, 189 p.
183. **Sigrid Selberg.** Synthesis and properties of lipophilic phosphazene-based indicator molecules. Tartu, 2019, 74 p.
184. **Jaanus Liigand.** Standard substance free quantification for LC/ESI/MS analysis based on the predicted ionization efficiencies. Tartu, 2019, 254 p.
185. **Marek Mooste.** Surface and electrochemical characterisation of aryl film and nanocomposite material modified carbon and metal-based electrodes. Tartu, 2019, 304 p.
186. **Mare Oja.** Experimental investigation and modelling of pH profiles for effective membrane permeability of drug substances. Tartu, 2019, 306 p.
187. **Sajid Hussain.** Electrochemical reduction of oxygen on supported Pt catalysts. Tartu, 2019, 220 p.
188. **Ronald Väli.** Glucose-derived hard carbon electrode materials for sodium-ion batteries. Tartu, 2019, 180 p.
189. **Ester Tee.** Analysis and development of selective synthesis methods of hierarchical micro- and mesoporous carbons. Tartu, 2019, 210 p.
190. **Martin Maide.** Influence of the microstructure and chemical composition of the fuel electrode on the electrochemical performance of reversible solid oxide fuel cell. Tartu, 2020, 144 p.
191. **Edith Viirlaid.** Biosensing Pesticides in Water Samples. Tartu, 2020, 102 p.
192. **Maike Käärik.** Nanoporous carbon: the controlled nanostructure, and structure-property relationships. Tartu, 2020, 162 p.
193. **Artur Gornischeff.** Study of ionization efficiencies for derivatized compounds in LC/ESI/MS and their application for targeted analysis. Tartu, 2020, 124 p.
194. **Reet Link.** Ligand binding, allosteric modulation and constitutive activity of melanocortin-4 receptors. Tartu, 2020, 108 p.
195. **Pilleriin Peets.** Development of instrumental methods for the analysis of textile fibres and dyes. Tartu, 2020, 150 p.
196. **Larisa Ivanova.** Design of active compounds against neurodegenerative diseases. Tartu, 2020, 152 p.
197. **Meelis Härmas.** Impact of activated carbon microstructure and porosity on electrochemical performance of electrical double-layer capacitors. Tartu, 2020, 122 p.
198. **Ruta Hecht.** Novel Eluent Additives for LC-MS Based Bioanalytical Methods. Tartu, 2020, 202 p.
199. **Max Hecht.** Advances in the Development of a Point-of-Care Mass Spectrometer Test. Tartu, 2020, 168 p.
200. **Ida Rahu.** Bromine formation in inorganic bromide/nitrate mixtures and its application for oxidative aromatic bromination. Tartu, 2020, 116 p.
201. **Sander Ratso**. Electrocatalysis of oxygen reduction on non-precious metal catalysts. Tartu, 2020, 371 p.
202. **Astrid Darnell.** Computational design of anion receptors and evaluation of host-guest binding. Tartu, 2021, 150 p.

203. **Ove Korjus.** The development of ceramic fuel electrode for solid oxide cells. Tartu, 2021, 150 p.
204. **Merit Oss.** Ionization efficiency in electrospray ionization source and its relations to compounds' physico-chemical properties. Tartu, 2021, 124 p.
205. **Madis Lüsi**. Electroreduction of oxygen on nanostructured palladium catalysts. Tartu, 2021, 180 p.
206. **Eliise Tammekivi.** Derivatization and quantitative gas-chromatographic analysis of oils. Tartu, 2021, 122 p.
207. **Simona Selberg.** Development of Small-Molecule Regulators of Epi-transcriptomic Processes. Tartu, 2021, 122 p.
208. **Olivier Etebe Nonga.** Inhibitors and photoluminescent probes for in vitro studies on protein kinases PKA and PIM. Tartu, 2021, 189 p.
209. **Riinu Härmas.** The structure and H2 diffusion in porous carbide-derived carbon particles. Tartu, 2022, 123 p.
210. **Maarja Paalo.** Synthesis and characterization of novel carbon electrodes for high power density electrochemical capacitors. Tartu, 2022, 144 p.
211. **Jinfeng Zhao.** Electrochemical characteristics of Bi(hkl) and micro-meso-porous carbon electrodes in ionic liquid based electrolytes. Tartu, 2022, 134 p.
212. **Alar Heinsaar.** Investigation of oxygen electrode materials for high-temperature solid oxide cells in natural conditions. Tartu, 2022, 120 p.
213. **Jaana Lilloja.** Transition metal and nitrogen doped nanocarbon cathode catalysts for anion exchange membrane fuel cells. Tartu, 2022, 202 p.
214. **Maris-Johanna Tahk.** Novel fluorescence-based methods for illuminating transmembrane signal transduction by G-protein coupled receptors. Tartu, 2022, 200 p.
215. **Eerik Jõgi.** Development and Applications of E. coli Immunosensor. Tartu, 2022, 103 p.
216. **Alo Rüütel.** Design principles of synthetic molecular receptors for anion-selective electrodes. Tartu, 2022, 109 p.
217. **Tanel Sõrmus.** Development of stimuli-responsive and covalent bisubstrate inhibitors of protein kinases. Tartu, 2022, 148 p.
218. **Oleg Artemchuk.** Autotrophic nitrogen removal processes for nutrient removal from sidestream and mainstream wastewater. Tartu, 2022, 115 p.
219. **Andre Leesment.** Quantitative studies of Brønsted acidity in biphasic systems and gas-phase. Tartu, 2023, 83 p.
220. **Meeli Arujõe-Sado.** Structural effects in aza-peptide bond formation reaction. Tartu, 2023, 83 p.
221. **Jonas Mart Linge.** Electrochemical reduction of oxygen on silver-based catalysts. Tartu, 2023, 269 p.
222. **Tõnis Laasfeld.** Integrating Image Analysis and Quantitative Modeling for a Holistic View of GPCR Ligand Binding Dynamics. Tartu, 2023, 226 p.
223. **Ernesto de Jesus Zapata Flores.** Derivatization Reagents used in negative mode electrospray LC-MS. Tartu, 2023, 107 p.

224. **Patrick Teppor.** Obtaining platinum-free oxygen reduction catalysts through biomass valorization: a case study of peat. Tartu, 2023, 161 p.
225. **Peeter Valk.** Methanol Oxidation on Platinum-Rare-Earth Metal Oxide Activated Catalysts. Tartu, 2023, 162 p.
226. **Shidong Chen.** Unravelling prehistoric plant exploitation in eastern Baltic: organic residue analysis of plant-based materials by multi-method approach. Tartu, 2023, 245 p.
227. **Yogesh Kumar.** M-N_4 macrocycle-based catalysts for electrocatalysis of oxygen reduction and oxygen evolution. Tartu, 2023, 224 p.
228. **Kerli Martin.** Recognition of carboxylates by synthetic receptors – from structure-affinity studies to solid-contact anion-selective electrode prototyping. Tartu, 2024, 158 p.